THESIS

A NOVEL DYNAMIC ZERO-PLANE DISPLACEMENT HEIGHT APPROACH TO IMPROVE REMOTE SENSING-BASED ESTIMATION OF HEAT FLUXES OVER CORN FIELDS

Submitted by

Debashree Halder Tuli

Department of Civil and Environmental Engineering

In partial fulfillment of the requirements

For the Degree of Master of Science

Colorado State University

Fort Collins, Colorado

Fall 2025

Master's Committee:

Advisor: José L. Chávez

Frances Davenport

Russ Schumacher

ABSTRACT

A NOVEL DYNAMIC ZERO-PLANE DISPLACEMENT HEIGHT APPROACH TO IMPROVE REMOTE SENSING-BASED ESTIMATION OF HEAT FLUXES OVER CORN FIELDS

Accurate estimation of latent heat flux (LE) and sensible heat flux (H) is critical for determining actual crop evapotranspiration (ET_a) rates and optimizing irrigation. However, heat fluxes over cropped systems are sensitive to surface aerodynamic properties, including the zero-plane displacement height (d_o), which may introduce uncertainties in the ET_a characterization. This study presents a novel approach to better characterize d_o through a dynamic fractional vegetation cover (f_{veg}) and new canopy porosity (Φ_{dp}) term, derived from an unmanned aerial system (UAS) imagery. Field experiments were conducted in 2024 at the USDA-ARS Limited Irrigation Research Farm in Greeley, Colorado, across two corn fields, one fully irrigated (FI) and the other deficit irrigated (DI). Soil water content sensors, soil heat flux plates, soil temperature sensors, net radiometers, infra-red radiometers, and eddy covariance (EC) systems were deployed to measure all the components of the land surface energy balance. Weekly crop development was monitored using a multispectral radiometer (MSR5) to capture the surface reflectance and canopy temperature, and crop height (H_c) was measured manually using a measuring tape. Near-daily calibrated mini-satellite imagery (PlanetScope) was used to derive continuous estimates of spatially distributed net radiation (R_n) across both fields. The upwind fetch area sampled by the EC tower varies with H_c, weather conditions, wind speed (u_z), and wind direction (θ) were used to dynamically determine the heat flux footprint area and to align it with the contributing field zones. The newly developed and existing d_o models were applied to estimate H and LE; the results were

evaluated with EC-based corrected H and LE values. Both the Φ_{dp}-based and f_{veg}-based d_0 models demonstrated improved accuracy over existing models in estimating H, reducing NRMSE by up to 15.6% (DI) and 21.1% (FI), and 16.9% (DI) and 21.9% (FI), respectively. Similarly, both models achieved a higher agreement index, d_r (0.7 in DI, 0.74 in FI), reflecting a stronger model-observation correlation. These results underscore the potential of incorporating Φ_{dp} and f_{veg} in dynamically characterizing d_o to improve H and LE estimation, thereby enhancing energy balance modeling and advancing water management strategies in irrigated agricultural systems.

ACKNOWLEDGEMENTS

I am deeply grateful to God for providing strength and perseverance throughout this journey. I sincerely thank my family for their constant encouragement and emotional support, and my friends for their motivation during challenging times. I extend my appreciation to my advisor, Dr. José L. Chávez, for his structured guidance, insightful feedback, and steady mentorship. I am also thankful to my lab mate, Manish Giri, for his intellectual collaboration and valuable assistance in my research. I acknowledge the Fulbright Program for granting the scholarship that made it possible to pursue my studies in the United States. Finally, I express gratitude to everyone who contributed to the fieldwork and data collection for the year 2024; their help was essential to the success of this research project.

TABLE OF CONTENTS

LIST OF TABLES

LIST OF FIGURES

CHAPTER 1: INTRODUCTION

Agriculture is the largest consumer of freshwater globally and thus plays a critical role in ensuring water use efficiency and productivity for sustainable food production (Sharma et al., 2015). In the western U.S. Corn Belt, approximately 58% of total annual maize production depends on irrigation (Grassini et al., 2011). However, much of this region, including the Southwest, western Great Plains, and parts of the Northwest, faces substantial water stress due to increasing agricultural, municipal, and industrial demands on nearly fully utilized water resources (A. Irmak et al., 2011) (Dettinger et al., 2015; Engelbert & Scheuring, 2023).

Accurate estimation of actual evapotranspiration (ET_a) is essential for effective irrigation scheduling and water resource management. Among various approaches, multispectral remote-sensing data-based methods have shown strong reliability for instantaneous ET (ET_i) estimation (Chávez et al., 2008). The main component governing ET_a is latent heat flux (LE), and the sensible heat flux (H), both influenced by crop type, growth stage, irrigation practice, nutrient level, and soil properties. Remote sensing (RS)-based models are particularly advantageous for estimating H in semi-arid, water-stressed regions such as Greeley, Colorado (Mohan et al., 2020).

Nevertheless, achieving surface energy balance (EB) remains a persistent challenge, as H and LE are often approximately underestimated by 10-30%, leading to deviations from the principle of energy conservation (Twine et al., 2000; Xie et al., 2025). Enforcing energy balance closure (EBC) is therefore necessary, with the method depending on the spatial homogeneity or heterogeneity of the site (Lloyd et al., 1997). Reliable flux estimation further requires accurate computation of

surface aerodynamic parameters, which depend on the interaction between canopy structure, wind dynamics, and surface temperature within the measurement footprint.

Zero-plane displacement height (d_o, m) is a key aerodynamic variable that defines at which height, within the crop, the wind speed tends to zero due to surface roughness, directly affecting the land surface energy heat flux estimation. Its accurate determination is challenging because it varies with wind direction, wind speed, and canopy geometry. Wind interaction with crop rows and canopy gaps modifies the effective roughness length, influencing the partitioning between H and LE. High wind speeds promote evapotranspiration by enhancing turbulent mixing and lowering near-surface humidity (Ning et al., 2022), while weak or unstable winds reduce flux estimation accuracy (Goulden et al., 1997). Temperature gradients between the surface and air above the crop canopies further alter wind profiles and complicate the derivation of the so-called aerodynamic temperature, particularly in heterogeneous fields where RS-based estimation becomes less reliable (Boulet et al., 2012).

To address spatial variability, representing canopy and inter-row heterogeneity through a crop height model (CHM) and a binary classification of effective versus ineffective crop areas provides a more realistic depiction of the surface roughness (Meiyan et al., 2022). Similarly, incorporating a pseudo surface temperature model (PSTM) derived from multispectral data improves estimation of surface temperature and net radiation, enhancing the accuracy of surface energy balance analyses by capturing the spatial and temporal variability in canopy temperature and energy fluxes (Peters and Evett, 2007).

Existing d_o models primarily depend on H_c and assume homogeneous canopies. These models neglect the effects of canopy porosity, field heterogeneity, dynamics of the wind penetration in row crops, and the influence of the surface and air temperature difference on wind circulation. These structural and aerodynamic factors strongly influence momentum absorption and, consequently, the accuracy of H and LE estimations. Therefore, this study develops a novel d_o parameterization that explicitly incorporates canopy structure dynamics and wind-field interactions. By accounting the variations in canopy porosity and canopy organization, the proposed approach enhances the land surface EBC and the overall reliability of RS-based ET_a models. Such advancement supports more precise water management strategies and better adaptation of irrigation practices in water-limited agricultural regions.

CHAPTER 2: LITERATURE REVIEW

Irrigation water management is vital for mitigating the impacts of climate variability and improving the precision of agricultural practices such as drip irrigation to minimize water loss (Evans & Sadler, 2008). Achieving this requires an accurate assessment of micrometeorological variables. The estimation of H is particularly sensitive to aerodynamic resistance to heat transfer (r_{ah}) and friction velocity (u_*), from the surface to a height above the canopies, both of which depend on the accurate determination of the dynamic d_o.

Measuring d_o under real field conditions is challenging due to complex, dynamic interactions between vegetation and wind flow (Raupach, 1994; Dong et al., 2001). Jackson (1981) emphasized the importance of a detailed characterization of roughness elements for accurate d_o estimation. Although wind speed (u_z) plays a role in determining d_o, relying solely on it can lead to unrealistic results; Molion and Moore (1983) found that u_z alone exerts a limited influence. Incorporating in-canopy wind profiles into d_o parameterization improves model accuracy and captures canopy-atmosphere interactions more effectively. Vegetation indices such as the leaf area index (LAI, m^2/m^2) help track canopy development but are insufficient on their own to represent the dynamic conditions of agricultural systems (Schaudt, 2000). The empirical equation developed by Brutsaert (1982) is widely popular for estimating the d_o as a function of crop height (H_c, m) only, while this model is only suitable for tall height, and equally spaced crops. The model developed by Pereira et al. (1999) incorporates LAI along with H_c; however, it also misses the dynamic changes the d_o might have on heterogeneous surfaces due to crop structure and wind penetration differences within row crops/surfaces. A similar limitation is also applicable to the Shaw and Pereira (1982) d_o model, where the surface drag coefficient (C_d) is incorporated as a function of LAI only. Thus,

it is necessary to develop a dynamic d_o model that effectively captures the wind interaction with the crop.

Remote sensing techniques are increasingly used to optimize irrigation due to their efficiency and cost-effectiveness (Al-Majali & Chávez, 2024; Karthikeyan et al., 2020; Shanmugapriya et al., 2019). This technique uses multispectral data collection, offers a non-invasive means of observing large areas with reduced field effort (Kasampalis et al., 2018). High-resolution RS platforms have proven reliable for capturing spatial variability of land surface heat fluxes (Chávez et al., 2005). However, measuring aerodynamic parameters across large regions through direct field observation is impractical (Schaudt, 2000). Limited technical and financial resources further constrain surface flux measurement across heterogeneous landscapes, making full validation of RS-based heat flux algorithms difficult. While regional datasets can support calibration, accurate validation still requires simultaneous in situ heat flux measurements across dominant land-use types (Bastiaanssen et al., 1998). Consequently, models developed for large-scale areas often rely on satellite-derived or land-cover-based estimates, supported by ground data for calibration.

Estimating H from surface radiation temperature obtained via thermal infrared sensors can introduce large errors, particularly under stable atmospheric conditions, dense vegetation, or uneven terrain. Variations in wind speed, soil moisture, and canopy structure affect the difference between the aerodynamic temperature (which controls heat exchange) and the observed surface temperature, reducing accuracy (Mahrt & Vickers, 2004). Net radiation (R_n) also varies with reflected shortwave and emitted longwave components, which depend on surface type, emissivity, and reflectance properties (Jackson et al., 1985; Ferreira et al., 2011). Combining ground-based

cloud-free meteorological data with remote multispectral observations has been found effective for estimating R_n at the field scale (Jackson et al., 1985).

Soil heat flux (G) and surface temperature (T_s) are critical for achieving energy balance in RS models. Chávez (2005) demonstrated that G is closely linked to vegetation structure, as represented by LAI, and that surface temperature derived from thermal imagery, when properly corrected for emissivity, viewing geometry, and canopy heterogeneity, can accurately represent ground conditions for surface energy balance estimation.

Accurate H_c retrieval from RS or satellite data remains challenging under field conditions (Schaudt, 2000), but advances in digital elevation and terrain modeling from unmanned aerial systems (UAS) have improved accuracy. Meiyan et al. (2022) developed a 3D crop height model for estimating above-ground biomass using Red, Green, Blue, and near-infrared (NIR) spectral bands with LAI, while Maimaitijiang et al. (2019) introduced a canopy volume model that integrates vegetation indices, showing strong correlations with biomass. These approaches demonstrate the potential of RS data for reliable H_c estimation.

In summary, integrating accurate micrometeorological measurements with RS techniques enhances the reliability of energy balance modeling and irrigation management. Continued refinement of aerodynamic parameterization, surface flux estimation, and model evaluation metrics remains essential for improving predictive accuracy and supporting sustainable agricultural water use.

2.1 Hypothesis and Objectives

Achieving land surface EBC requires accurate estimation of R_n, G, H, and LE. Depending, in part, on the precise determination of surface aerodynamic variables. This study focuses on modeling the d_o by capturing the dynamic interactions between wind flow and crop structure to simulate field-scale water and energy exchanges in agricultural systems.

The central hypothesis of this research is that incorporating dynamic variables, such as wind speed, crop structure and row orientation, heat flux footprint area, soil surface heterogeneity, and canopy-air temperature gradients, will enhance the estimation of H and LE, thereby improving EBC.

The specific objectives of the research are:

1. To develop a distributed pseudo surface temperature model (PSTM) from PlanetScope imagery and point-based surface temperature (T_s) readings.

2. To evaluate the accuracy of remote sensing-based net radiation (R_n) estimates.

3. To generate UAS-based distributed canopy height (H_c) surfaces (CHM).

4. To derive dynamic zero-plane displacement height (d_o) from PSTM and CHM by integrating a new crop porosity (Φ_{dp}) concept, vegetation fraction (f_{veg}), temperature gradient (ΔT), wind speed (u_z), and crop row orientation and wind interactions (θ_{rel}).

5. To evaluate the performance of the derived dynamic d_o and compare results with the performance of the existing d_o models for estimating sensible (H) and latent (LE) heat fluxes.

CHAPTER 3: METHODOLOGY

3.1 Study Region

The study was conducted at the Limited Irrigation Research Farm (LIRF), operated by the United States Department of Agriculture (USDA) Agricultural Research Service (ARS), located in Greeley, Colorado, USA (40.4463° N, 104.637° W) as shown in Fig. 3.1. The experimental field covered an area of approximately 10 acres (184 m × 220 m), with an approximate elevation of 1425 m above mean sea level (msl). The field was divided into two equal sections based on irrigation strategy. The western half was managed under full irrigation (FI), while the eastern half operated under deficit irrigation (DI).

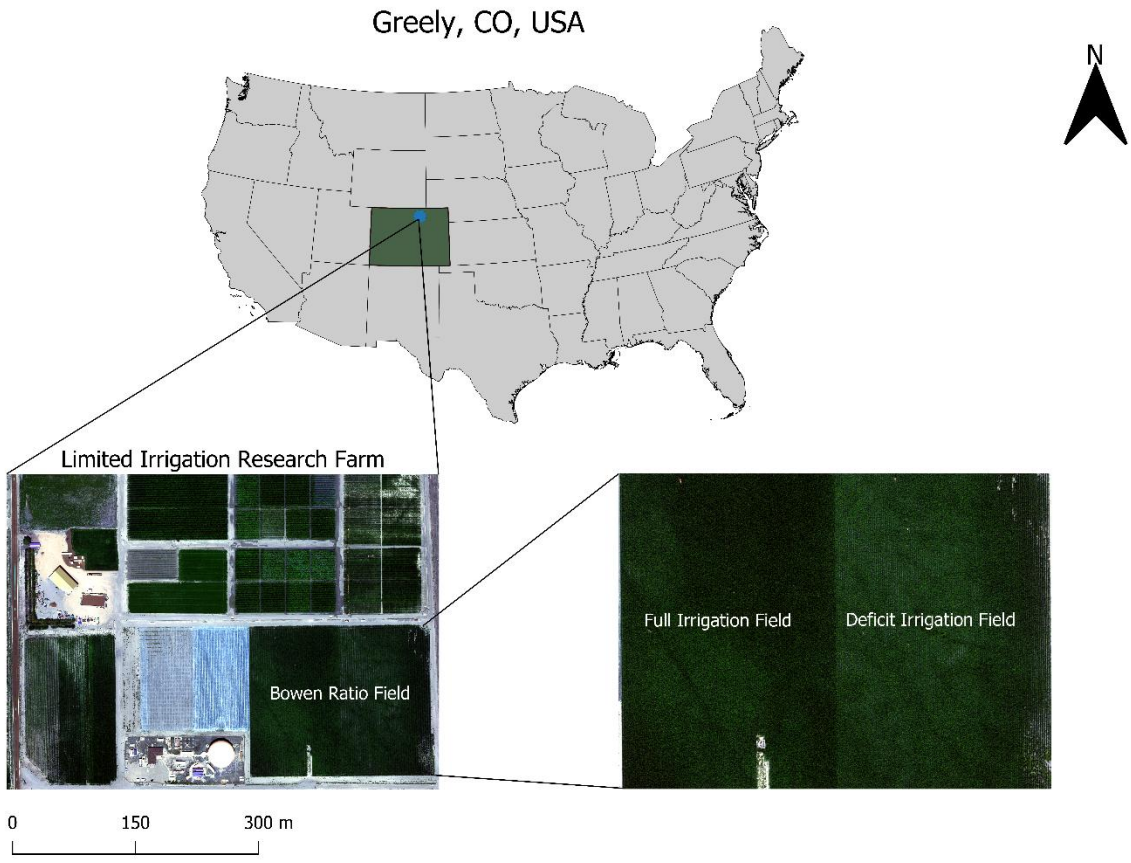

Fig. 3.1. Location of the study area in Greely, Colorado

A subsurface drip irrigation (SDI) system was employed for both treatments, with drip lines installed at a depth of 0.23 m below the soil surface and emitters spaced at 0.30 m intervals. The site was characterized by an arid to semi-arid climate. Soil across the DI and FI sections exhibited variability, with bulk density ranging from 0.95 to 1.60 g/cm³; according to the USDA soil texture-bulk density relationship, the bulk density range indicated textural variations from loamy sand to silty clay loam. The average bulk density between 15 cm and 200 cm depth was determined to be 1.16 g/cm³, classifying the soil as sandy clay loam.

Corn (Zea mays L.) was sown on May 3, 2024, with seedling emergence observed on May 16, 2024. Data collection started in June, following the completion of field instrumentation, and continued through October 2024.

3.2 Instrumentation and Data Collection

A spatially distributed network of sensors was deployed across the experimental field to support the d_o modeling, shown in Fig. 3.2. Two eddy covariance (EC) towers, EC1 in the DI zone and EC2 in the FI zone, were installed to measure H and LE fluxes at 30-minute intervals. Each EC system includes a Gill WindMaster PRO, a three-axis ultrasonic anemometer, which measures three-dimensional wind components at high frequency (10 Hz), enabling calculation of u_*. It was installed at a height of 3.5 m. An open-path LI-7500DS analyzer from LICOR captured rapid fluctuations (10 Hz) in atmospheric water vapor (and CO_2), critical for computing LE. An infrared thermometer (IRT) was available for recording T_s.

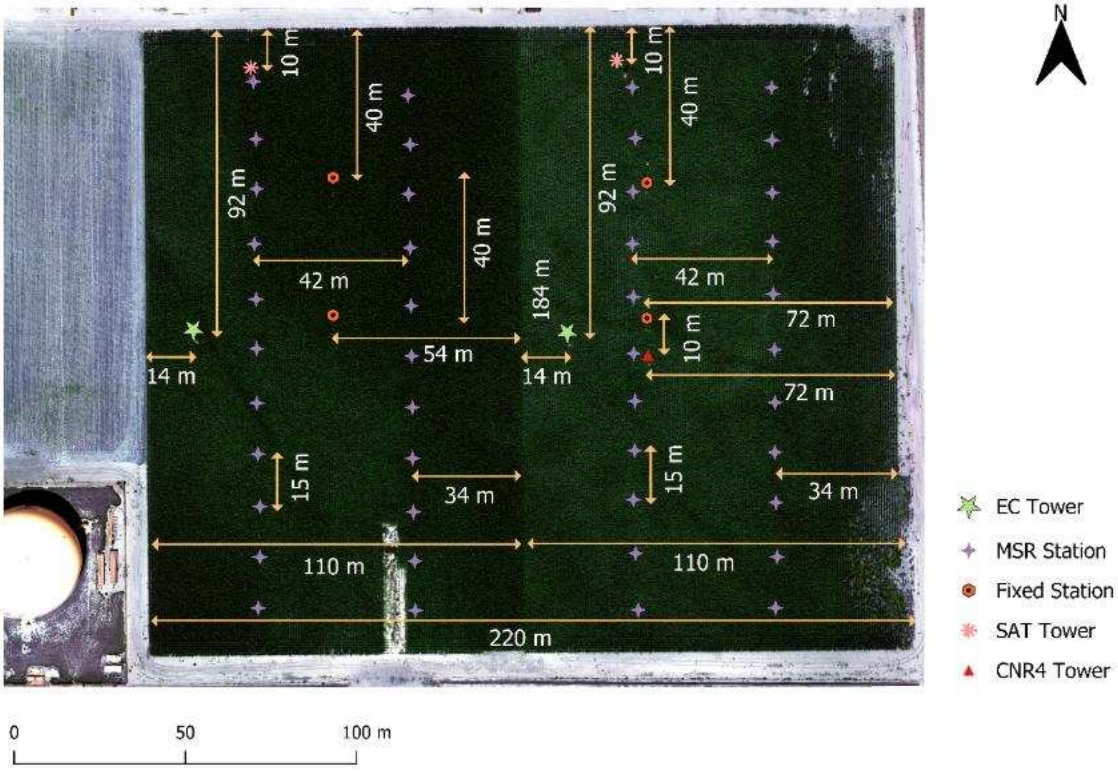

Fig. 3.2. Instrumentation setup at the USDA-ARS Limited Irrigation Research Farm (LIRF), Greeley, CO, in 2024. EC towers were installed in both full (FI) and deficit (DI) irrigation zones. MSR stations show locations where canopy reflectance was measured. Fixed stations (orange hexagons) provided radiation and soil data. The SAT towers and the CNR4 tower recorded additional atmospheric information.

The spatial variability in canopy structure and development was monitored using a handheld multispectral radiometer (MSR5, CropScan Inc., Rochester, MN) mounted on a telescopic pole for nadir-view measurements, yielding a ground footprint of approximately 1 m in diameter. The instrument captured reflectance in five spectral bands: red (660 nm), green (560 nm), blue (485 nm) (these three bands also denoted as RGB), near-infrared (830 nm), and mid-infrared (1650 nm), and canopy surface temperature with an added IRT sensor. Measurements were taken weekly at 22 designated station points in each irrigation zone, with stations spaced approximately

15 m apart. These stations were named as MSR stations in Fig. 3.2. The FI field was taken as the no. 1 field, and the DI field was taken as the no. 2 field, and each field was divided into east and west. Following that, the FI field's MSR points were named as 1 W1 to 1 W11, and 1 E1 to 1 E11. Similarly, the DI field's MSR points were named as 2 W1 to 2 W11 and 2 E1 to 2 E11. Data collection was conducted around local noon time under clear-sky conditions for eight consecutive weeks. At those MSR stations, the crop heights were collected on the same day, earlier in the morning.

Four fixed stations were installed across the field, also denoted as EB stations, to monitor radiation and soil conditions. ST 1.1 (40 m from North) and ST 1.2 (80 m from North) were positioned in the FI zone, while ST 2.1 (40 m from North) and ST 2.2 (80 m from North) were positioned in the DI zone. Each fixed station was equipped with one net radiometer (CNR-01, Kipp & Zonen, Delf, The Netherlands) to measure R_n, two IRTs (SI-111, Apogee Inc., Logan UT) to measure canopy temperature in the oblique and nadir positions.

Surface atmosphere temperature profile (SAT) towers were installed near the northern boundary of each field section. Each tower was equipped with three six-plate solar radiation shields for T_a and relative humidity (RH) sensors. Additionally, three 03101-L cup anemometers from Campbell Scientific, Inc. were installed to measure wind speed (u_z). Air temperature (T_a) and RH were recorded using HMP45C, Vaisala, at 15-minute intervals.

One CNR4 (4-way net radiometer, Kipp & Zonen, Delf, The Netherlands) tower was installed in the DI zone, 10 m distant from the ST 2.2. While not central to this study, this tower offered auxiliary radiation data for cross-checking atmospheric conditions.

Each station's position on the ground was recorded using a handheld GPS (Global Positioning System) device to know the latitude, longitude, and height of the towers and sensors.

To validate station measurements, data were sourced from the Colorado Agricultural Meteorological Network (CoAgMet) station Greeley04 (GLY04). The retrieved variables included shortwave solar radiation (R_s), clear-sky shortwave radiation (R_{so}), wind direction (θ_u) as azimuth angle, along with u_z, T_a, and RH.

Multispectral imagery from Planet's Dove satellite constellation (PlanetScope) was integrated for spatiotemporal assessment of canopy and surface conditions. These CubeSat-based satellites capture the land surface with near-daily coverage at a nominal 3 m spatial resolution and include multispectral bands covering RGB and NIR wavelengths. The surface reflectance products were calibrated with Landsat and Sentinel-2 satellite data after internal calibration. Additionally, the images were geometrically harmonized, utilizing sensor telemetry, ground control points, and digital elevation models to align with the Sentinel-2 data standards.

An unmanned aerial system (UAS) was deployed to obtain high-resolution imagery describing spatial and temporal variations in canopy and soil surface properties within the study area administered by the USDA-ARS Division. Flights were conducted at an altitude of roughly 120 m above ground level, with nine cloud-free missions completed during the growing season. The platform carried two sensors: a MicaSense RedEdge-MX multispectral camera (MicaSense Inc., Seattle, WA, USA) and a thermal infrared camera used to measure outgoing surface radiation. The multispectral unit recorded reflectance in four distinct wavebands: blue (475 nm), green (560 nm, 27 nm), red (668 nm, 14 nm), and near-infrared (842 nm, 57 nm). Data from the red and NIR regions were later applied to compute vegetation indices. Image capture followed overlap settings of about 80 % along-track and 70 % cross-track, producing a ground sampling distance near 5 cm per pixel for the reflectance layers. Surface reflectance outputs were then combined with simultaneous nadir temperature measurements from SI-111 radiometric sensors (Apogee Instruments Inc., Logan, UT, USA) to support analyses of surface energy-balance dynamics.

3.3 Calibration and Interpolation of Satellite Imagery Using Field Measurements

3.3.1 PlanetScope Imagery Processing

Raster images from PlanetScope were processed in QGIS 3.40 ‘Bratislava’ (QGIS Development Team, 2024). Each image was first clipped to the area of interest (AOI), and cloud masking was applied to remove affected pixels. The four spectral bands (red, green, blue, and NIR) were scaled by dividing pixel values by 10,000 to match standard reflectance units. GPS coordinates of the MSR and fixed stations were imported into the imagery, ensuring consistency in the coordinate system (EPSG:32613 – WGS 84 / UTM Zone 13N). Around each station, a 5 m buffer was created

using the buffer tool, and the mean reflectance of the enclosed pixels was extracted as the representative value for that location.

Mean band surface reflectance (SR) values were then plotted by day of year (DOY) for each station. The resulting time series showed some noise, which was reduced by fitting polynomial regression curves of degree 1 through 5. For each band and station, predicted SR values were generated from the fitted equations and were compared with the observed SR values to calculate R^2. The 5^{th}-degree polynomial consistently produced the best fit, with the general form:

$$y = ax^5 + bx^4 + cx^3 + dx^2 + ex + f$$

where y is the band SR value; x is DOY; a, b, c, d, e, and f are the coefficients.

Thus, 5^{th}-degree polynomial regression equations were derived for each SR band for MSR and fixed station points. The respective equations were used to determine the modified SR band values for each station's buffered zone, including the missing days when the PlanetScope images were unavailable.

3.3.2 Calibration of PlanetScope Imagery

The noise-reduced SR band values from PlanetScope imagery were compared with SR values measured by the MSR instruments at 44 station locations on corresponding dates. For each spectral band, linear regression equations were established to relate satellite-derived and ground-measured

reflectance. Across the 44 stations and four bands (red, green, blue, and NIR), a total of 352 paired observations (44 × 8) were obtained, providing a statistically robust dataset to represent the field-scale relationship. The resulting regressions are presented in the form of linear regression equations as: $y = mx + c$.

To calibrate the PlanetScope imagery, MSR reflectance values were taken as the ground truth. For each spectral band (RGB, and NIR), the derived regression equations were applied to adjust the corresponding band values. In these equations, y represents the MSR reflectance and x represents the PlanetScope reflectance. The calibration was performed on a pixel-by-pixel basis, ensuring that every pixel value in the raster images was multiplied by the respective regression coefficients and adding the constants. Using this approach, all raster images by DOY were calibrated, resulting in MSR-based PlanetScope raster datasets for the entire field.

3.3.3 Temporal Gap Filling of PlanetScope Imagery

The calibrated PlanetScope raster SR images were not available for every DOY, although a continuous daily record was required for subsequent analyses. To address this gap, raster images for missing DOYs were generated through linear interpolation between the nearest available dates, using the following equation (Eq. 1):

$$\text{Raster}_{\text{missing}}(x, y) = \text{Raster}_{t_1}(x, y) + \frac{\text{Raster}_{t_2}(x, y) - \text{Raster}_{t_1}}{t_2 - t_1} \times (t - t_1) \quad \text{.....(1)}$$

where x and y axis represents the longitude and latitude, respectively; $Raster_{missing}$ (x, y) is the interpolated pixel value at missing day t; $Raster_{t_1}$ (x, y) is the pixel value from the earlier available raster (before the missing day); $Raster_{t_2}$ (x, y) is the pixel value from the later available raster (after the missing day); t_1 is the date of the earliest available raster image; t_2 is the date of the latest available raster image; t is the date of the missing raster (to be interpolated).

To ensure realistic results, interpolated band values were constrained to a minimum of zero, thereby avoiding negative pixel values. This procedure provided a complete set of multispectral raster images for the entire growing season, along with missing days filled by interpolation for further analyses. Next, the normalized difference vegetation index (NDVI) and the optimized soil adjusted vegetation index (OSAVI) were calculated from the band values for the PlanetScope imagery for every DOY.

3.4 Pseudo Surface Temperature Estimation and Validation

3.4.1 MSR-based IRT Data Collection and Correction

The IRT mounted on MSR5 recorded both emitted canopy radiation and reflected background radiation. Because the reflected component can bias the readings, the raw measurements were corrected for surface thermal emissivity (ε_s) and background radiation.

At each MSR point station, five subsamples were collected using the MSR5. Any subsample deviating by more than two standard deviations from the mean was removed, and the remaining values were averaged to obtain one IRT measurement per station.

To exclude measurements affected by cloud cover, solar radiation data from the CoAgMet "Greeley 04" station were used. For each date and time of MSR measurement, the observed incoming shortwave radiation (R_s, W/m^2) and the theoretical clear-sky shortwave radiation (R_{so}, W/m^2) were extracted, and the ratio R_s/R_{so} was calculated. Only values with ratios greater than 0.8, representing clear-sky conditions, were retained.

The filtered IRT data were then corrected for background radiation (Eq. 2) following Brunsell & Gillies' (2002) procedure, as:

$$IRT_{corrected} = \sqrt[4]{\frac{[IRT_{measured} + 273.15]^4 - [(1 - \varepsilon_s) \times (-15 + 273.15)]}{\varepsilon_s}} - 273.15 \quad \text{.....(2)}$$

where $IRT_{measured}$ is the MSR-derived canopy temperature in °C; the background temperature was assumed -15 °C, and the $IRT_{corrected}$ was denoted as IRT for later calculations. The surface emissivity (ε_s) was calculated by following equation A4 (Appendix A), which required the calculation of the NDVI (Eq. A1, Appendix A). Mean NDVI values were extracted for MSR5 SR reading locations, fixed stations, EC towers, and CNR4 tower points for a 5 m radius buffer area from the raster images.

3.4.2 Normalization of MSR-based IRT Observations to Satellite Overpass Time

PlanetScope scenes were acquired near local noon, so MSR5 IRT measurements collected at other times of the day, depending on cloud cover, required normalization to ensure comparability.

Without this adjustment, diurnal temperature fluctuations would bias the integration of ground-based and satellite data.

The procedure applied here followed Peters & Evett (2007), who developed a scaling method for irrigation scheduling using canopy temperature. Their approach rescales field measurements relative to reference station data so that all values represent noon conditions when temperature readings were taken at different times and places. The normalization was performed as:

$$T_{rmt,12} = T_e + \frac{(T_{rmt,t} - T_e) \times (T_{ref,12} - T_e)}{(T_{ref,t} - T_e)} \quad \text{.....(3)}$$

where $T_{rmt,12}$ (°C) is the noon-normalized MSR5-based T_s to be computed; $T_{rmt,t}$ (°C) is the MSR5 T_s at the measurement time t; T_e (°C) is the early-morning temperature, assumed spatially uniform and taken from the fixed station; $T_{ref,t}$ (°C) and $T_{ref,12}$ (°C) are the reference-station temperatures at time t and at noon, respectively.

Reference IRT data were collected from ST 1.1 for the corn growing season. Next, the clear-sky conditions were met ($R_s/R_{so} > 0.8$) for all MSR5 observations for that day. This procedure yielded non-equivalent MSR5 T_s consistent with PlanetScope overpass conditions.

3.4.3 Estimation of Surface Temperature from MSR5 IRTs

To evaluate the relationship between T_s and SR, the corrected IRT data from the MSR stations were analyzed using the OSAVI, a dimensionless vegetation index (Eq. 4) derived from PlanetScope SR imagery, which minimizes soil background effects in vegetation monitoring. Due

to limited MSR observations after September 6, early and mid-growing phases, T_s were analyzed using MSR-based IRT data. The relationship between OSAVI and corrected IRT was modeled using an exponential decay function, representing the physical expectation that canopy temperature decreases as healthy vegetation density increases. The form of the model was:

$$IRT = a \times OSAVI^{b} \quad \text{……..……(4)}$$

where IRT (°C) is the corrected IRT-based T_s, OSAVI is dimensionless, and a and b are empirical coefficients determined for each phase. The model performance was evaluated to assess the explanatory strength of OSAVI for spatial and temporal T_s variation.

3.4.4 Estimation of Nadir Surface Temperature from Fixed-Station IRTs

ST 1.1 and ST 2.2 were equipped with both nadir- and oblique-view IRT sensors, and ST 1.2 was equipped with a nadir-view IRT sensor, while ST 2.1 recorded only oblique IRTs. To estimate nadir-view canopy temperature at the latter sites, a calibration equation was developed using the measurements from ST 1.1, ST 1.2, and ST 2.2 and then applied to ST 2.1 and EC1 station points.

The calibration incorporated vegetation status through the OSAVI, calculated from PlanetScope reflectance as:

$$OSAVI = \frac{NIR - Red}{NIR + Red - 0.16} \quad \text{…….(5)}$$

where the constant 0.16 is a soil adjustment factor to reduce background soil influence in areas of partial vegetation cover.

Relationships between nadir and oblique IRT-based were modeled as in Equation 6:

$$IRT_n = a + (b \times OSAVI) + (c \times IRT_0) \quad \text{.....(6)}$$

where IRT_n (°C) is the nadir T_s, IRT_0 (°C) is the oblique T_s, and OSAVI is dimensionless. Only the regressions with $b < 0$ were retained. The raster imagery for IRT-based T_s, developed using this equation, is denoted as a three-point-based IRT raster, as this equation was derived from three station points.

Finally, all nadir T_s values derived through calibration were corrected for emissivity and background radiation following Brunsell & Gillies (2002), using the same procedure as for MSR-based T_s data, the raster imagery for T_s.

3.4.5 OSAVI – Surface Temperature Relationships by Crop Growth Phase

OSAVI values were first calculated using PlanetScope SR imagery for a 5 m radius buffer around EC, fixed, and MSR station points. These values were then plotted against the DOYs, and based on the resulting line graph, the crop growing season was divided into three phases: Phase 1 (June 11 - July 11, initial phase), Phase 2 (July 12 - September 6, mid-phase), and Phase 3 (September 7 - October 20, end phase).

3.4.6 Generation of Pseudo-Surface Temperature Model

Regression equations from the OSAVI - T_s relationships were applied to the OSAVI raster images from PlanetScope imagery. The equations were developed based on MSR station IRT data were used only for the image dates that fell within Phase 1 (June 11 - July 11) and Phase 2 (July 12 - September 6), crop growth phases, and for Phase 3 (September 7 - October 20), fixed station-based equations were used, because those were derived from only 5 points data (ST 1.1, ST 1.2, ST, 2.1, ST 2.2 and EC1) based in the field.

For each raster within these date ranges, the corresponding phase equation was applied to convert pixel-level OSAVI values into T_s values through multiplication with the coefficients, denoted as pseudo-surface temperature.

Thus, pseudo-surface temperature raster imagery for PlanetScope was produced for Phases 1, 2, and 3. These outputs provided spatially continuous maps of surface temperature for the early, middle, and late stages of crop growth, directly linked to vegetation status through OSAVI.

3.4.7 Temporal Extension of Pseudo-Temperature Model from the PlanetScope Imagery

After generating the pseudo T_s raster for every DOY for the local noon time (12:00 pm), the equation from Peters & Evett (2007) (Eq. 11) was again used to extend T_s estimates for other times of day. The goal was to calculate pseudo-IRT-based surface temperature ($T_{rmt,t}$) raster images for 30-minute intervals between 11:00 am and 01:00 pm. This was possible because reference station temperatures were available for each of these times.

$$T_{rmt,t} = T_e + \frac{(T_{rmt,12} - T_e) \times (T_{ref,t} - T_e)}{(T_{ref,12} - T_e)} \quad \text{.....(7)}$$

For each day, early morning and noon reference values (T_e and $T_{ref,12}$) and half-hourly reference temperatures ($T_{ref,t}$) between 11:00 am and 3:00 pm were compiled from the fixed IRT stations. The $T_{rmt,12}$ was extracted for every DOY from the noon pseudo-surface temperature raster. By combining all the variables for temperature (°C), T_s were generated for 11:00, 11:30, 12:30, and 1:00, timesteps. This approach preserved the spatial distribution of T_s provided by the noon raster while capturing diurnal variation through the temporal pattern observed at the reference station.

3.4.8 Net Radiation Estimation from PlanetScope and SAT Data

To estimate distributed R_n values at local noon for each DOY during the growing season, raster SR imagery from PlanetScope, and the pseudo T_s raster were used, within the surface radiation budget equation (Eq. 8):

$$R_n = (1 - \alpha)\, R_s + \varepsilon_a \sigma T_a^4 - \varepsilon_s \sigma T_s^4 \quad \text{.....(8)}$$

where R_n (W/m^2) is the net radiation, R_s (W/m^2) is the incoming shortwave radiation, extracted from the CoAgMet "Greeley 04" station; α (dimensionless) refers to surface albedo (Eq. A5, Appendix B); ε_a (dimensionless) is the thermal air emissivity (Eq. A8, Appendix B); ε_s (dimensionless) is the thermal surface emissivity (Eq. A4, Appendix A); T_a (K) and T_s (K) are, air and surface temperatures from EC and pseudo-surface temperature raster images, respectively, and

σ ($W/m^2/K^4$) is the Stefan-Boltzmann constant ($5.67\times10^8 W/m^2/K^4$). Surface properties varied spatially across the field, and thus, R_n was calculated for each image pixel.

Finally, combining these raster-based inputs (σ, ε_s, T_s) station-based variables (T_a, RH, e_a, ε_a) along with the R_s from CoAgMet in the radiation budget equation, half-hourly raster images of R_n for the field were generated for the local noon time span and were evaluated with field net radiometers' Rn readings from the fixed stations.

3.5 Soil Heat Flux Estimation

Soil heat flux (G) represents the amount of energy transferred to the ground at the surface. G (W/m^2) was calculated using the PlanetScope SR imagery and three RS-based empirical models.

Model developed by Singh et al. (2008), which is a function of NDVI, and as equation (9):

$$G = [0.3811 \times \exp^{(-2.3187 \times NDVI)}] \times R_n \quad \text{.....(9)}$$

where NDVI, and R_n (W/m^2) were extracted from the PlanetScope SR imagery.

The model developed by Singh et al. (2008) was applied in this study to estimate G across the entire study area. The equation was originally derived from data collected in a maize field under a subsurface drip irrigation system (Irmak et al., 2008), similar to the irrigation system used in the

present study. The model's performance for estimating G was further assessed by A. Irmak et al. (2011), who reported satisfactory accuracy.

3.6 Crop Height Estimation from UAS-Derived Digital Elevation Models (DEMs)

3.6.1 Generation of DEMs from Multispectral UAS Imagery

Digital surface model (DSM) imagery and multispectral imagery captured by the UAS drone were jointly utilized to construct a reference bare-soil elevation surface. UAS flights were conducted on DOY 155, 190, 200, 209, 229, 232, 250, and 271 of the corn growing season. Each flight produced a DSM raster image representing surface height along with four-band multispectral imagery (Blue, Green, Red, and Near-Infrared). The multispectral imagery was combined into a multiband raster for each flight date, and an additional band was derived for the NDVI. All raster images were clipped to the AOI and resampled to a uniform spatial resolution to ensure consistency across the dataset.

To generate a digital elevation model (DEM) for the study area, the DSM raster from DOY 155 was selected as the reference elevation surface. This was done since this date corresponded to the early growing season, the vegetation cover was minimal, and most pixels represented bare soil.

Bare soil pixels were identified from DOY 155 multispectral imagery using an NDVI threshold value. A fixed NDVI threshold of 0.25 was applied, where all pixels with NDVI < 0.25 were classified as non-vegetation pixels and were labeled bare soil, while pixels with NDVI ≥ 0.25 were labeled as vegetation. The selected bare soil pixels were then converted into point datasets using

the raster-to-point tool, with each point preserving its geographic location and linked to the corresponding elevation value from the DSM. The large set of georeferenced elevation points was subsequently interpolated across the field using the inverse distance weighting (IDW) method, implemented in QGIS using a Python script. This interpolation process generated a continuous elevation raster, referred to as the pseudo-DEM, which represented the bare-soil surface elevation for the study field.

3.6.2 Crop Height Calculation and Calibration

Crop canopy height (H_c, m) was derived, for each UAS flight date, by subtracting the pseudo-DEM from the corresponding DSM (Meiyan et al., 2022) according to the following equation (10):

$$H_c = DSM_{DOY} - DEM_{bare\ soil} \quad \text{.....(10)}$$

where DSM_{DOY} comes with the canopy heights for a specific day and $DEM_{bare\ soil}$ comes with only the bare soil heights at different parts of the study field.

This operation was applied to all raster datasets from DOY 155 through DOY 271, producing crop height models (CHM) for the entire field for the available DOYs. Negative and undefined values were replaced with zero to eliminate spurious outputs.

To improve the agreement between UAS-derived H_c, a calibration procedure was applied. First, from the CHM, H_c values were extracted at the 44 MSR reading station locations. Then, the extracted UAS-based H_c values and the corresponding field-measured H_c values, at MSR stations,

were merged into a single dataset. Because the field and UAS-based H_c observations were not always available on the same DOYs; linear interpolation was performed on both UAS and field datasets to harmonize the datasets. For any missing DOY, the interpolation was carried out using the following equation:

$$H_{c_{interpolated}} = H_{c_{prev}} + \frac{(H_{c_{next}} - H_{c_{prev}})}{(DOY_{next} - DOY_{prev})} \times (DOY_{interpolated} - DOY_{prev}) \quad (11)$$

where $H_{c_{interpolated}}$ (m) is the interpolated crop height ; $H_{c_{prev}}$ (m) is the crop height on the closest previous DOY; $H_{c_{next}}$ (m) is the crop height on the closest subsequent DOY; $DOY_{interpolated}$ is the day of the year for which interpolation was performed; DOY_{prev} is the closest previous day; DOY_{next} is the closest subsequent day.

As this interpolation procedure was applied consistently to both UAS and field datasets, paired values existed for all DOYs.

After interpolation, a combined dataset was constructed with paired UAS- and field-based H_c values across all MSR stations and DOYs. Outliers and negative interpolated values were removed before analysis. A form of power regression model was then fitted to establish the correction relationship between UAS- and field-measured crop heights as:

$$H_{c_{field}} = a \times H_{c_{UAS}}^{b} \quad (12)$$

where $H_{c_{field}}$ (m) is the field-measured crop height; $H_{c_{UAS}}$ (m) is the crop height (m) extracted from CHM, developed from the UAS DSM imagery; a is the coefficient; b is the power value.

Validation of the corrected H_c raster values extracted at the MSR reading stations demonstrated a good relationship with the corresponding field-measured data. However, H_c raster imagery before DOY 200 presented data gaps where portions of the imagery were missing due to some cloud cover. Several MSR reading stations were located within these missing-data areas, preventing the reliable extraction of UAS-based H_c for validation. For this reason, calibration could only be conducted for the period DOY 200 to DOY 271. Accordingly, subsequent analyses of UAS-derived H_c were based on the corrected CHM raster imagery within this range.

3.6.3 Vegetation Masking of CHM

To ensure that crop height estimates represented only effective vegetation, a vegetation mask was applied to each corrected CHM raster image. The mask was generated in binary form, assigning a value of 1 to effective crop pixels and 0 to non-crop pixels. The classification was based on NDVI values derived from multispectral SR imagery, with thresholds determined separately for each DOY to account for seasonal variation in crop development. The DOY-specific NDVI thresholds ranged between 0.45 and 0.60.

Before applying the masks, both the corrected CHM raster imagery and the NDVI-based vegetation masks were resampled to a uniform spatial resolution to maintain consistency across the dataset. The binary masks were then applied to the corrected CHMs using raster calculations,

such that only crop pixels classified as effective vegetation were retained. At the same time, all non-vegetated or ineffective crop pixels were assigned as zero.

This masking procedure reduced noise in the canopy height maps by removing the influence of weeds, crop residues, and bare soil, thereby improving the reliability of crop height estimates derived from the UAS-based CHMs.

3.6.4 Missing Data Estimation of CHM

During processing of the corrected CHM, continuous null values were observed for DOY 190 and DOY 200, primarily over the deficit irrigation field, due to the shadow from clouds and other image interferences. Several MSR stations were located within these missing-data zones, which prevented the reliable extraction of H_c values. To address this issue, a gap-filling procedure was implemented to reconstruct H_c values in the affected areas while preserving spatial variability.

Crop height values were first extracted from MSR reading stations located within the missing-data zones for later DOYs (209 to 271), where complete images were available. These values were then used to model H_c dynamics over time. To capture the growth trajectory more realistically, a logistic growth model was fitted using data from DOY 209 to DOY 250, as logistic regression is widely applied to describe biological growth processes such as canopy height growth. The logistic growth function used, mentioned in equation 13:

$$H_c = \frac{K}{1 + \exp[-r\,(DOY - t_o)]} \quad \text{.....(13)}$$

where K is the maximum canopy height; r is the growth rate; t_o is the inflection point corresponding to the DOY of rapid growth.

To integrate these estimates spatially, shapefiles were created to delineate the missing-data zones for DOY 190 and separately for DOY 200. A scaling approach was then applied, using DOY 229 as the reference raster because it was the nearest complete and high-quality CHM. The scaling procedure was defined as:

$$Scale_{190} = \frac{\overline{H}_{c_{190}}}{\overline{H}_{c_{229}}}, \quad Hc_{190}(x, y) = H_{c_{229}}(x,y) \times Scale_{190} \text{……..(14)}$$

$$Scale_{200} = \frac{\overline{H}_{c_{200}}}{\overline{H}_{c_{229}}}, \quad Hc_{200}(x, y) = H_{c_{229}}(x,y) \times Scale_{200} \text{ ……...….....(15)}$$

where $\overline{H}_{c_{190}}$ and $\overline{H}_{c_{200}}$ are the mean canopy heights estimated from the logistic model for DOY 190 and DOY 200, respectively; $\overline{H}_{c_{229}}$ is the mean canopy height from the reference CHM at DOY 229, and H_c (x, y) represents pixel-wise crop height values.

This method allowed the missing areas to be reconstructed while maintaining the spatial variability of $H_c$across the field. Finally, the reconstructed raster images for DOY 190 and DOY 200 were multiplied by their corresponding NDVI-based vegetation masks to ensure that only effective crop pixels were retained, with non-vegetated areas assigned a value of zero. The gap-filled raster images were then resampled to match the target resolution of the corrected CHM dataset, ensuring consistency across all flight dates.

Validation of the reconstructed CHMs demonstrated that the gap-filled H_c values were in good agreement with the field-measured H_c data, confirming the robustness of the applied method and the reliability of the corrected raster imagery for subsequent analyses.

Finally, missing days between DOY 190 to DOY 271 were generated by adopting pixelwise linear interpolation using the following formula:

$$H_c^{(i,j)}(t) = H_c^{(i,j)}(DOY_p) + \frac{t - DOY_p}{DOY_n - DOY_p} * [H_c^{(i,j)}(DOY_n) - H_c^{(i,j)}(DOY_p)] \quad \text{.....(16)}$$

where $H_c^{(i,j)}(t)$ is the interpolated crop height at pixel (i, j) on DOY t, (DOY_p) and (DOY_n) is the nearest known DOYs before and after t, and $H_c^{(i,j)}(DOY_n)$ and $H_c^{(i,j)}(DOY_p)$ are the known crop heights at pixel (i, j) on DOY_p and DOY_n.

Thus, a continuous set of raster imagery for H_c became available for further analyses.

3.6.5 Evaluation of Crop Height and Zero-Plane Displacement Height Models

To assess the accuracy of canopy structural and aerodynamic parameterization, the H_c raster images generated from the UAS-derived CHM were compared to the performance of existing empirical H_c models [18, 19, 20]. Similarly, zero-plane displacement height layers, estimated from UAS data, were compared to the performance of existing [21, 22, 23] formulations.

Leaf area index (LAI, m^2/m^2) was calculated using UAS multispectral SR imagery and the empirical relationship proposed by Chávez et al. (2009):

$$LAI = 0.263 \times \exp^{3.813 \cdot OSAVI} \quad \text{..(17)}$$

where the OSAVI, with a soil adjustment factor L_2=0.16, was calculated for the entire study area, based on which raster imagery with LAI was generated. The resulting LAI raster was subsequently used as an input for the existing H_c and d_o models.

3.6.5.1 Comparison of UAS-Derived and Existing Crop Height Models

Three published models were used to simulate H_c as a function of vegetation indices (Al-Majali & Chávez, 2024), and their results were compared with the field-calibrated CHM:

i. LAI-based H_c model, developed by (Al-Majali & Chávez, 2024; Costa-Filho et al., 2021) as:

$$H_c = \left[0.697 \times \exp^{(0.236 \cdot LAI)}\right] - [3.42 \times \exp^{(-3.177 \cdot LAI)}] \quad \text{...(18)}$$

ii. OSAVI-based H_c model, developed by (Anderson et al., 2004) as:

$$H_c = [(1.86 \times OSAVI) - 0.8] \times [1 + \{0.000000482 \times \exp^{(17.69 \cdot OSAVI)}\}] \quad \text{...(19)}$$

iii. LAI-based H_c model, developed by Arslan et al. (2022) as:

$$H_c = \frac{LAI + 0.3919}{1.44} \quad \text{.....(20)}$$

Therefore, each H_c model used a vegetation index (NDVI, OSAVI, or LAI) derived from the UAS imagery, and a raster dataset for each model was generated for H_c. To ensure consistency in canopy representation, only pixels with NDVI > 0.25 were considered, and both effective and non-effective vegetation height pixels were counted in this comparison.

The corresponding H_c values were extracted from the raster images and averaged for each DOY. Finally, the mean modeled (existing) H_c values were then compared with the UAS-derived H_c (mean of each DOY), and statistical performance evaluation was conducted.

3.6.5.2 Evaluation of Existing Zero-Plane Displacement Height Models

The d_o was computed using the mean H_c and the mean LAI derived from the CHM, described in 3.6.5.1. Three existing d_o models were evaluated:

i. The widely d_o used formula, based on H_c, developed by Brutsaert (1982) as:

$$d_o = \frac{2}{3} \cdot H_c \ldots\ldots(21)$$

ii. The H_c , and the LAI-based model, developed by Pereira et al. (1999) as:

$$d_o = H_c \times \left(1 - \frac{1 - \exp^{-0.5 \cdot LAI}}{LAI}\right) \ldots\ldots(22)$$

iii. The H_c, LAI, and the drag coefficient (C_d)-based d_o model, developed by Shaw & Pereira (1982) as:

$$d_o = 1.1 \times H_c \times \ln\left(1 + X^{1/4}\right) \ldots\ldots(23)$$

where $X = C_d \times LAI$, and C_d was taken as 0.2 for the corn plants.

Thus, the DOY-wise mean values of H_c and LAI were used as d_o model inputs to ensure temporal consistency, and the comparison was conducted statistically, with field-measured d_o values established for these three models.

3.7 Sensible Heat Flux Estimation

3.7.1 Air Temperature, Humidity, and Wind Data Inputs

The reliable estimation of H requires accurate inputs of T_a, RH, u_z, and θ. To ensure consistency, measurements from the EC systems and CoAgMet stations were compared for the near-noon period (11:00 am to 01:00 pm).

The T_a and RH were extracted from EC1 and EC2 at 30-minute intervals and compared with CoAgMet values (5-minute data averaging 30 minutes). The two sources showed strong agreement, confirming the reliability of EC-derived T_a and RH.

In contrast, u_z and θ from EC1 and EC2 showed weak agreement with CoAgMet and, when used in the heat flux calculations, produced unrealistically low H compared to the corrected fluxes calculated from the EBC. For this reason, u_z and θ were instead taken from CoAgMet and adjusted to the same 30-minute resolution as the EC data, which improved the estimates of H.

The variables R_s and R_{so} from CoAgMet were also used to ensure data quality. A cloudiness filter was applied by calculating the ratio R_s/R_{so}; time steps with values above 0.8 were retained with their corresponding wind directions, while all others were excluded.

3.7.2 Footprint Modeling and Weighting

The purpose of footprint modeling was to accurately associate remotely sensed parameters with the upwind surface heat flux source areas contributing to heat flux measurements recorded by the EC towers. Footprint parameters, including the offset distance (x_{offset}), and footprint length ($x_{70\%}$), were computed by EddyPro software (LICOR, Inc., Lincoln, NE). The footprint length ($x_{70\%}$) represented 70% of the total fetch distance, as the distal portion of the footprint contributes minimally to the measured fluxes. For simplification, a constant footprint width of 30 m was applied for all time steps. The EC tower location was defined as the coordinate origin (0,0) and

served as the reference point for orienting and rotating each modeled footprint area relative to the wind direction.

For each time step, a rectangular footprint area was generated in a local coordinate system using the extracted parameters. The box was positioned such that its upwind edge began at the offset distance from the EC tower. To align the footprint with the θ, the rectangle was rotated by an angle θ_{fp} defined as:

$$\theta_{fp} = (90 - \theta)\ \%\ 360 \quad \text{.....(24)}$$

where θ is the azimuth wind direction angle (degrees clockwise from north); θ_{fp} is the rotation angle corresponding to θ. The angle θ_{fp} was normalized within the range $0^{\circ} \leq \theta < 360^{\circ}$, in equation 32. This ensured that the footprint polygon was oriented correctly relative to wind direction flow, so that it spatially overlapped the raster imagery from UAS for H_c, and PlanetScope for pseudo T_s, R_n, G, and VI.

After rotation, the footprint polygons were checked against the boundary of the AOI.
The outside area percentage was calculated as:

$$\text{Percent outside} = \left(1 - \frac{\text{Total footprint area}}{\text{Area inside AOI}}\right) \times 100 \quad \text{.....(25)}$$

If more than 25% of the footprint extended beyond the field boundary, it was discarded. If 0 – 25% fell outside, the footprint was clipped to the AOI, and its effective length was adjusted accordingly. Footprints fully contained within the field were retained without modification.

To represent the spatial variability in heat flux contribution within each footprint, which describes how different upwind surface areas act as sources or sinks contributing to the measured flux (Heidbach et al., 2017), the effective footprint length was divided into five equal segments along the predominant wind direction. Each segment was assigned a weighting factor reflecting its relative contribution to the total flux: 0.15, 0.35, 0.30, 0.15, and 0.05 from the nearest to the farthest downwind segment, resulting in a total weight of 1.0. When extracting target parameter values from the raster images, pixel values within each segment were averaged separately to represent the mean condition for that segment. The general form of this weighted averaging can be expressed as:

$$P_{fp} = \sum_{i=1}^{5} [\bar{P}_i \times w_i] \quad \text{.....(26)}$$

where P_{fp} is the footprint-averaged value of the parameter; $\bar{P}_i$ is the mean pixel value within the i^{th} segment; w_i is the corresponding segment weight.

This modeling and weighting approach provided a spatially representative link between the EC tower heat flux source area and remote sensing-based surface variables, ensuring that extracted parameters accurately reflected the variable influence of upwind source areas. The schematic

diagram (Fig. 3.3) illustrates the geometric configuration, showing the offset distance from the EC tower, the fixed footprint width, and the five weighted segments aligned with the wind direction.

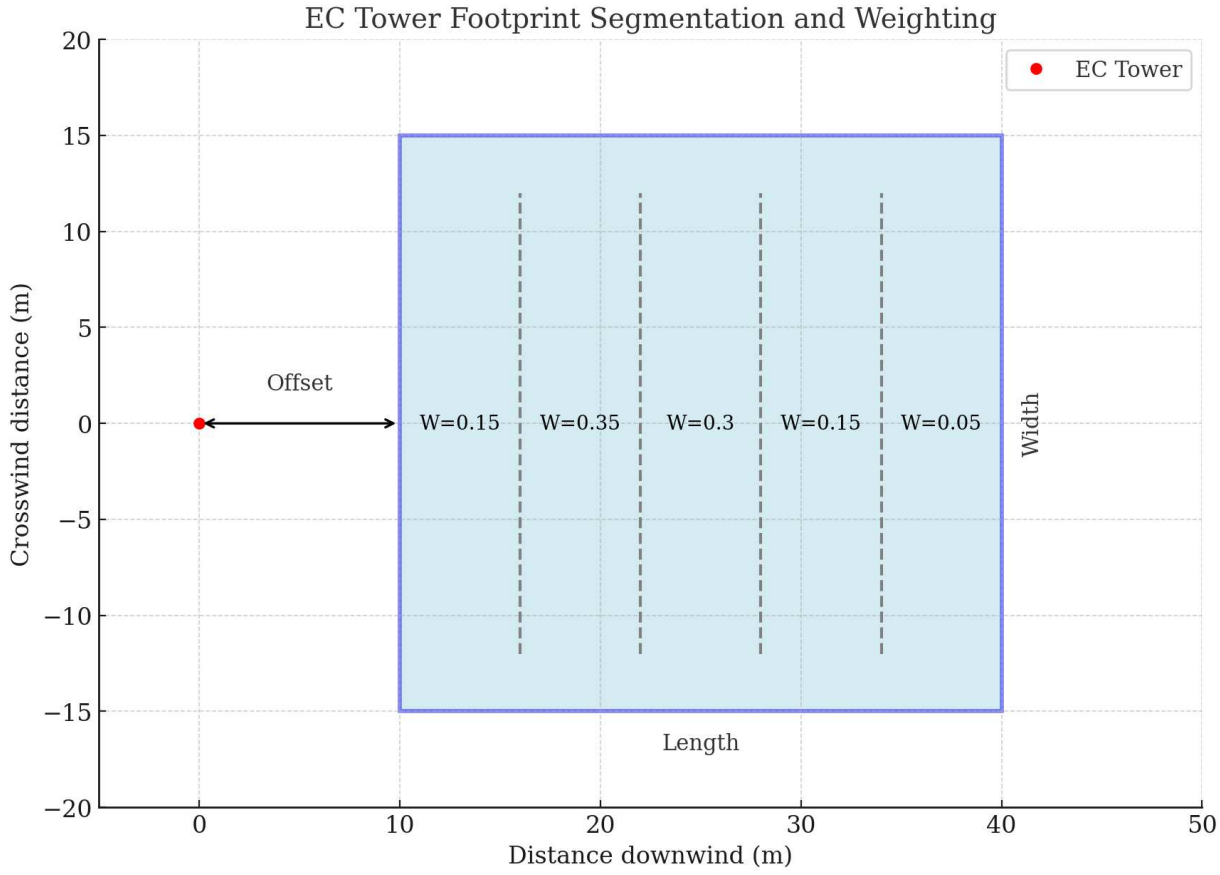

Fig. 3.3. Illustration of the EC tower footprint geometry showing the offset distance, fixed 30 m width, and five downwind segments, weighing 0.15, 0.35, 0.30, 0.15, and 0.05, respectively, representing their relative flux contributions.

3.7.3 Vegetation and Surface Variables from Remote Sensing

Vegetation and surface variables were obtained from PlanetScope and UAS-derived datasets to represent the canopy biophysical and temperature conditions corresponding to the EC tower heat flux source area footprints. The primary parameters included the leaf area index (LAI), R_n, T_s,

and H_c. The LAI was calculated from PlanetScope multispectral imagery using the empirical relationship mentioned in equation 17.

The footprint-weighted LAI values were extracted from the raster imagery for each time step following the segmentation and weighting procedure for each footprint at half-hourly intervals. Following the same procedure, the weighed T_s was obtained from the pseudo-surface temperature raster dataset, and R_n was obtained from the pseudo-surface temperature-based R_n raster dataset.

Continuous UAS-based H_c raster images were available for the period DOY 190 - 271. However, to maintain temporal consistency with the PlanetScope imagery and station-based datasets, H_c values for the missing dates during the early and late growing season (DOY 180 - 189 and DOY 271 - 291) were estimated through pixel-wise linear temporal extrapolation. Thus, raster images for H_c from DOY 180 to DOY 291 were available. The interpolated H_c raster images were subsequently processed to extract footprint-weighted H_c values, ensuring temporal and spatial consistency among all RS-derived parameters.

3.7.4 Aerodynamic Temperature Modeling

Radiometric T_s is often used as a proxy for aerodynamic temperature (T_o) when estimating H in land surface EB models (Colaizzi et al., 2004). However, T_s and T_o are not equivalent, as radiometric temperature represents the composite emission from canopy and soil surfaces, whereas T_o corresponds to the effective temperature at the level where turbulent heat exchange occurs between the surface and the atmosphere. To reduce this discrepancy and improve the accuracy of

H estimation, T_o was computed using the empirical model developed by Costa-Filho et al. (2021), which relates T_o to biophysical, surface, and aerodynamic variables derived from remote sensing.

The model expresses T_o as a function of T_s , T_a, f_c, and the turbulence-mixing row resistance (r_p). The general form of the model can be represented as:

$$T_o = f(T_s, T_a, f_c, r_p)$$

where T_s (°C) is the weighted pseudo-IRT-derived surface temperature, and T_a (°C) is the EC-measured air temperature for a 30-minute timestep, f_c is the weighted fractional canopy cover derived from NDVI, and r_{ah} (s/m) was calculated corresponding to the timesteps for neutral, stable, and unstable conditions by using LAI, H_c, d_o, and u_z derived parameters.

To account for seasonal variation in canopy density, the model was applied in a piecewise form based on four LAI intervals:

i. For LAI ≤ 1.5:

$$T_o = -8.742 \cdot f_c + 0.571 \cdot T_a + 0.529 \cdot T_s + 0.806 \cdot r_p + 3.295 \quad \text{.....(27)}$$

ii. For 1.5 < LAI ≤ 2.5:

$$T_o = -9.168 \cdot f_c + 0.485 \cdot T_a + 0.575 \cdot T_s + 0.160 \cdot r_p + 6.491 \quad \text{.....(28)}$$

iii. For 2.5 < LAI ≤ 3.5:

$$T_o = 4.708 \cdot f_c + 0.350 \cdot T_a + 0.580 \cdot T_s + 0.086 \cdot r_p \text{……..……..(29)}$$

iv. For LAI > 3.5:

$$T_o = -1.912 \cdot f_c + 0.443 \cdot T_a + 0.509 \cdot T_s + 0.115 \cdot r_p + 5.014 \text{……(30)}$$

The resulting T_o values were computed individually for each LAI class and aggregated temporally to produce a continuous record of aerodynamic temperature across the growing season.

This modeling approach ensured that the derived T_o dynamically responded to variations in canopy structure, vegetation cover, and meteorological conditions, providing a more physically realistic representation of surface-atmosphere interactions for use in subsequent H flux calculations.

3.7.5 Psychrometric and Surface Aerodynamic Variables Estimation

Psychrometric and air properties were determined to support the estimation of the EB components. The saturation vapor pressure (e_s) and actual vapor pressure (e_a) were obtained by adopting equations A6 and A7 (Appendix B), respectively.

The air pressure (P) was calculated as a function of elevation (Z_m) followed the procedures outlined in the (ASCE-EWRI, 2005) standardized equation:

$$P = 101.3 \times \left[\frac{293 - (0.0065 \times Z_m)}{293}\right]^{5.26} \text{……..(31)}$$

where P is the local mean atmospheric pressure in kPa at elevation Z_m, and Z_m = 1425 (avg. mean sea level elevation for Greely04)

The air density (ρ_a) was calculated using the CIPM-2007 (Picard et al., 2008) formulation for moist air density, which accounts for the contribution of water vapor to the total air mass:

$$\rho_a = \left(\frac{P}{R_d \times T_a}\right) \times \left(1 - \frac{0.378 \times e_a}{P}\right) \quad \text{.....(32)}$$

where P is in Pa; e_a is in Pa; R_d = the constant for dry air ≈ 287.04 J/kg/K; T_a is in K; ρ_a is in kg/m^3.

This formulation accounts for the contribution of water vapor to total air density and provides a more physically realistic representation of atmospheric conditions than the ideal gas approximation.

The specific heat of air at constant pressure was taken as, C_{p_a} = 1004 J/kg K, and the roughness length for momentum transfer (z_{om}) as a function of H_c, valid for crops with total LAI > 0.5 m^2/m^2 by (Colaizzi et al., 2004), was calculated as:

$$z_{om} = H_c \cdot e^{-0.5LAI} \cdot \left(1 - e^{-0.5LAI}\right) \quad \text{.....(33)}$$

where z_{om} and H_c are in m.

The roughness length for heat transfer (z_{oh}), where the proportionality constant (α) depends on canopy density and stability conditions. For a well-developed canopy, α was assumed to be 0.1 such that:

$$z_{oh} = \alpha \times z_{om} = 0.1 \times z_{om} \quad \text{(34)}$$

where z_{oh} and z_{om} are in m.

The d_o was estimated from PlanetScope-derived LAI raster images, and UAS-derived H_c for each EC half-hourly time step. The same empirical models previously described in Section 3.6.5.2: (Brutsaert, 1982), (Pereira et al., 1999), and (Shaw & Pereira, 1982) were used separately every time to calculate the aerodynamic parameters and ultimately to calculate H.

3.7.6 Estimation of Friction Velocity and Aerodynamic Resistance under Neutral Conditions

In the first iteration, neutral atmospheric stability was assumed. The u_* was computed as:

$$u_* = \frac{k \times u_z}{\ln\left(\frac{z_m - d_o}{z_{om}}\right)} \quad \text{(35)}$$

where u_* is in m/s, $k = 0.41$ is the von Kármán constant, u_z is the mean wind speed in m/s at measurement height (z_m), $z_m = 3.5$ m, d_0, and z_{om} are in m.

The aerodynamic resistance to heat transfer (r_{ah}) under neutral conditions was calculated as:

$$r_{ah} = \frac{\ln\left(\frac{z_m - d_o}{z_{om}}\right) \times \ln\left(\frac{z_m - d_o}{z_{oh}}\right)}{k^2 \times u_z} \quad \text{.....(36)}$$

where r_{ah} is in s/m, z_{om} and z_{oh} is in m; u_z is in m/s, z_m is in m and d_o is in m.

The first calculation of H for neutral atmospheric conditions was performed as:

$$H = \rho_a \times C_{pa} \times \frac{T_o - T_a}{r_{ah}} \quad \text{.....(37)}$$

where H is in W/m^2, ρ_a is in kg/m^3, C_{pa} is in J/kg K, T_o, and T_a are in K, and r_{ah} is in s/m.

For accurate H calculation, it is required to find the Monin-Obukhov length (L_{MO}, m), to characterize the atmospheric stability condition (Costa-Filho et al., 2021), computed as:

$$L_{MO} = - \frac{u_*^3 \times T_a \times \rho_a \times C_{pa}}{g \times k \times H} \quad \text{.....(38)}$$

where L_{MO} is in m, g ≈ 9.81 m/s, T_a is in K, ρ_a is in kg/m^3, C_{pa} is in J/kg K, and H is in W/m^2.

The magnitude of L_{MO} defines the atmospheric stability conditions as follows:

i. $L_{MO} = 0$, Neutral condition

ii. $L_{MO} < 0$, the atmospheric boundary layer is considered unstable (the H and LE fluxes are from the surface to the atmosphere)

iii. $L_{MO} > 0$, the atmospheric boundary layer is considered stable (the H and LE fluxes are from the atmosphere (air above) to the surface)

Once the L_{MO}, was calculated, the atmospheric stability correction process was initiated to adjust the equations for u_*, and r_{ah}.

3.7.7 Estimation of Friction Velocity and Aerodynamic Resistance after Stability-Correction

Atmospheric stability corrections terms: Ψ_m (atmospheric correction function for momentum transfer) and Ψ_h (atmospheric stability correction function for heat transfer) were applied in the second iteration, following the formulation used in (Chávez et al., 2005), as:

i. For unstable conditions ($L_{MO} < 0$):

- $\Psi_m = 2 \ln\left(\frac{1+x_1}{2}\right) + \ln\left(\frac{1+x_1^2}{2}\right) - 2\arctan(x_1) + \frac{\pi}{2}$……..(39)

- $\Psi_h = 2 \ln\left(\frac{1+x_1}{2}\right)$…….(40)

where $x_1 = \left[1 - 16\left(\frac{z_m - d_o}{L_{MO}}\right)\right]^{0.25}$ ……..(41)

ii. For stable conditions ($L_{MO} > 0$):

$$\Psi_m = \Psi_h = -5 \times \left(\frac{z_m - d_o}{L_{MO}}\right) \quad \text{(42)}$$

The stability-corrected friction velocity and aerodynamic resistance were then recalculated as:

$$u_* = \frac{k \times u_z}{\ln\left(\frac{z_m - d_o}{z_{om}}\right) - \Psi_m} \quad \text{(43)}$$

$$r_{ah} = \frac{\ln\left(\frac{z_m - d_o}{z_{oh}}\right) - \Psi_h}{0.41 \times u_*} \quad \text{(44)}$$

The H estimation was updated iteratively until convergence was achieved (difference between iterations < 5%).

Finally, the H was filtered by irrigation treatment based on EC tower location and wind direction, θ. For EC1, θ between 30°-160° corresponded to the DI field, and 210°-340° corresponded to the FI field. For EC2, θ between 30°-160° was assigned to the FI field. Data outside the selected ranges were removed to avoid using heat fluxes from other areas than the corn surface. This classification ensured that H values reflected heat fluxes originating from the upwind contributing area associated with the appropriate irrigation management zone within the corn fields.

Thus, using each selected d_o model (Eq.21, Eq. 22, and Eq. 23), u_* and r_{ah} was calculated to estimate H for the DI and FI field.

3.8 Evaluation of Sensible Heat Flux Estimates

3.8.1 Correction of Eddy Covariance Fluxes Using Energy Balance Closure

According to the principle of energy conservation, the surface EB equation states that the net available energy at the surface, represented by R_n after accounting for reflection and emission, is equal to the sum of the H, LE, and as shown in equation 45:

$$R_n = H + LE + G \quad \text{.....(45)}$$

The degree of agreement between the available energy and the measured turbulent fluxes can be quantified using the energy balance closure coefficient (k), defined as the ratio of the sum of H and LE to the available energy:

$$k = \frac{LE + H}{R_n - G} \quad \text{.....(46)}$$

A value of k = 1 indicates perfect EBC, meaning that the measured turbulent fluxes account for all available energy. In practice, however, the EB rarely closes completely, resulting in the k value less than 1.

Values of k lower than unity indicate an apparent energy deficit, commonly attributed to measurement uncertainties, neglected storage terms, or other unaccounted flux components. To address this imbalance, the turbulent fluxes obtained from the EC system were corrected for EBC (Eq. A9, Appendix C) by adopting the Bowen ratio (β) method (Eq. A10, Appendix C) at each 30-

minute interval by using weighted R_n values, and weighted G values for the same timestamps. Thus, the corrected H and LE become:

- $H_{corrected} = H_{measured} + \Delta H$……..….(47)

- $LE_{corrected} = LE_{measured} + \Delta LE$…….(48)

where $H_{measured}$ and $LE_{measured}$ are the measured H and LE from the EC; $H_{corrected}$ and $LE_{corrected}$ are the corrected ones by adding ΔH (Eq. A12, Appendix C) and ΔLE (Eq. A14, Appendix C) respectively, and all the fluxes were in W/m^2.

Then, using corrected H and LE, the adjusted closure coefficient (k_{adj}) was calculated and found to be equal to one:

$$k_{adj} = \frac{LE_{corrected} + H_{corrected}}{R_n - G} = 1 \text{……..……..….(49)}$$

3.8.2 Statistical Evaluation of Zero-Plane Displacement Height and Sensible Heat Flux

For every 30-minute time step, each d_o model and corresponding corrected H results were compared by plotting values in a scatter plot, which included a 1:1 line, and by observing the resulting coefficients of determination.

Model evaluation is essential for assessing accuracy and comparing performance across modeling approaches. Metrics based on absolute differences, such as mean absolute error (MAE) and mean absolute deviation (MAD), provide a more reliable measure of performance than squared-difference statistics like root mean squared error (RMSE) (Willmott & Matsuura, 2005, 2006; Willmott et al., 2009). Furthermore, Willmott et al. (2012) proposed a refined index of agreement (d_r) that effectively measures how closely model predictions match observations. This index offers a robust and adaptable framework for evaluating model performance, especially under variable and data-limited field conditions.

Before evaluation, negative H values and extreme outliers were excluded from both datasets. Outliers were identified using an absolute error threshold of 110 W/m^2 between the estimated sensible heat flux (H_{est}) and corrected sensible heat flux ($H_{corrected}$). This threshold was selected following standard EC quality control principles that combine physical plausibility limits and statistical filtering. Physically unrealistic fluxes were first removed through range checks, while statistically improbable values were screened by eliminating the data with the three standard deviation criterion (mean ± 3σ) (Foken et al.; Vickers & Mahrt, 1997); ensuring the retention of realistic turbulence while minimizing measurement artifacts.

Next, the d_o model performance in terms of accurately estimating H was quantified using a set of error and efficiency statistics commonly applied in surface energy balance validation. Each metric was calculated for H and for both DI and FI fields as follows:

i. Mean Absolute Error (MAE):

$$MAE = \frac{\sum_{i=1}^{n} |E_i - O_i|}{n} \text{……..….(50)}$$

It is the average magnitude of the deviation between modeled or estimated (E_i) and observed (O_i) fluxes. Smaller MAE values signify higher overall accuracy.

ii. Mean Absolute Deviation (MAD):

$$MAD = \frac{\sum_{i=1}^{n} |O_i - \bar{O}|}{n} \text{…….……..(51)}$$

It measures the variability or consistency of the O_i values around their mean ($\bar{O}$). Lower MAD values indicate stable and less scattered model outputs.

iii. Root Mean Square Error (RMSE):

$$RMSE = \sqrt{\frac{\sum_{i=1}^{n} (E_i - O_i)^2}{n}} \text{…….…….(52)}$$

It reflects the overall error magnitude, giving greater weight to large discrepancies. It highlights the presence of major deviations between E_i and O_i fluxes.

iv. Nash-Sutcliffe Efficiency (NSE):

$$NSE = 1 - \frac{\sum_{i=1}^{n} (E_i - O_i)^2}{\sum_{i=1}^{n} (O_i - \bar{O})^2} \text{……..(53)}$$

NSE evaluates the predictive performance and goodness of fit between estimated and observed fluxes. It compares the residual variance of the model with the variance of the observed data.

- NSE = 1 indicates a perfect match between modeled and measured values.
- NSE = 0 means the model predicts no better than the mean of observations.
- NSE < 0 shows that the model performs worse than using the mean as a predictor.

Because NSE is sensitive to large errors due to the squared residual term, it is effective in identifying models that deviate strongly from observations, but may produce extreme negative values under poor performance

v. Normalized Mean Absolute Error (NMAE) and Normalized Root Mean Square Error (NRMSE):

- $NMAE = \frac{MAE}{\bar{O}} \times 100\%$.....(54)

- $RMSE = \frac{RMSE}{\bar{O}} \times 100\%$.....(55)

Both metrics express the relative magnitude of model error as a percentage of the mean observed flux ($\bar{O}$).

NRMSE is analogous to RMSE but normalized to the $\overline{O}$, remains more sensitive to large errors because of the squared residual term. This sensitivity makes NRMSE more effective in detecting models that occasionally produce extreme deviations, while NMAE provides a more balanced measure of overall accuracy.

Lower values of NMAE and NRMSE indicate smaller relative errors and stronger model performance, allowing comparison among datasets with different flux magnitudes or measurement conditions.

vi. Normalized Nash-Sutcliffe Efficiency (NNSE):

$$NNSE = \frac{1}{2 - NSE} \quad \text{.....(56)}$$

NNSE converts the NSE into a bounded 0 – 1 range, improving interpretability and comparability among models. This normalization mitigates the issue of extreme negative NSE values, which can distort the assessment when model errors are large. By compressing the efficiency scale, NNSE reduces sensitivity to outliers and provides a more stable measure of predictive performance across different datasets and conditions. $NNSE = 1$ indicates perfect agreement, while values approaching 0 represent weak predictive skill.

vii. Refined index for model prediction (d_r):

$$d_r = \begin{cases} 1 - \dfrac{\sum_{i=1}^{n} |E_i - O_i|}{c \sum_{i=1}^{n} |O_i - \bar{O}|}, \text{ when } \sum_{i=1}^{n} |E_i - O_i| \le c \sum_{i=1}^{n} |O_i - \bar{O}| \\ \dfrac{c \sum_{i=1}^{n} |O_i - \bar{O}|}{\sum_{i=1}^{n} |E_i - O_i|}, \text{ when } \sum_{i=1}^{n} |E_i - O_i| > c \sum_{i=1}^{n} |O_i - \bar{O}| \end{cases}, \text{ with } c = 2 \ldots\ldots\ldots\ldots\ldots (57)$$

It was proposed by (Willmott et al., 2012) as an improved version of the original index of agreement introduced by (Willmott, 1981) It quantifies the degree of model-observation agreement by measuring how closely the estimated values E_i approach the corresponding O_i relative to the variability in the observed dataset.

Unlike correlation-based metrics such as R^2, which only assesses the strength of linear association, d_r evaluates both accuracy and precision, making it a more comprehensive performance indicator. The value of d_r ranges between -1 and 1, where:

- $d_r = 1$ represents perfect agreement between modeled and observed values,
- $d_r = 0$ represents model is as good as using the average observations,
- $d_r = -1$ represents a very poor performance of the model.

The exponent, c (commonly set to 2), increases the penalty for larger errors, emphasizing deviations that are substantial relative to the data spread. Compared to error-based indices such as RMSE, d_r is less sensitive to extreme outliers because it uses absolute rather than squared differences. This property makes it particularly suitable for flux-based comparisons, where occasional large deviations may result from measurement or footprint inconsistencies rather than model deficiency.

In this study, d_r was used to evaluate the overall model agreement and reliability of the three d_o-based sensible heat flux models across deficit and full irrigation conditions. Values of $d_r > 0.6$ are interpreted as indicating good model performance.

Finally, the H values estimated using the three d_o models were statistically evaluated and compared to assess their internal consistency and relative performance. For each model-based estimated H, the corresponding statistical parameters were computed. The comparison among these parameters provided a quantitative basis for identifying which d_o model produced the most stable and coherent H estimates. The same procedure was applied for LE estimation.

3.9 Determination of "Measured" Zero-Plane Displacement Height from EC-Derived Friction Velocity

The d_o was derived using "measured" u_* and horizontal u_z from the EC system under neutral atmospheric conditions. The neutral equation (Eq. 44) was used to derive d_o values, because the EC-derived u_* included the actual atmospheric conditions. The equation for d_o was derived by substituting equation 44 for u_*:

$$d_o = z_m - [z_{om} \times e^{\frac{k \times u_z}{u_*}}] \quad \text{.....(58)}$$

where d_o is the measured zero-plane displacement height in m, $z_m = 3.5$ m is the wind measurement height; z_{om} (m) was calculated from H_c (m); LAI was calculated following equation 25; $k = 0.41$

is the von Kármán constant; u_z (m/s) is the mean wind speed at z_m; u_* (m/s) was collected from EC every 30-minute timestep.

The u_* data from the EC towers was filtered for the time between 11:00 am to 01:00 pm. The EC1 (installed in the middle of the field) collected data from both of the fields (DI and FI), as wind came from the east and west parts of the field to the tower, and the EC2 only collected the data from the FI field. Thus, for the FI field, more data was available for d_o compared to the DI field.

Next, wind rose analyses were performed for the DI and FI fields and indicated that d_o variability was governed primarily by canopy structure, u_z, and θ, contributing to the dynamic behavior of d_o.

3.10 Development of Two New Empirical 'd_o' Models

3.10.1 Input Data and Preprocessing

To develop new dynamic d_o models, UAS-derived CHM data representing effective H_c, were used as the primary input. From the CHM raster images, the weighted dynamic porosity (Φ_{dp}) and weighted fractional vegetation cover (f_{veg}) were calculated as described in 3.7.2 for each EC footprint corresponding to the 30-minute time intervals. Similarly, weighted T_s were extracted from the PlanetScope-based pseudo-surface temperature raster images, while T_a for the same time steps were obtained from the EC system to determine the canopy-air temperature difference (ΔT).

The relative wind direction (θ_{rel}) was computed from the 15-minute wind azimuth angle data provided by CoAgMET and averaged to match the 30-minute EC interval. Concurrent u_z values

were extracted from the EC data. All datasets were restricted to local noon hours (11:00 am – 01:00 pm) to minimize diurnal variability.

3.10.2 Derivation of Surface Aerodynamic Terms

The concept of Φ_{dp} is analogous to crop porosity, representing the relative proportion of open space within the canopy volume under a given footprint area, and was computed as:

$$\Phi_{dp} = 1 - \frac{V_c}{V_f} \quad \text{.....(59)}$$

where V_c (m^3) is the crop volume within the EC heat flux footprint areas, V_f (m^3) is the total volume calculated by multiplying a given footprint area by the mean H_c included in that footprint area.

To produce these volumes at the raster level, V_c and V_f were determined as the sum of pixel-wise canopy height contributions within the corn vegetated areas:

- $V_c = \sum_{i-1}^{n} h_i \times A_{pix}$ .....(60)

- $V_f = A_{fp} \times \bar{h} = (N_{pix} \times A_{pix}) \times \bar{h}$ .....(61)

where h_i (m) is the corn canopy height of pixel i, A_{pix} (m^2) is the pixel area (same for every pixel), n is the total number of canopy pixels in the footprint area, N_{pix} is the total number of pixels under the footprint area, $\bar{h}$ is the mean height of vegetated pixels (N_{veg}) by only considering the pixels with corn H_c under the footprint.

The sum of crop heights was calculated as:

$$S_{h_{sum}} = \sum_{veg} h_i = N_{veg} \times \bar{h} \quad \text{.....(62)}$$

The f_c quantifies the fraction of crop canopy area within the footprint as:

$$f_{veg} = \frac{N_{veg}}{N_{pix}} \quad \text{.....(63)}$$

The temperature gradient between the canopy surface and air was expressed as:

$$\Delta T = T_s - T_a \quad \text{.....(64)}$$

where T_s and T_a are in K. ΔT was incorporated into the d_o model development to address how this temperature difference explains wind penetration within the canopy structure.

The θ_{rel} was calculated as the angular deviation between the azimuth angle and the crop row orientation as:

$$\theta_{rel} = \theta - \theta_{row} \text{……..……..(65)}$$

where θ_{row} (°) is 0°, because our corn is oriented North-South facing (0° and 180° axis), and θ (°) is the azimuth angle.

Then, the cosine and sine of the θ_{rel} were calculated to quantify the wind alignment with the crop rows. Specifically, $\cos(\theta_{rel})$ represents the degree of along-row flow, while $\sin(\theta_{rel})$ indicates the cross-row flow component. The azimuth angles were first converted from degrees to radians in Excel before computation.

3.10.3 Model Formulation, Training, Testing, and Validation

The empirical new dynamic models for d_o were formulated by relating the measured values from EC-derived datasets to selected surface aerodynamic/thermal predictors described earlier. Two formulations were tested: one using the weighted Φ_{dp} and another using the weighted f_{veg} as the primary canopy descriptor. Additional predictors, including ΔT, u_z, u_*, and $\sin(\theta_{rel})$, were incorporated to represent thermal and directional effects in d_o model formulations.

Multiple linear regression analysis was performed to establish the relationships between d_o and the selected predictors using the following general form:

$$d_o = \beta_1 X_1 + \beta_2 X_2 + \text{…….} + \beta_n X_n + C$$

where β_0 is the intercept, β_i are regression coefficients, X_i are the predictor variables, and C is the constant term.

The dataset combining both irrigation treatments, covering all crop growth stages throughout the growing season (a total of 530 data points), was randomly divided into two subsets: 80% for model calibration (training) and 20% for validation (testing). Random selection ensured that data from every phenological phase and both irrigation regimes were proportionally represented in each subset, minimizing sampling bias and enhancing model generalization. Model performance was assessed by using MAE, MAD, RMSE, NMAE, NRMSE, NSE, NNSE, R^2, and d_r, as described in section 3.8.1, to evaluate accuracy, precision, and overall agreement with observed values. The calibrated models were then tested independently for the DI and FI fields to verify their robustness across varying canopy, surface, and aerodynamic conditions.

The validated d_o models were applied in the estimation r_{ah} and u_*, which were then used to compute the H and LE, and were evaluated with EC-based $H_{corrected}$, and $LE_{corrected}$ heat fluxes as described in section 3.7.

Before the heat flux-based evaluation for the d_o models, unrealistic data for H and LE were removed based on physical and statistical criteria as described in 3.8.2. The same statistical evaluation procedure was followed for both flux components to maintain consistency across energy balance terms.

Thus, the developed empirical d_o models linked the canopy structural and aerodynamic predictors, enabling a dynamic representation of displacement height across different irrigation and canopy conditions.

CHAPTER 4: RESULTS and ANALYSIS

4.1 Irrigation Scheduling, Precipitation Patterns During Growing Season

The irrigation schedule for the study area was the same for both irrigation treatments/fields until DOY 160. After this DOY, the DI and FI fields followed distinct irrigation regimes. Therefore, the corn canopy structures in both fields were similar during the early growth stage. However, as the crop entered the peak of the growth phase, canopy development differences became prominent, reflecting the cumulative effect of the different irrigation schedules.

The DI received less frequent irrigations, whereas the FI field received irrigation more frequently and consistently throughout the season, as shown in Fig. 4.1. During the crop growing period, the cumulative irrigation depth was 306.80 mm for the DI field and 502.73 mm for the FI field. Irrigation data were obtained from the USDA-ARS research station in Greeley, and daily average precipitation data were collected from the CoAgMet Greeley 04 weather station.

Precipitation during the study period was minimal compared with irrigation inputs. Most rainfall events were light (< 5 mm), except for a few moderate showers and one larger event on DOY 248 (17 mm). These late-season rains provided supplementary moisture but contributed only marginally to the overall water availability of the fields shown in Fig. 4.2.

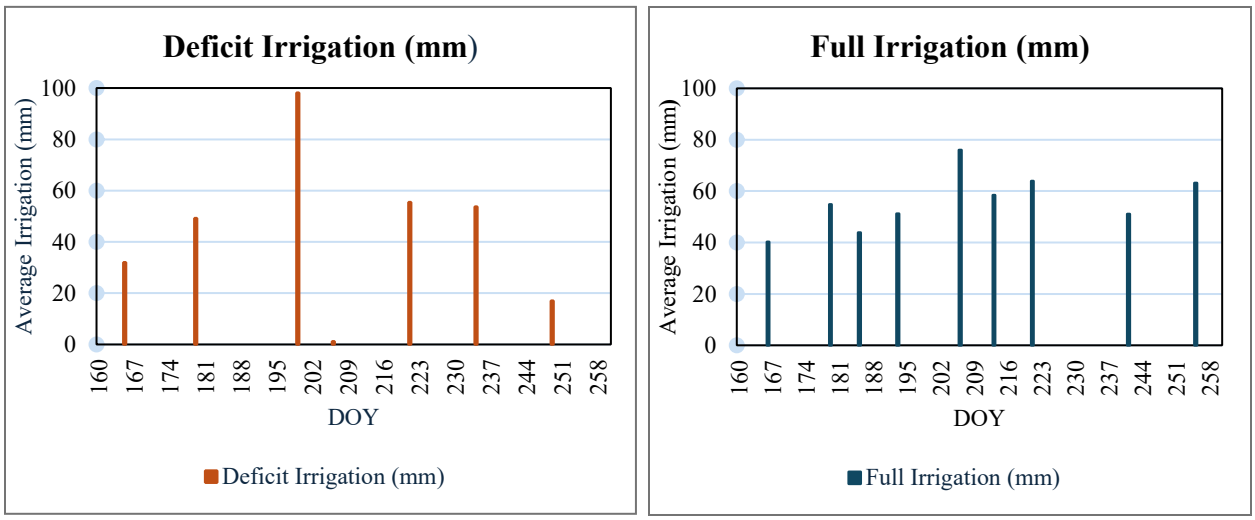

Fig. 4.1. Average irrigation depth (mm) and application dates for deficit irrigation (DI) and full irrigation (FI) treatments during the 2024 growing season.

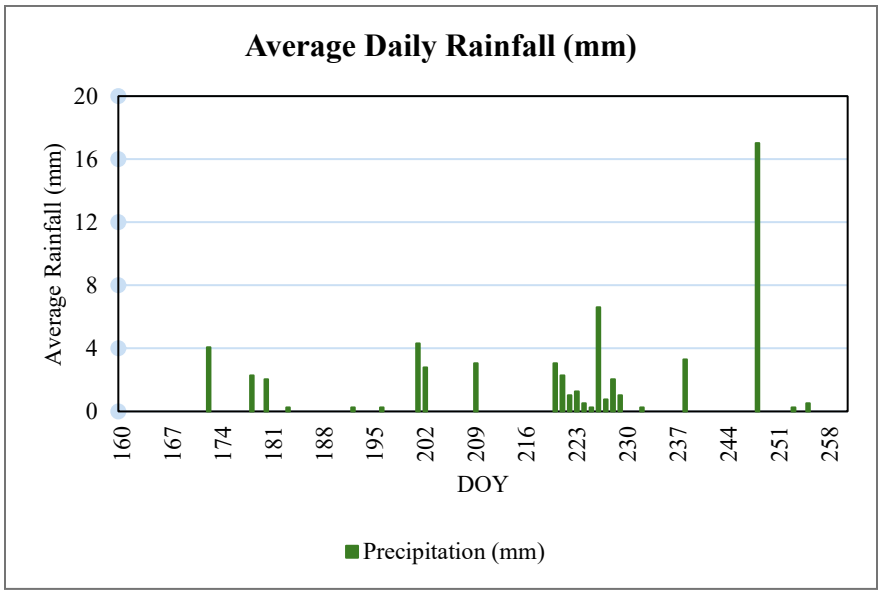

Fig. 4.2. Average daily precipitation (mm) recorded at the Greeley 04 CoAgMet weather station during the 2024 growing season.

4.2 Local Noon (11:00 – 01:00) Meteorological Conditions During the Growing Season

Meteorological data at local noon were analyzed from DOY 153 to 303, corresponding to July through October, using records from the CoAgMet Greeley 04 station. Noon observations were

selected because this period represents the time of peak net radiation and because it is close to the satellite and UAS overpass time, as well as the ground-based RS data collection.

Noon air temperature ranged from approximately 18 – 37 °C early in the season (DOY 153 – 200), with the highest temperatures observed in July and early August. A gradual decline followed, dropping below 15 °C toward late September and October. This seasonal cooling reflects decreasing solar decline and shorter day length, leading to reduced available energy for H and LE heat fluxes. As T_a decreases, the vapor pressure deficit (VPD) also declines, lowering the actual crop ET (ET_a) demand.

Solar radiation at noon ranged from 900 – 1000 W/m^2 during early July, then progressively decreased to 400 – 600 W/m^2 by October. The decline corresponds to the seasonal reduction in solar elevation angle and increased atmospheric scattering in the late season. High R_s values drive canopy heating and increase available energy for both LE and H, while later-season reductions in R_s limit overall flux magnitude.

Noon u_z fluctuated between 1 – 3 m/s, with short-term gusts reaching up to 7 – 8 m/s. Midseason stability and occasional gusts enhance turbulent transport, influencing aerodynamic resistance and promoting H and LE exchanges.

The RH values were low during July and August (20 – 40%) but increased substantially from September onward (40 – 80%). The inverse relationship between T_a and RH reflects typical continental summer patterns. Low RH combined with high R_s and T_a early in the season intensified VPD, maximizing ET and surface energy fluxes. As RH increased in the late season, the gradient for vapor transfer weakened, contributing to reduced ET rates or LE despite persistent soil moisture from irrigation or rainfall.

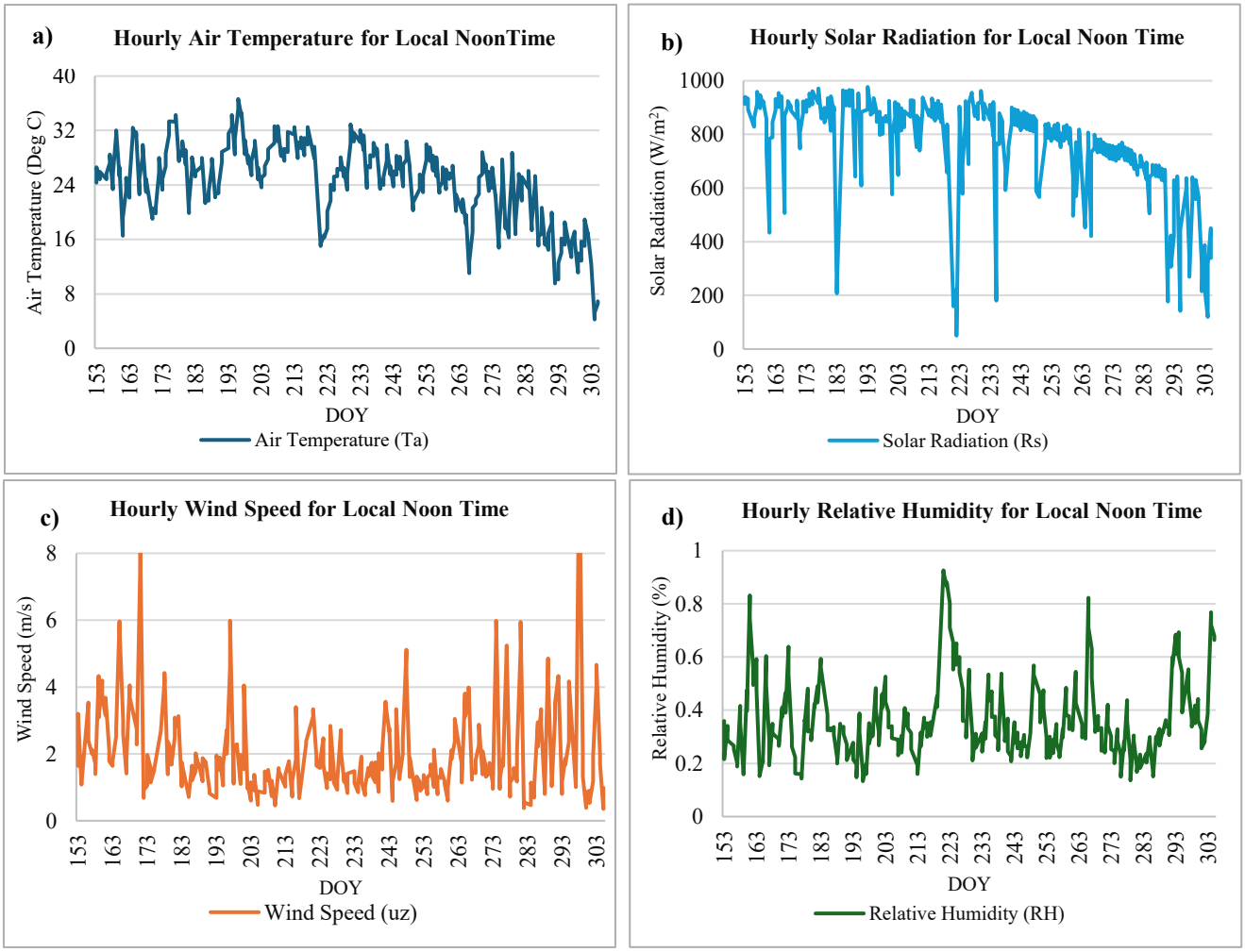

Fig. 4.3. Hourly meteorological variables at local noon (11:00 – 01:00) from CoAgMet Greeley04 station during the 2024 growing season (DOY 153 – 303). Panels show (a) air temperature (°C), (b) solar radiation (W/m^2), (c) wind speed (m/s), and (d) relative humidity (%).

4.3 PlanetScope Reflectance Band Values Processing and Calibration

4.3.1 PlanetScope Imagery Derived Spectral Trends and Noise Reduction

PlanetScope imagery for the fixed and MSR stations exhibited clear temporal variation in surface reflectance across all four spectral bands (red, green, blue, and NIR). These variations correspond to changes in crop canopy condition, soil type, and moisture conditions. Healthy vegetation absorbs red and blue light for photosynthesis, reflects green light, and strongly reflects NIR radiation due to internal leaf structure and water content.

Throughout the growing season, the FI field showed consistently higher NIR band SR (0.35 – 0.6) and lower red band SR (0.05 – 0.10), indicating a dense and vigorous canopy. In contrast, the DI field exhibited a lower NIR band, SR (0.25 – 0.35), and slightly higher red band SR (0.10 – 0.15), during the mid to late growth stages, suggesting water stress and reduced canopy vigor.

Thus, the raw time-series data contained noticeable fluctuations and irregular spikes caused by residual atmospheric effects, sensor noise, diversified soil textures, and different irrigation treatments, resulting in non-smooth reflectance trends when plotted against the dates. The plot for fixed EB stations is shown in Fig. 4.4, and the plot for the MSR stations is shown in Fig. A1 (Appendix D).

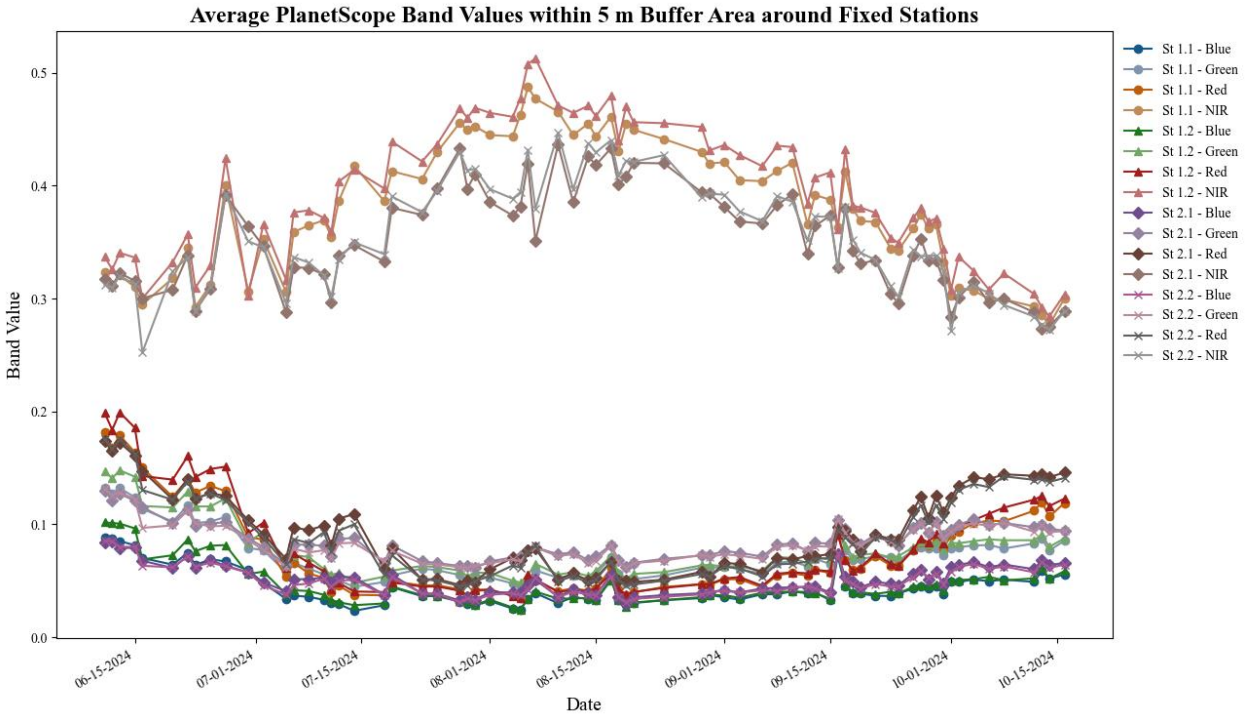

Fig. 4.4. Raw PlanetScope band reflectance values (RGB, and NIR) within 5 m radius buffer areas around fixed stations and during the 2024 growing season. The time-series plots show high-frequency fluctuations and irregular spikes caused by atmospheric scattering, illumination variation, and sensor noise, illustrating the need for polynomial smoothing in subsequent analyses.

To reduce variability in band values over time and capture the underlying spectral trends, a 5^{th}-degree polynomial was fitted to the temporal sequence of each band's mean values, providing the best overall performance in noise reduction. The accuracy of the 5^{th}-degree polynomial regression model was evaluated using the coefficient of determination (R^2) between observed and predicted reflectance values. Polynomial functions of degree 1 through 4 showed weaker correlations and less effective smoothing, while a 6^{th}-degree fit was tested but rejected due to overfitting and oscillatory behavior near data gaps. The 5^{th}-degree polynomial regression function consistently produced the highest R^2 across all spectral bands and both stations, effectively representing seasonal reflectance trends without amplifying noise. For all stations in the FI field, R^2 values exceeded 0.80 across all bands, indicating a strong model fit. In the DI field, R^2 values for the red

and NIR bands were slightly lower, typically around 0.70, reflecting greater spatial variability and heterogeneity within the field. However, no station exhibited an R^2 below 0.65, confirming satisfactory performance across all stations, including fixed and MSR stations (Appendix E). From these fitted polynomial equations, missing days' reflectance values were calculated, and all DOYs band values were available for every station.

4.3.2 Calibration Results of PlanetScope SR Raster Imagery Using MSR Observations

Using the fitted 5^{th}-degree polynomial equations, complete daily SR values were obtained for all stations and bands, including the dates corresponding to in-field MSR measurements. These continuous datasets for each band as SR, allowed a direct comparison between PlanetScope-derived and ground-measured MSR5 SR across 44 stations. The subsequent linear regression analysis demonstrated strong band-wise relationships between the two RS datasets, confirming that the smoothed PlanetScope SR data accurately represented surface conditions measured over the corn fields.

Linear regression analyses (Fig. 4.5) demonstrated that PlanetScope SR values slightly underestimated and overestimated MSR5-based SR measurements, with regression slopes close to unity and small positive intercepts. SR values in the blue and NIR bands exhibited the highest correspondence, while SR in the red and green bands showed slightly lower R^2 values, although larger than 0.75.

The PlanetScope SR calibration equations derived for each band were as follows:

- Blue band: $y = 1.3336x - 0.01$, $R^2 = 0.81$
- Green band: $y = 1.2882x - 0.0189$, $R^2 = 0.78$
- Red band: $y = 1.2241x - 0.0167$, $R^2 = 0.79$
- NIR: $y = 1.1535x - 0.0524$, $R^2 = 0.88$

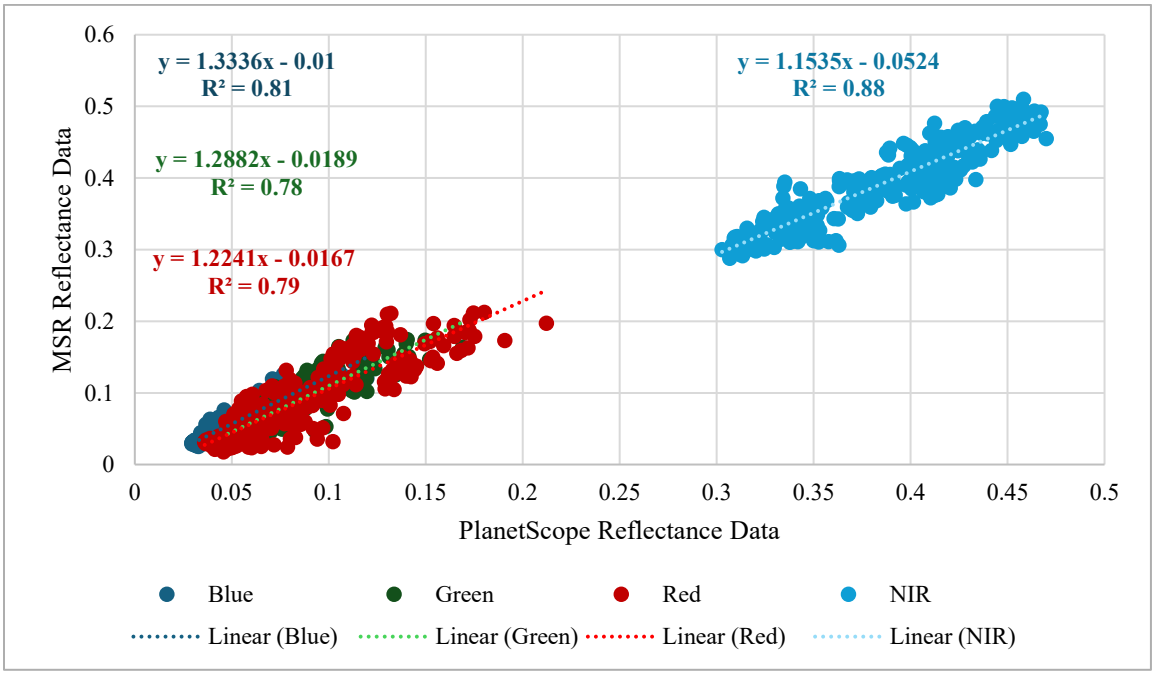

Fig. 4.5. Comparison of PlanetScope and MSR reflectance values with linear regression fit for four spectral bands.

Following application of these SR calibration regression equations to the cloud-masked PlanetScope SR imagery, the resulting calibrated SR values closely matched MSR5 SR measurements across all observation dates. Overall, the calibrations improved the radiometric accuracy of the PlanetScope SR imagery band values, reduced bias between satellite and field SR, and produced a spatially consistent, MSR5-based SR dataset.

4.3.3 Temporal Gap Filling and Seasonal Spectral Trends

After calibration, PlanetScope SR imagery was available only for specific acquisition dates. To ensure daily temporal continuity, missing PlanetScope SR images (by dates) were estimated using pixel-based linear interpolation, producing complete daily reflectance datasets for the study area across the growing season.

The interpolated SR imagery results, illustrated in Figures 4.6 and 4.7, show smooth and consistent spectral transitions without introducing noise or unrealistic fluctuations by extracting the average SR values per band from a 5 m radius buffer area for the fixed stations. In both fields, the NIR band SR values increased during the crop vegetative growth phase and declined toward maturity, while the red band SR values exhibited the opposite trend, decreasing during active canopy development and increasing again during senescence.

Clear differences were evident in the trend for SR and OSAVI across the growing season between the two irrigation treatments. The FI field maintained higher NIR-based SR and OSAVI values for a longer period with an early peak, indicating sustained canopy greenness under adequate soil water content conditions. In contrast, the DI field displayed a delayed peak and an earlier decline in NIR-based SR and OSAVI, as well as a quicker rebound in red reflectance, reflecting the onset of water stress and accelerated canopy drying.

These trends confirmed that the temporal interpolation effectively preserved realistic crop spectral dynamics, producing a biologically consistent dataset.

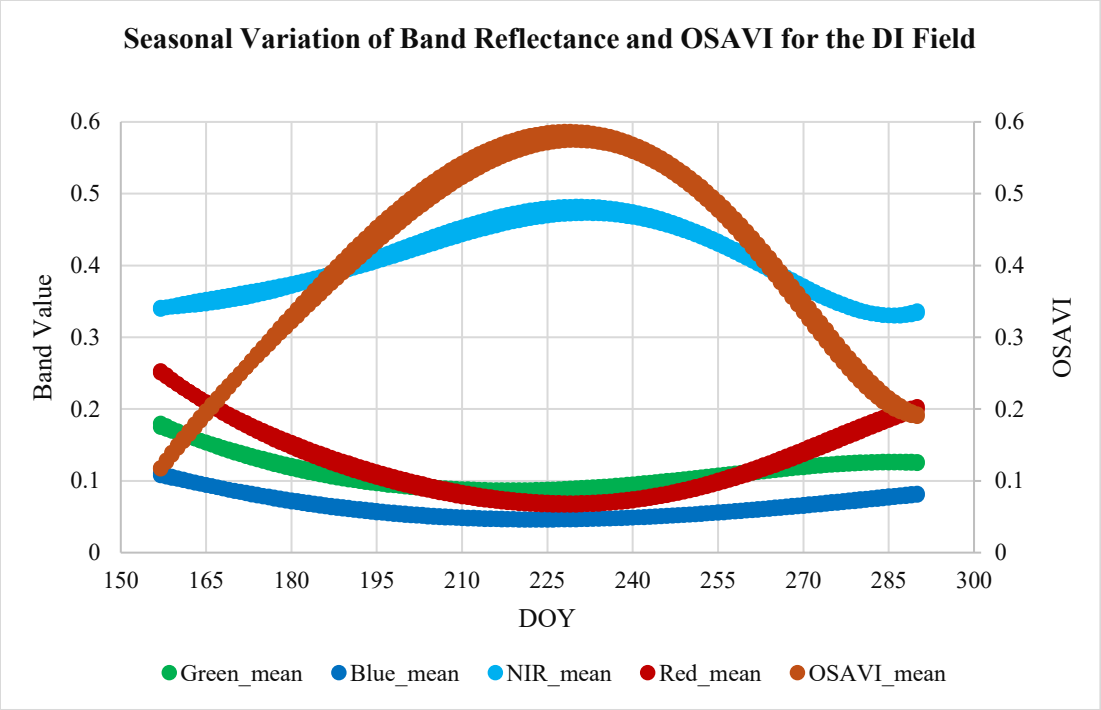

Fig. 4.6. Seasonal variation of band reflectance and OSAVI derived from PlanetScope raster imagery for the DI field, showing sustained canopy vigor and delayed senescence.

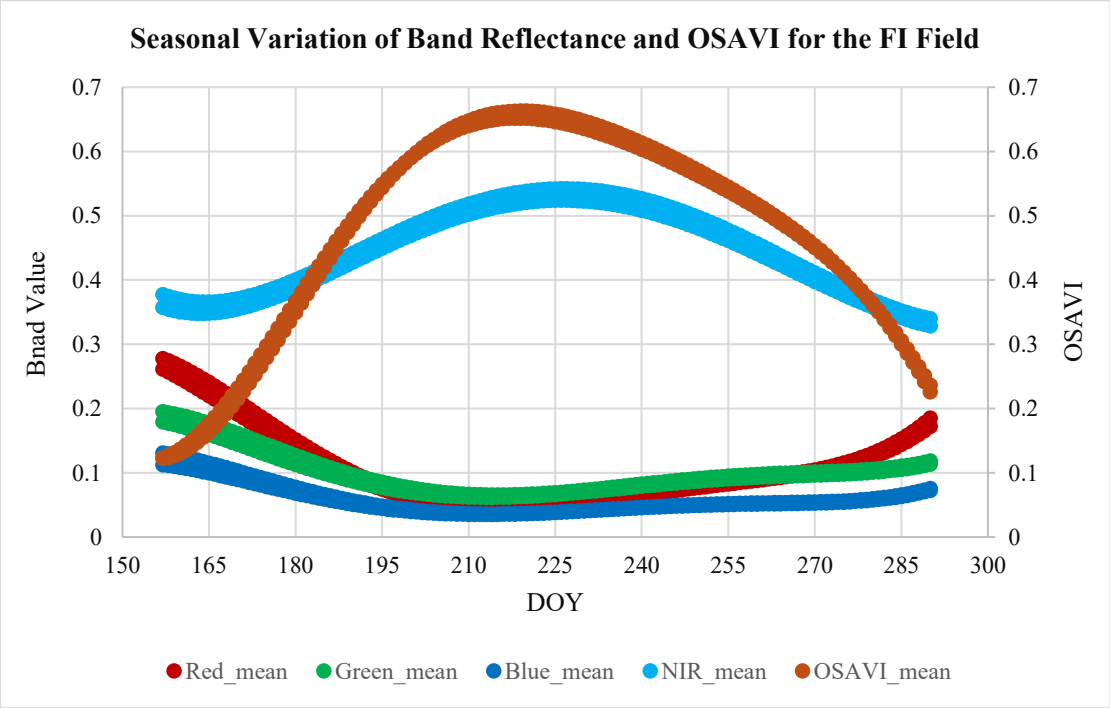

Fig. 4.7. Seasonal variation of band reflectance and OSAVI derived from PlanetScope raster imagery for the FI field, showing sustained canopy vigor and delayed senescence.

4.4 Performance Evaluation of the Pseudo Surface Temperature Model

4.4.1 Correction and Normalization of IRT (MSR5) Variation Across the Growing Season

Following the correction for ε_s and background radiation, MSR-based IRT measurements were normalized to exact noon conditions (12:00 pm MST) to align with PlanetScope overpass timing following the procedure indicated by Peters & Evett (2008).

IRT data affected by cloud cover or extreme deviations (beyond two standard deviations from the mean) were excluded to retain only representative canopy temperature values under clear-sky conditions. Clear-sky filtering was based on the variability of R_S, extracted from the CoAgMet "Greeley 04" station for the corresponding MSR SR and T_s measurement days (Fig. 4.8). Analysis of these records indicated that June 18 and July 19 were cloudy, while August 8 had a short clear period (11:40 am – 12:50 pm) without MSR data collection. August 21 showed clear conditions between 10:20 am – 12:25 pm, allowing partial data inclusion for that date. Additionally, MSR stations 1 E10 and 1 E11 were excluded from further analysis because their buffered zones overlapped with bare soil in the southwest portion of the field, which could bias canopy temperature estimates. These processes produced a consistent and physically meaningful dataset for evaluating surface temperature patterns across irrigation treatments.

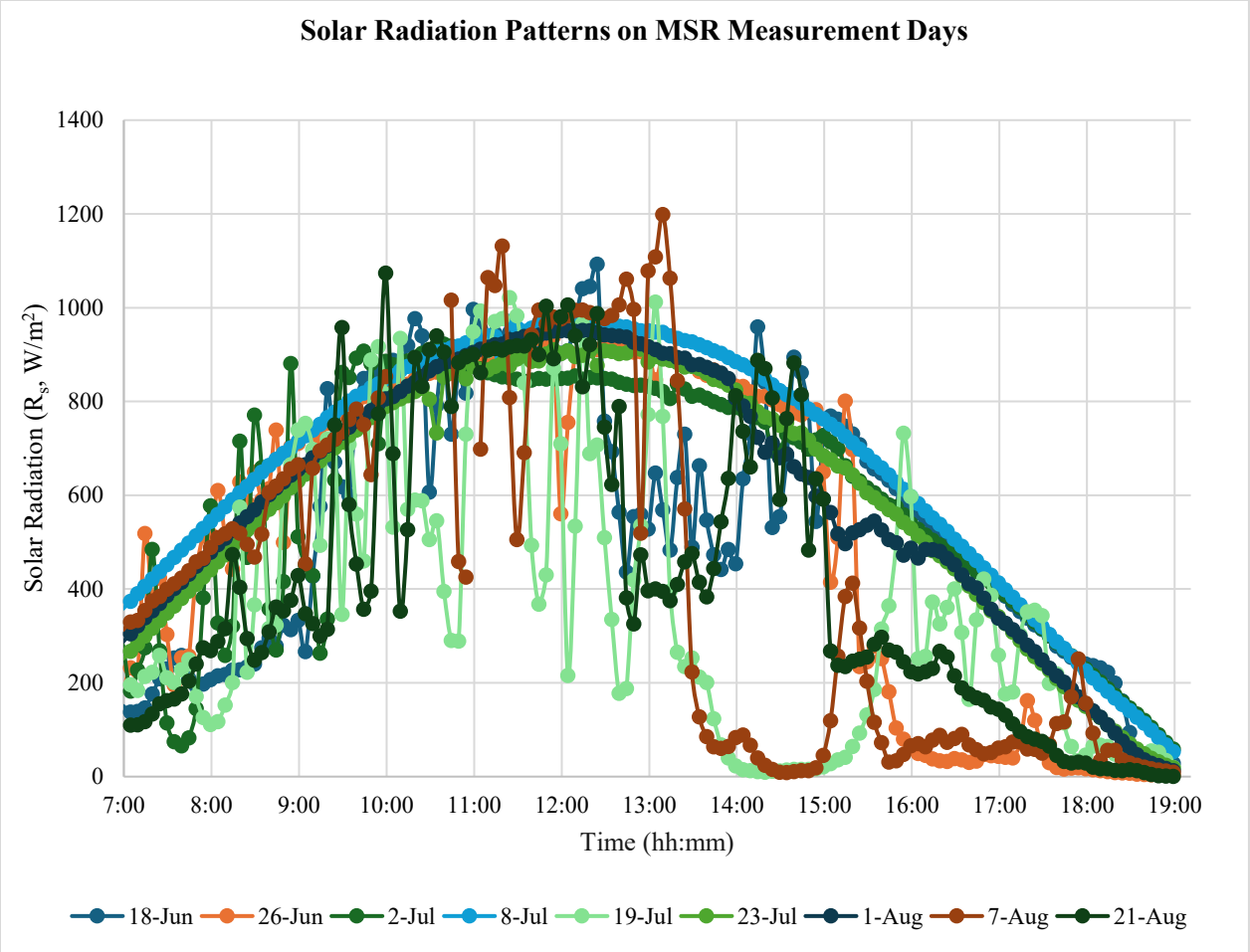

Figure 4.8. Fifteen-minute R_s (W/m²) data from the CoAgMet "Greeley 04" station on MSR measurement days, used to identify clear-sky and cloudy periods for filtering valid IRT-based Ts observations.

The calibrated IRT-based T_s values were summarized using boxplots (Figs. 4.9 and 4.10) to represent the temporal and spatial variation of canopy temperature in the FI and DI fields separately. The boxplots display the median, interquartile range (IQR), and whiskers (1.5× IQR), providing insight into both central tendency and variability of surface temperature. Outliers beyond the whiskers denote localized anomalies within the field.

In the FI field, the median IRT-based T_s values declined progressively from DOY 178 to 214, indicating canopy/surface cooling as vegetation cover and transpiration increased. The IQR

narrowed from approximately 5 °C at DOY 178 to 2 °C by DOY 214, reflecting reduced spatial variability as the canopy reached full and uniform coverage. Overall, the FI field exhibited strong evaporative cooling and thermal homogeneity as the season advanced.

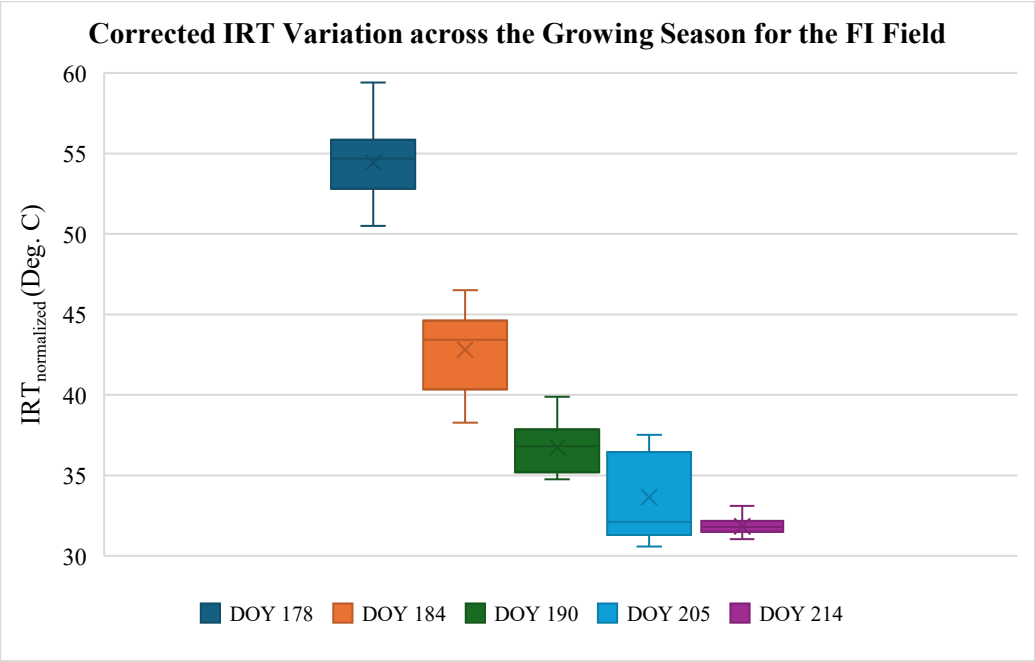

Fig. 4.9. Boxplot of corrected IRT-based T_s variation across the growing season for the FI field, showing decreasing median temperature and narrowing variability due to enhanced canopy cooling.

In the DI field, surface temperatures remained high during the early season and exhibited greater variability across all DOYs. The IQR ranged from 6 – 10 °C during midseason (DOY 184 – 214), showing strong spatial heterogeneity and uneven evaporative cooling. Wider boxes and longer whiskers indicate that canopy and soil temperature differences were more pronounced under limited water supply. Toward the late season (DOY 234), both median temperature and variability decreased, consistent with canopy senescence and declining transpiration.

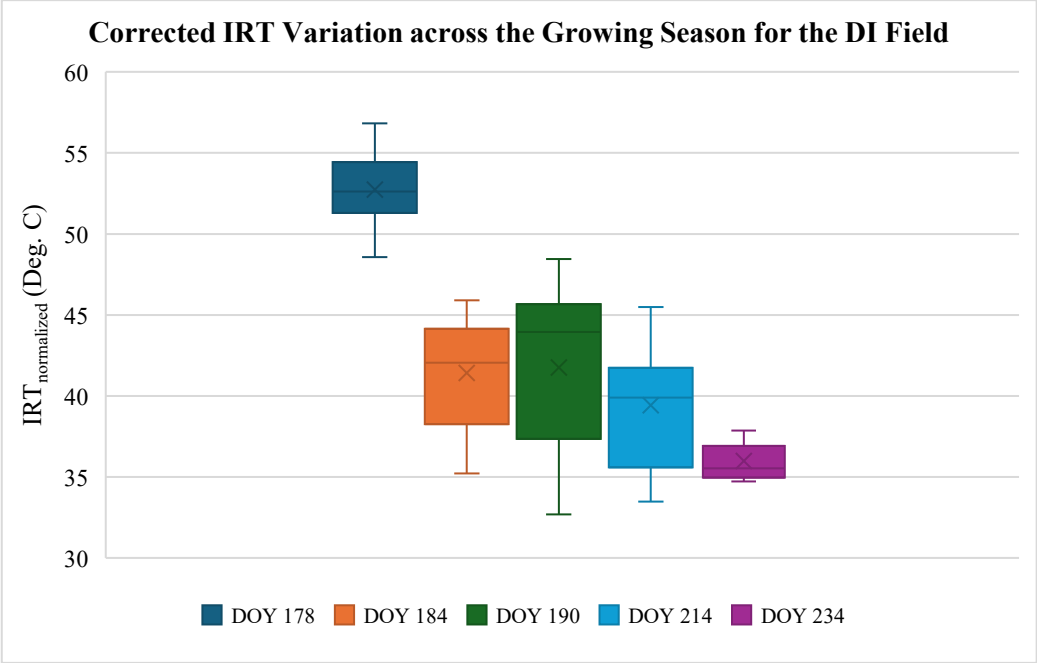

Fig. 4.10. Boxplot of corrected IRT-based T_s values variation across the growing season for the DI field, showing higher median temperature and wider variability associated with water stress and bare soil heating.

The FI field showed lower median IRT-based T_s values and narrower IQRs than the DI field, reflecting better evaporative cooling and uniform canopy conditions. In contrast, the DI field experienced higher and more dispersed temperature distributions, indicating uneven surface moisture and spatially variable thermal behavior due to water stress.

4.4.2 Results for OSAVI–IRT Relationships at MSR Stations

A strong inverse relationship was observed between surface temperature and OSAVI during the early and midseason phases of the growing period (Fig. 4.11), confirming that increased vegetation cover corresponded to lower canopy temperature due to enhanced transpiration and shading.

In Phase 1, the OSAVI - T_s relationship exhibited a pronounced exponential decay described by:

$$IRT = 78.091 \cdot e^{-1.502 \cdot OSAVI} \quad \text{.....(66)}$$

indicating that canopy temperature decreased rapidly with increasing OSAVI. The high coefficient of determination ($R^2 = 0.97$) reflects strong canopy-temperature sensitivity during this stage, as expanding vegetation led to effective evaporative cooling.

During Phase 2, the relationship remained negative and statistically robust:

$$IRT = 104.54 \cdot e^{-1.1786 \cdot OSAVI} \quad \text{.....(67)}$$

Although the correlation remained strong ($R^2 = 0.82$), the reduced R^2 value suggests that the canopy had reached a thermal equilibrium under dense vegetation, with high variation in temperature across the field due to its diverse character.

After September 6, data for SR and IRT from MSR were unavailable, so Phase 3 relationships were evaluated using fixed-station IRTs. These continued to show an inverse pattern, confirming that canopy temperature increased as vegetation cover declined with senescence.

Overall, the phase-wise analysis revealed that the OSAVI–IRT relationship is strongest during the early crop development period and remains reliable through midseason, capturing the dynamic thermal response of the canopy throughout the growing season.

The pseudo-surface temperature raster imagery, derived from this approach, was denoted as the MSR-based pseudo-surface temperature model (PSTM).

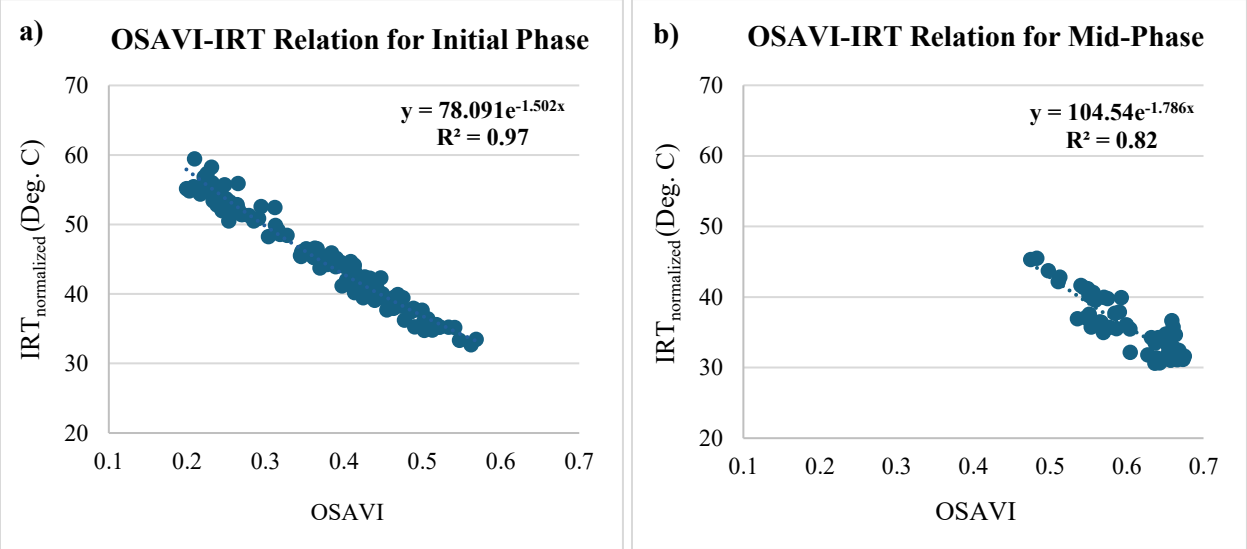

Fig. 4.11. Relationship between OSAVI and calibrated IRT-based T_s data derived from MSR measurements for (a) early growth (Phase 1) and (b) midseason (Phase 2). Both phases show strong negative exponential relationships, with higher sensitivity during early growth and stabilized canopy conditions during midseason.

4.4.3 Surface Temperature Results from Nadir-View IRT at EB Fixed Stations

Paired IRT-based T_s measurements from fixed stations equipped with both nadir and oblique sensors (ST 1.1, ST 1.2, and ST 2.2) were analyzed to develop regression relationships for estimating nadir canopy temperature (IRT_n) at stations with only oblique IRT sensors (ST 2.1 and EC1). Only clear-sky observations were retained to ensure physically consistent temperature-vegetation relationships.

Regression analysis between measured nadir and oblique IRTs' T_s data resulted in an R^2 value greater than 0.8, confirming the consistent angular behavior of canopy/surface temperature. OSAVI was initially incorporated to account for vegetation density effects; however, the

equation's regression coefficient was found to be statistically insignificant because both OSAVI and IRT-based T_s declined simultaneously during the late season (crop senescing). The Solver function in an MS Excel spreadsheet was used to optimize the regression parameters by minimizing the sum of squared differences between observed and estimated T_s, with the OSAVI coefficient constrained to zero, demonstrating that vegetation index variations did not improve prediction accuracy during the growth phase.

Among the regression models derived between nadir and oblique IRTs' T_s data, the best performance was obtained for stations in the DI field, expressed as:

$$IRT_n = -4.61 + 0 \times OSAVI + 1.239 \times IRT_o \quad \text{.....(68)}$$

with $R^2 = 0.86$. Relationships at FI stations were weaker ($R^2 \approx 0.5$) due to the more uniform canopy and narrower temperature range. So, the DI-field equation (Eq. 68) was adopted to estimate nadir canopy/surface temperatures for ST 2.1 and EC1 locations, which were both in the DI field.

The estimated nadir IRT-based T_s data were subsequently corrected for surface emissivity and background radiation effects, producing a set of clear-sky, thermal emissivity-corrected, nadir-equivalent canopy/surface temperatures for all fixed stations.

Validation was performed for estimated nadir IRT-based T_s separately for the Phase 2 and Phase 3 growth phases (Fig. 4.12), demonstrating high reliability of the regression. In mid-season, the regression model achieved excellent agreement between estimated and measured IRT-based Ts_n

(R^2 = 0.93), while the late season, the model maintained a strong correlation (R^2 = 0.84) with slightly higher scatter due to canopy senescence and exposed soil surfaces.

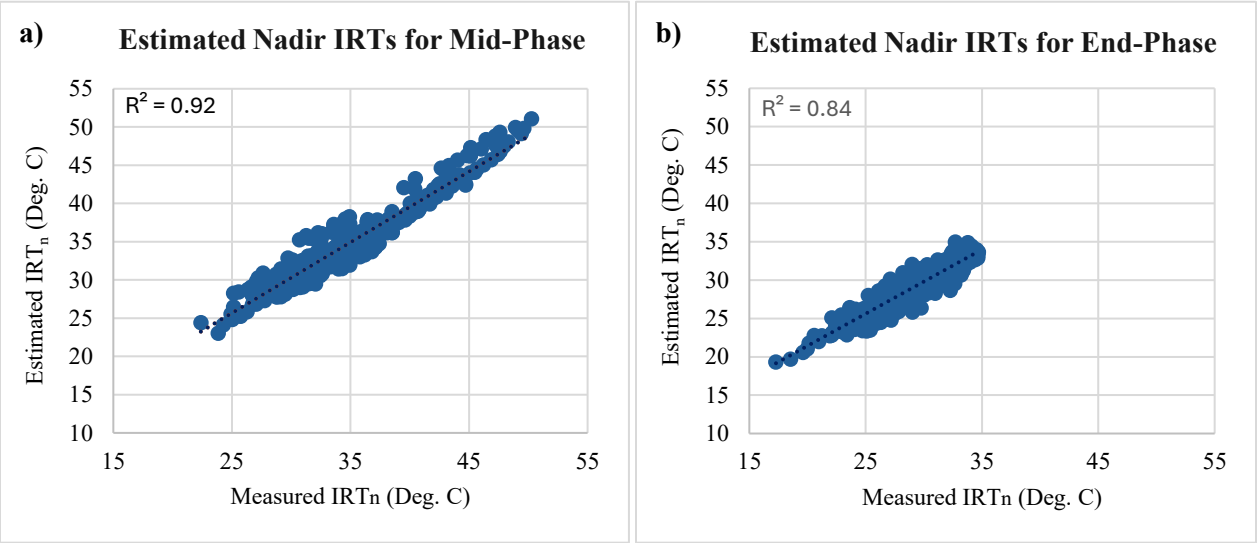

Fig. 4.12. Validation of estimated nadir T_{s_n} against measured values for the (a) middle and (b) end growth phases, showing strong linear relationships

These results confirm that oblique IRT T_s measurements can be accurately converted to nadir-equivalent canopy/surface temperatures, with the strongest model performance observed during midseason when canopy structure and surface thermal emissivity were most stable.

Next, OSAVI values were extracted for a 5 m radius area from the PlanetScope raster SR imagery for these five station points, and the OSAVI-T_s relationship was derived for every DOY with R^2 > 0.8. Using the corresponding regression equations from OSAVI-T_s relationships, raster imagery for T_s for every DOY was developed. The IRT-based T_s raster imageries were developed using T_s data from three EB fixed stations (ST 1.1, ST 1.2, and ST 2.2) IRT; therefore, the resulting PSTM was denoted as the three-point-based PSTM. Since this model was specifically developed from these three stations, only the raster imagery for the Phase 3 date range was used for analysis.

Finally, the raster imagery for T_s was generated from the T_s raster imagery for 12:00 pm for the local noon time span for every 30 minutes, as: 11:00 am, 11:30 am, 12:00 pm, 12:30 pm, 01:00 pm for every DOY to match the time step of the EC data, as described in section 3.4.7. This whole set of raster imagery for T_s (11:00 am to 01:00 pm) was defined as PSTM, represented as the canopy surface temperature, or T_s.

The integration of the PSTM concept represents a methodological advance over conventional UAV-based thermal sensing for this study. The uncooled microbolometer mounted on the UAV was sensitive to temperature drift, producing unstable thermal readings and limiting reliable use to 8 flight dates during the season. PlanetScope imagery also lacked thermal bands but supplied consistent near-daily surface reflectance around local noon. By linking these optical indices with in-situ temperature observations, the PSTM approach reconstructs a stable and spatially continuous proxy for canopy surface temperature over the 11:00 am – 01:00 pm period. This method overcomes the radiometric and temporal limitations of UAV thermal data and provides improved temporal coverage for energy-balance modeling throughout the growing season.

4.5 Performance Evaluation for Modeled Net Radiation

The evaluation of RS-based modeled R_n was conducted using two different PSTM sources: one derived from the MSR-based pseudo-T_s approach and the other from a three-point-based pseudo-T_s approach using fixed-station T_s temperatures. The ratio of field-measured to modeled R_n (Field/Estimated R_n) was analyzed over time for all four fixed stations, as shown in Fig. 4.13. Across both approaches, the majority of Field/Estimated R_n ratios clustered around unity, indicating that the modeled R_n values corresponded well with field observations. However,

differences were evident in the degree of variability and temporal stability between the two models.

The MSR-derived PSTM-based R_n (Fig. 4.13-a) demonstrated slightly higher temporal fluctuation compared to the three-point-based PSTM. The ratio (Field/Estimated R_n) values typically ranged between 0.8 and 1.3, with most data points closely distributed around 1.0, confirming that the MSR-derived PSTM-based R_n estimates were largely consistent with field-measured values. Occasional R_n spiked above 1.5 and dipped below 0.7, particularly after DOY 260, which may be attributed to canopy senescence, changing surface thermal emissivity, or atmospheric instability during late-season measurements.

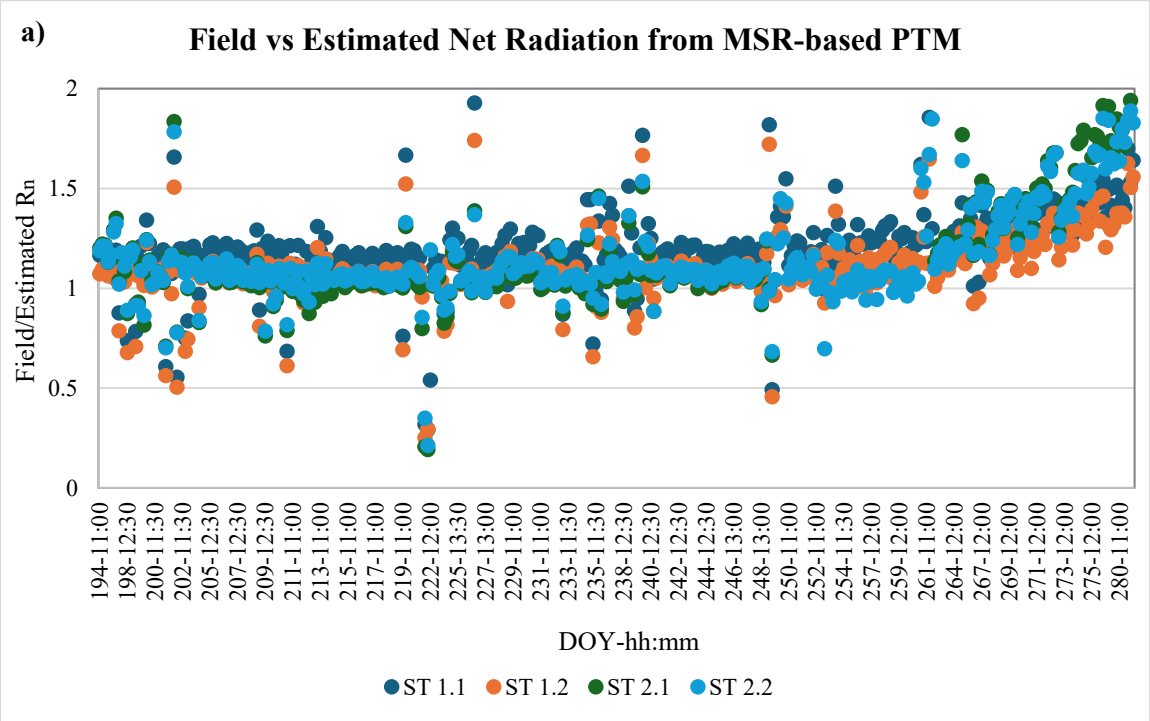

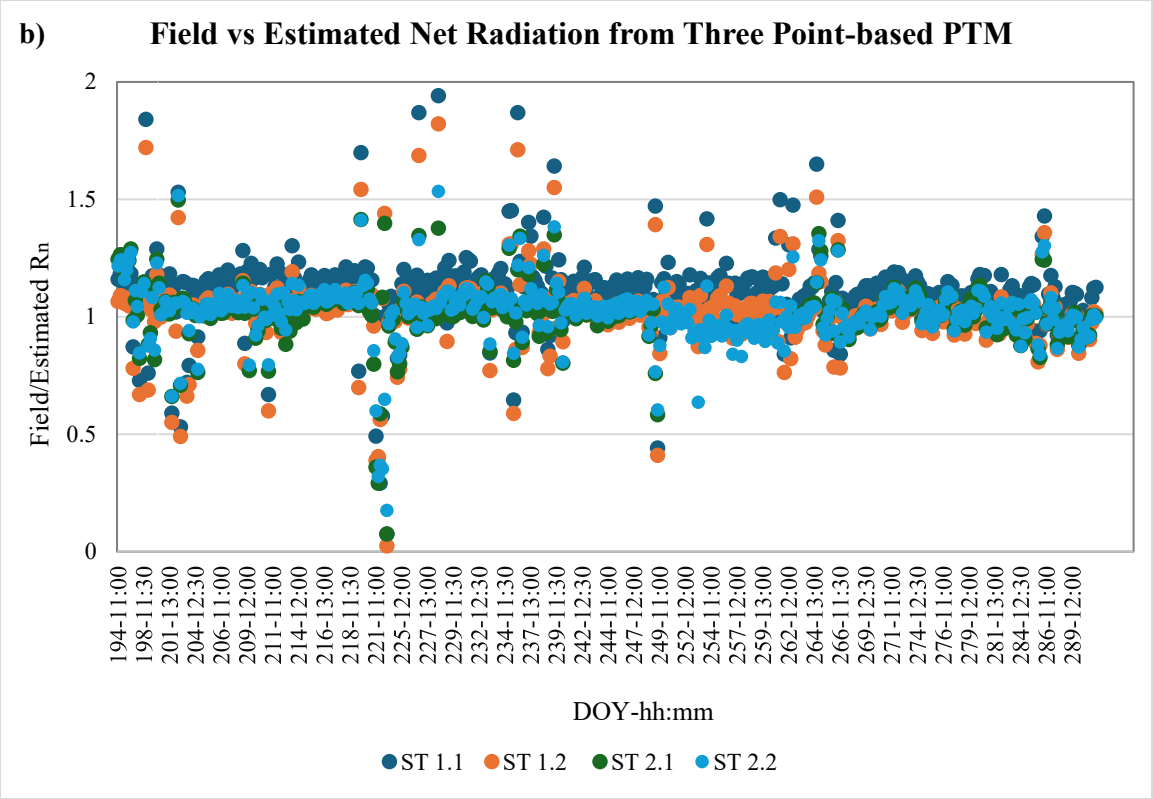

Fig. 4.13. Comparison of field-measured and modeled net radiation (R_n) ratios for (a) MSR-based pseudo-temperature model and (b) three-point-based pseudo-temperature model, showing generally strong agreement (ratios ≈ 1) with minor deviations during late-season periods.

The three-point-based PSTM (Fig. 4.13-b) produced smoother and slightly more consistent results than the MSR-derived PSTM R_n model. Ratios of Field/Estimated R_n remained mostly within 0.9 - 1.2, with fewer extreme outliers, reflecting a closer alignment between modeled and observed R_n across all stations. The reduced scatter suggests that the three-point interpolation captured local thermal conditions more uniformly, likely because it relied directly on fixed-station IRT-T_s values measured under comparable atmospheric conditions. However, this approach also showed minor underestimations and overestimations during midseason, potentially due to spatial averaging that reduced temperature gradients across the field. In late-season periods, the three-point-based PSTM model-based R_n showed good results compared to the MSR-derived pseudo-T_s-based R_n model.

These findings indicate that while the MSR-derived PSTM-based R_n approach better represents field-scale R_n spatial heterogeneity, the three-point-based PSTM-based R_n model offers smoother and more temporally consistent R_n estimation. For each fixed station, the R^2 was calculated for both approaches to assess the collinearity between the field and the estimated R_n. For all stations, R^2 values were equal to or greater than 0.9, giving high confidence in the raster imagery created for the net radiation.

4.6 Performance Evaluation Crop Height Model

UAS-derived CHM captured the spatial and temporal variation in canopy development across the study fields. Early-season CHMs showed low vegetation cover with distinct row structure, while later-season maps indicated dense, continuous canopies. However, the uncorrected UAS-based heights systematically underestimated the field-measured values, especially during mid to late growth stages when the canopy was tall and dense. This underestimation reflected the smoothing effect and limited canopy reconstruction typical of UAS-derived DSMs over homogeneous vegetation surfaces.

Regression analysis between field-measured and UAS-derived crop heights revealed a nonlinear relationship (Fig. 4.14), with UAS heights tending to saturate as true canopy height increased. The power regression equation is:

$$y = 1.5074x^{0.1727} \quad \text{.....(69)}$$

where y is H_c (m) from the field, and x is H_c (m) from UAS.

This relationship showed a high dispersion and strong underprediction of field heights, as indicated by the value of MBE = – 0.56 m, RMSE = 0.70, NMBE = – 46.81, and NRMSE = 58.65%. This confirmed that simple one-to-one scaling could not represent the canopy growth pattern accurately.

Applying the power-based calibration significantly improved the agreement between UAS and field observations. The corrected relationship (Fig. 4.15) followed a nearly one-to-one trend.

Post-calibration performance metrics indicated a substantial reduction in both systematic and random error (MBE = 0.05 m; RMSE = 0.25 m; NRMSE = 22.09%; NMBE = 4.79%). The improvement demonstrates that the calibration effectively compensated for height compression in the UAS-derived data.

The decision to adopt a power regression instead of a linear fit was supported by both the statistical results and the physical behavior of the canopy. At higher vegetation stages, the UAS DSM underrepresented canopy peaks due to surface smoothing and incomplete reconstruction, producing a nonlinear scaling between UAS and field heights. The power function captured this asymptotic response, providing more realistic estimates of tall crop canopies.

Overall, the calibrated CHM provided spatially consistent and physically reliable estimates of canopy height for the period DOY 200 – 271. The improved fit and reduced bias confirm that the

applied correction successfully aligned UAS-derived crop heights with in-field measurements, enabling their use in subsequent biophysical and flux analyses.

This CHM uniquely derives canopy height only from effective corn pixels identified within the study field. Non-crop areas were excluded to ensure that the model represents the true aerodynamic canopy rather than the surrounding bare or non-productive zones. This targeted approach refines the spatial domain of height estimation, improving the physical relevance of the derived d_o and subsequent EB calculations.

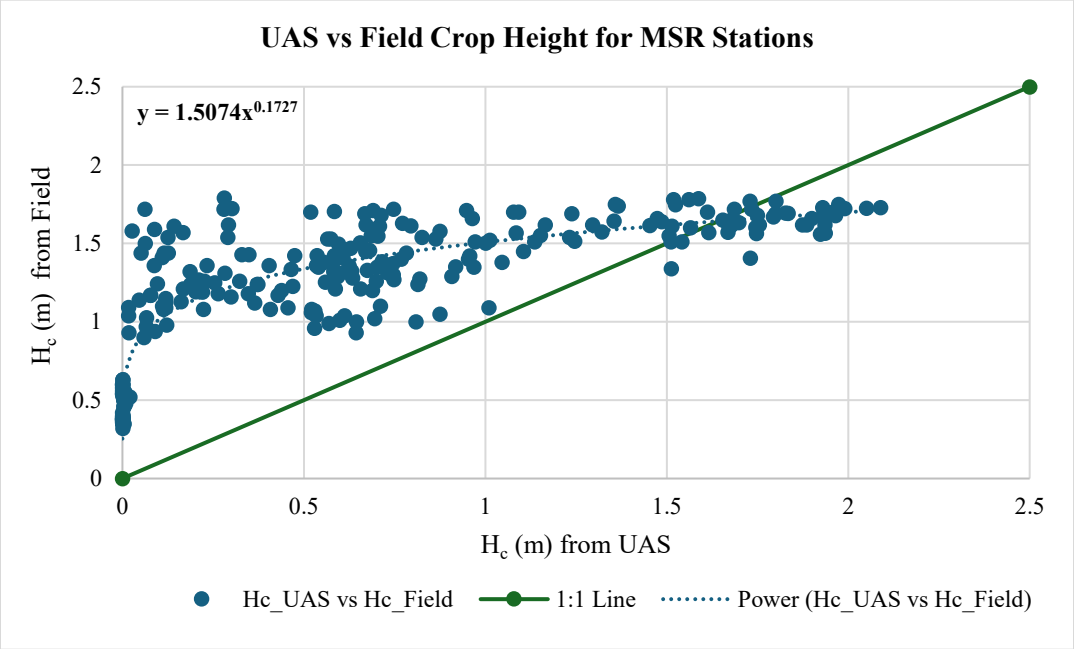

Fig. 4.14. Relationship between UAS-derived and field-measured crop heights at MSR stations showing systematic underestimation by UAS data and a nonlinear fit described by a power regression.

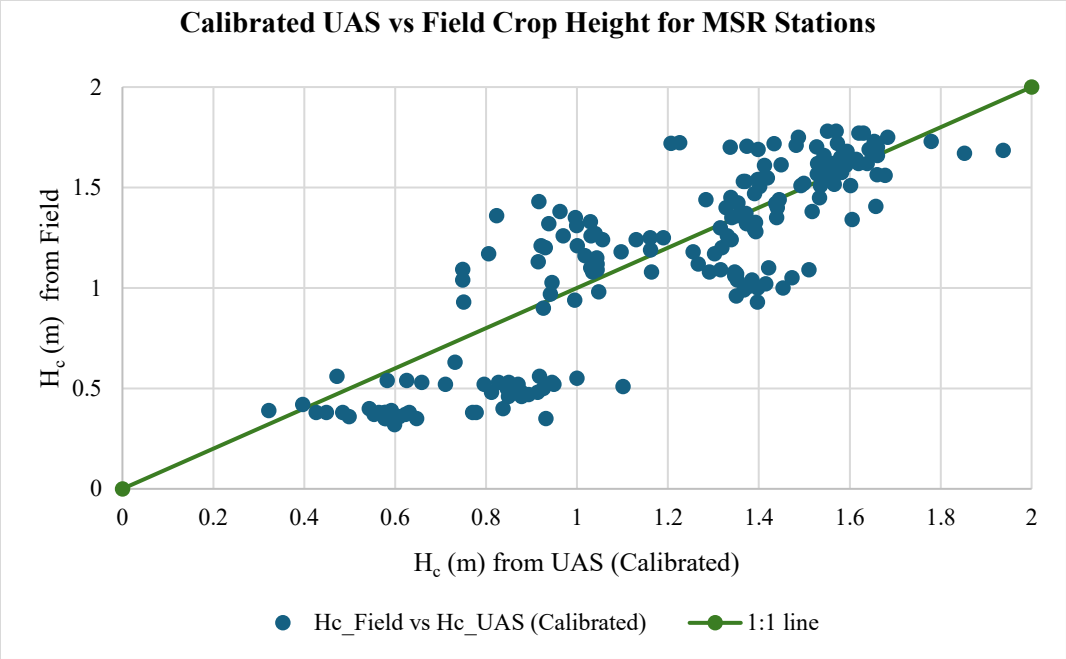

Fig. 4.15. Relationship between calibrated UAS-derived and field-measured crop heights at MSR stations showing improved agreement and near one-to-one correspondence after applying the power-based correction.

4.7 Results for Gap Filling of UAS-Derived Crop Height Data

After calibration, portions of the canopy height raster (CHM) for DOY 190 and DOY 200 remained incomplete, particularly within the DI field, due to cloud obstruction and data loss during UAS processing. These data gaps disrupted spatial continuity in the canopy structure and prevented H_c values extraction for several MSR stations located within the missing regions.

Gap-filled CHMs restored the continuity of canopy structure across the field and provided spatially coherent H_c patterns consistent with adjacent dates. Early reconstruction using a 2-degree polynomial approach produced unrealistically high mean values (~1.26 m for DOY 190), while the refined logistic-based estimation yielded mean heights of 1.09 m for DOY 190 and 1.18 m for

DOY 200, which were satisfactory. These estimates aligned with the expected crop development stage H_c values, representing moderate growth before full canopy closure.

Before Gap filling	After Gap filling
DOY 200	DOY 200
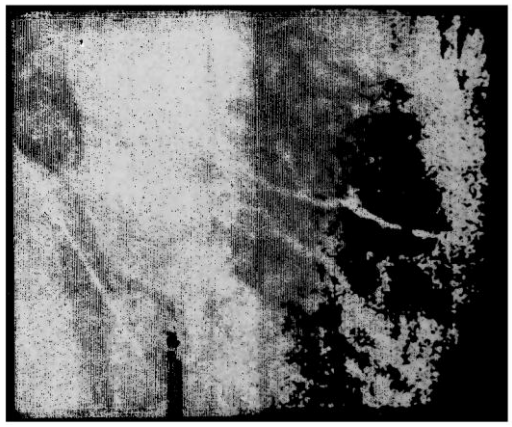	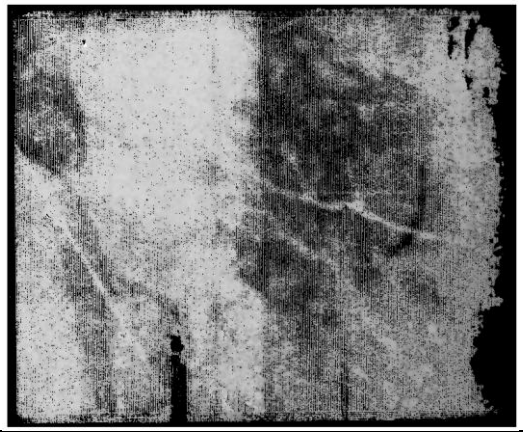
DOY 190	DOY 190
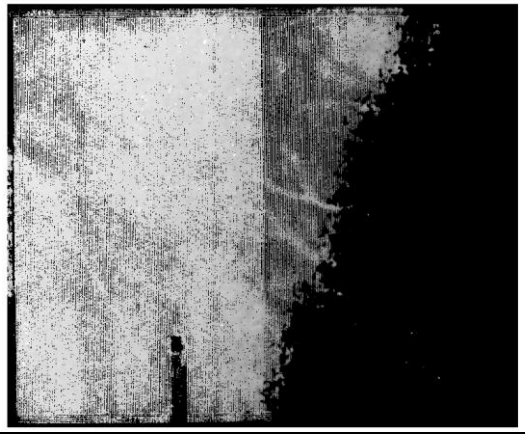	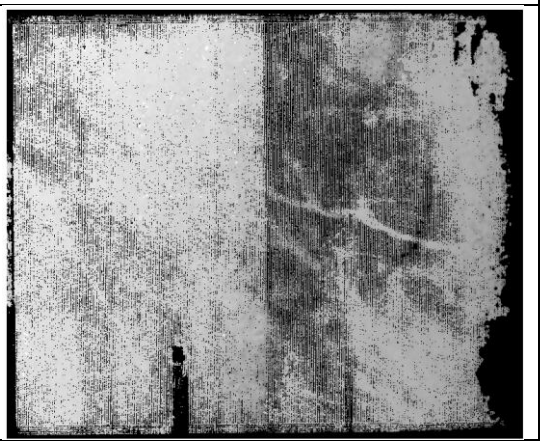

Fig. 4.16. Comparison of UAS-derived crop height maps before and after gap filling for DOY 200 and DOY 190. The post-processed raster imagery shows restoration of missing canopy regions and improved spatial continuity across the study field.

The spatial scaling of the reconstructed raster imagery using complete reference imagery preserved the natural variability between the full- and deficit-irrigated zones. As shown in Fig. 4.16, the filled H_c raster images exhibited smoother transitions and realistic height gradients compared with the fragmented and patchy appearance prior to gap filling. The vegetation mask applied afterward

effectively excluded soil and non-crop pixels, enhancing the precision of canopy-only height representation.

Validation against field-measured heights confirmed that the reconstructed canopy heights were within the expected range for both irrigation regimes, with no apparent artificial trends introduced by interpolation. The completed CHM series from DOY 190 - 271 thus provided a continuous, physically consistent canopy height dataset.

4.8 Evaluation of Crop Height and Zero-plane Displacement Height Models

The UAS-derived H_c values demonstrated a clear temporal growth pattern consistent with crop phenology. As shown in Fig. 4.17, the mean H_c, increased sharply from DOY 190 to approximately DOY 230, corresponding to the active vegetative stage, followed by a gradual decline during the senescence phase. The UAS-based H_c estimates reflected smooth and continuous changes across the growing season, indicating accurate structural characterization of the canopy.

When 'measured' (calibrated) H_c models were compared to the existing empirical RS-based H_c models, notable variations were observed in both the magnitude and trend of the estimated H_c. The Anderson et al. (2004) model consistently underestimated canopy height throughout the season, showing limited sensitivity to growth dynamics. The Arslan et al. (2022) model underestimated H_c during the early growth period but overestimated values beyond DOY 220, indicating excessive responsiveness to vegetation index fluctuations. In contrast, the Costa-Filho et al. (2021) H_c model aligned most closely with the UAS-derived H_c values, underestimating slightly during early and late stages but capturing mid-season growth peaks effectively.

Quantitative evaluation confirmed that Costa-Filho et al. (2021) achieved the highest accuracy, with an RMSE of 1.301 m and a near-zero mean bias error (MBE = 0.14 m). The Arslan et al. (2022) and Anderson et al. (2004) models yielded larger discrepancies (RMSE = 10.62 m and 9.52 m, respectively), reinforcing the superior consistency of the (Costa-Filho et al., 2021) model for representing canopy height under field conditions.

The d_o calculated from the existing models exhibited a similar temporal trend to H_c, increasing during canopy expansion and declining during the senescence stage (Figure 4.18). Among the evaluated d_o models, the (Brutsaert, 1982) formulation showed the linear relationship with H_c, which is obvious because in d_o is a fraction of H_c. The Shaw & Pereira (1982) model followed a comparable trend but produced slightly higher variability, likely due to the inclusion of canopy drag effects. The Pereira et al. (1999) model exhibited the greatest variability and produced the most diverse results, likely reflecting its higher sensitivity to LAI fluctuations, field heterogeneity, crop orientation, and air penetration effects.

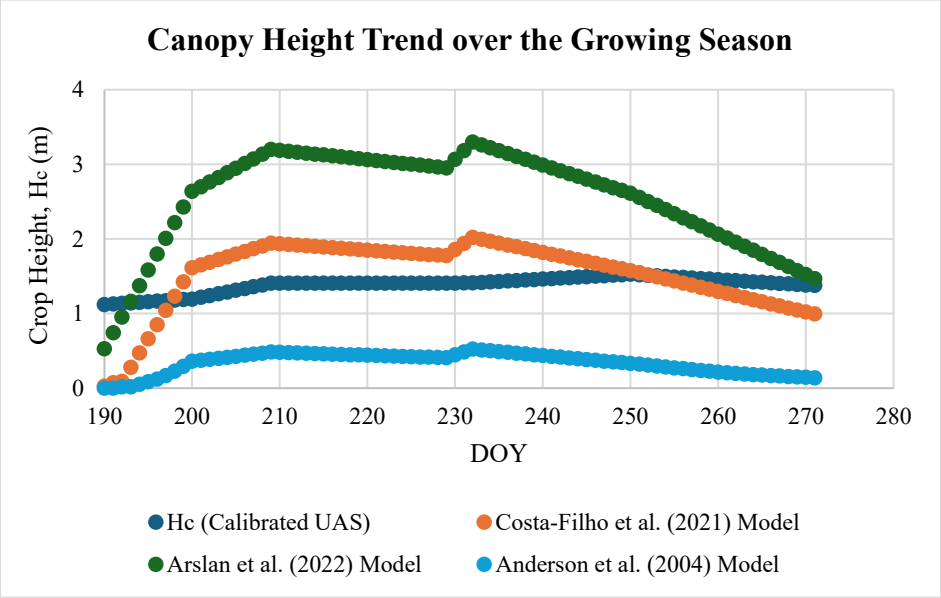

Fig. 4.17. Crop Height (H_c) growth over the season. Comparison of UAS-derived H_c with modeled H_c (Anderson et al., 2004; Arslan et al., 2022; Costa-Filho et al., 2021).

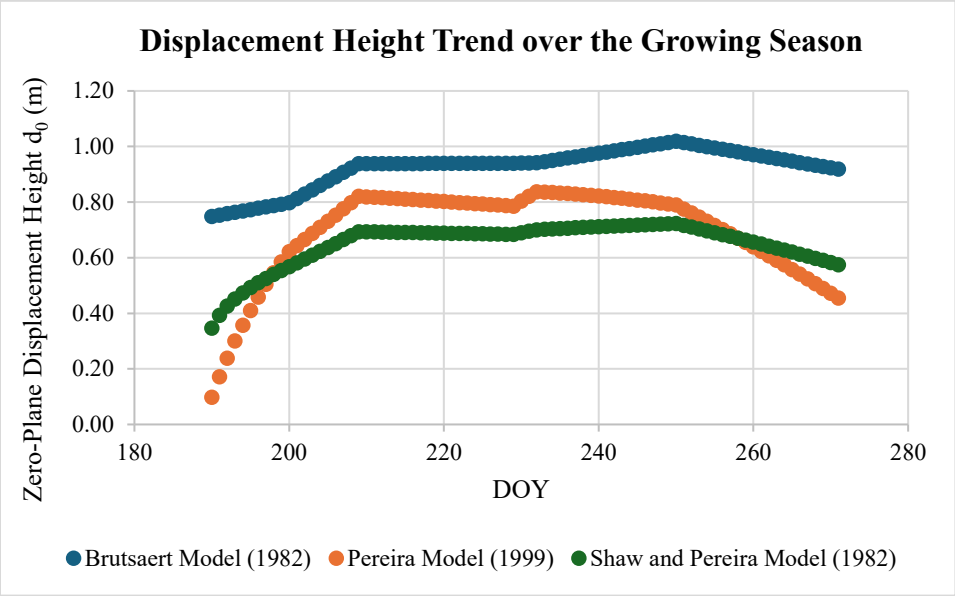

Fig. 4.18. Changes of Zero-plane Displacement Height (d_o) over the growing season. Comparison of d_o, estimated from Brutsaert (1982), Shaw and Pereira (1982), and Pereira (1999) models.

4.9 Characterization of Measured d_o Dynamics and Physical Plausibility

The d_o, derived from EC-based u_* and u_z (as described in Section 3.9), regarded as measured d_o was analyzed to evaluate physical consistency.

The resulting 'measured' d_o values were classified into three ranges:

i. $0 < d_o < H_c$,

ii. $d_o < 0$,

iii. $d_o > H_c$,

To investigate the reason behind the physically unrealistic values of d_o ($d_o < 0$ and $d_o > H_c$) analysis was done by generating wind roses to simulate the pattern of wind and canopy interactions, while also considering the wind speed shown in Fig. 4.19. The θ, expressed as the azimuth angle

measured clockwise from north, illustrates the prevailing flow orientation. The vector lengths indicate the intensity of u_z along the X and Y axes, while the d_o values were color-coded into three categories, based on the conditions as described previously, to visualize their distribution and variation for every 30-minute interval for the entire growing season.

To ensure a physically realistic aerodynamic representation, the d_o values were constrained within the canopy height range as:

i. If: $0 < d_o < H_c$, then $d_o = d_o$;

ii. If: $d_o < 0$, then $d_o = 0$;

iii. If: $d_o > H_c$, then $d_o = H_c$;

The corrected and constrained values were subsequently used as EC-derived measurements for the d_o model development.

Negative or excessively high d_o values were observed mainly during the early and late crop growth stages, when canopy density and aerodynamic roughness were low. At these stages, the larger open spaces within the corn rows allowed deeper wind penetration, which gradually decreased as the canopy developed and surface roughness increased. This occasionally resulted in physically unrealistic d_o estimates, reflecting limitations in the adopted estimation procedure and highlighting the need to constrain results within physically plausible ranges.

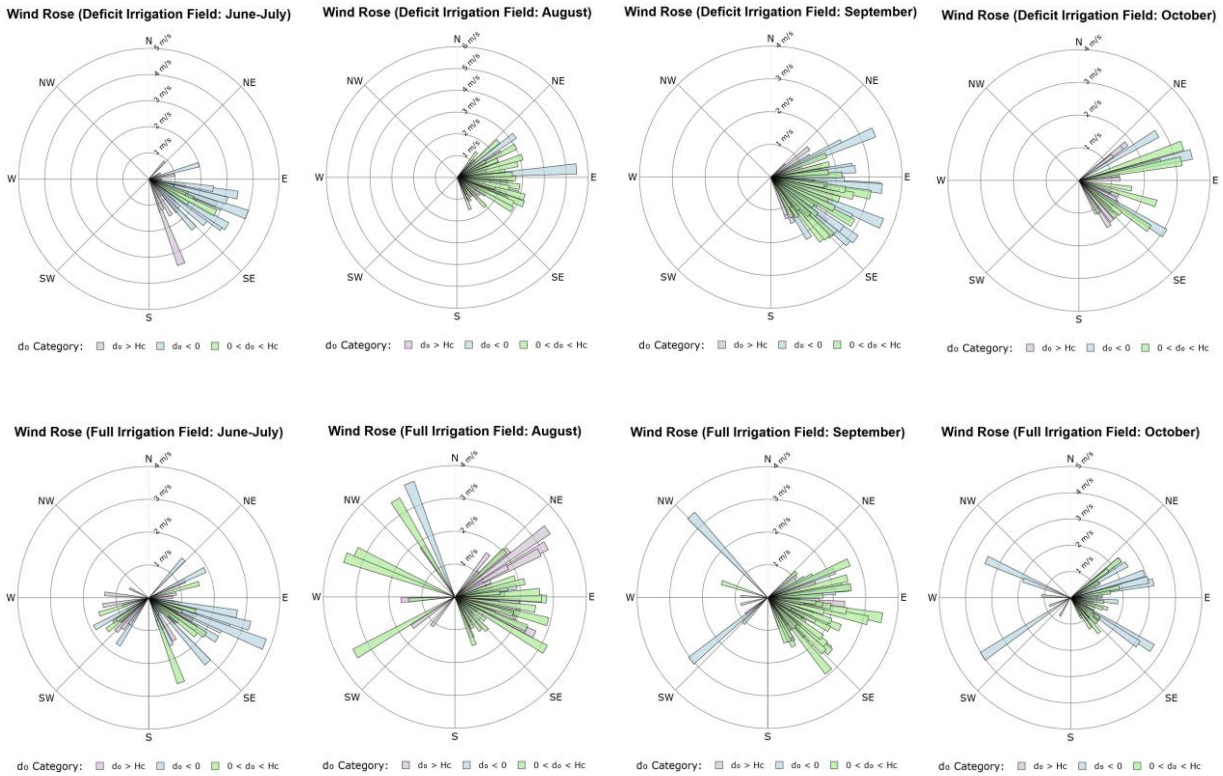

Fig. 4.19. Seasonal wind rose diagrams for deficit irrigation (DI) and full irrigation (FI) fields from June to October, showing wind direction (θ), speed (u_z), and categorized zero-plane displacement height (d_o): $d_o > H_c$(red), $d_o < 0$ (blue), and $0 < d_o < H_c$ (green). The plots highlight seasonal and irrigation-specific variations in canopy-wind interactions, with realistic d_o values ($0 < d_o < H_c$) prevailing during the peak growth period (August–September) and higher variability under sparse canopy conditions early and late in the season.

4.10 Sensible Heat Flux Estimation from Zero-Plane Displacement Height Models

4.10.1 New Empirical Dynamic 'd_o' Model Formulation

Two multiple linear regression d_o models were developed for the corn fields in the. The produced 'd_o' models dynamically estimate d_o from measured canopy structure and wind flow characteristics. The two d_o models differed in which canopy descriptor they used:

- Model 1 used the weighted Φ_{dp} (crop porosity) as the primary predictor:

$$d_o = 1.72 - 0.361\ u \cdot \Phi_{dp} - 0.038\ \Delta T - 0.322\ u \cdot \sin(\theta_{rel}) \quad \text{.....(70)}$$

- Model 2 used the weighted f_{veg} (fractional vegetation cover) as the primary predictor:

$$d_o = 1.16 + 0.617 \cdot f_{veg} - 0.039\ \Delta T - 0.359\ u \cdot \sin(\theta_{rel}) \quad \text{.....(71)}$$

Both models included additional variables to account for thermal and wind directional (interaction with crop row orientation) effects on d_o. These predictor choices were based on the hypothesis that d_o is affected not just by how much vegetation there is (quantity and arrangement of canopy), but also by how the wind speed, direction, and temperature conditions interact with the crop/canopy row orientation.

4.10.2 Training and Validation of the New Empirical Dynamic 'd_o' Model

The two d_o models achieved similar performance in terms of statistical predictive accuracy for the tested data set with the training dataset, explaining on the order of 40 - 50% of the variance in half-hourly d_o. The Φ_{dp}-based model yielded a coefficient of determination $R^2 \approx 0.39$ on the training set and ~0.48 on the independent test set. The f_{veg}-based model was virtually the same, with $R^2 \approx$ 0.39 (train) and ~ 0.47 (test). Error magnitudes were moderate: the MAE for d_o was around 0.33 m for both models, and the NRMSE was approximately 43%.

Other evaluation metrics likewise indicated modest predictive power (e.g., a Nash–Sutcliffe efficiency of ~ 0.48 and d_r of ~ 0.68 on the test set for both formulations). It is noteworthy that performance on the test data was slightly better than on the training data, suggesting no overfitting; in fact, the randomly selected training subset appeared to exhibit more scatter, as tabulated in Table 4.1.

Table 4.1: Statistical Performance of the Φ_{dp} based and f_{veg} based d_o model for the entire field.

Main Parameter	**Data Set**	**R^2**	**MAE**	**NMAE**	**MAD**	**RMSE**	**NRMSE**	**NSE**	**NNSE**	**d_r**
Unit		**-**	**m**	**%**	**m**	**m**	**%**	**-**	**%**	**-**
Φ_{dp}	Train	0.39	0.36	35.77	30.24	0.46	45.48	0.39	0.62	0.64
	Test	0.48	0.34	33.42	27.11	0.43	42.42	0.48	0.66	0.67
f_{veg}	Train	0.38	0.36	35.73	29.80	0.46	45.60	0.39	0.62	0.64
	Test	0.47	0.34	33.52	29.55	0.43	42.86	0.47	0.66	0.68

4.10.3 Performance Evaluation of New Empirical Dynamic 'd_o' Models for Estimating H and LE Heat Fluxes

The Φ_{dp}-based d_o model, used for estimating the H flux, was characterized by a good overall agreement when compared with the corrected measured H values. The MAE was 37.18 W/m^2, corresponding to a normalized MAE of 22.27%. The RMSE was 67.86 W/m^2 (NRMSE = 44.30% of the mean observed flux). Other performance indices further reflect good model fidelity: the NSE

reached 0.69, the normalized NSE was 0.76, and the d_r was 0.73. These statistics indicate a high degree of accuracy and relatively low error spread for the Φ_{dp}-based approach.

Similarly, the f_{veg}-based d_o model, used for estimating the H flux, achieved very comparable results. The MAE was 37.20 W/m^2 (NMAE = 22.2%), and the RMSE was 68.00 W/m^2 (NRMSE = 44.7%). The NSE attained was 0.69, with a normalized NSE of 0.76, and the index of agreement d_r was 0.73. All metrics (Table 4.2) for the f_{veg}-based model were essentially indistinguishable from those of the Φ_{dp}-based model, differing only in the third decimal place. This parity in statistical performance suggests that both modeling approaches fit the data equally well, with no significant loss of accuracy when using the simpler f_{veg} predictor.

Table 4.2: Statistical parameters for the estimated H by adopting Φ_{dp}-based and f_{veg}- based d_o model for the entire field data.

Main Parameter	**MAE**	**NMAE**	**MAD**	**RMSE**	**NRMSE**	**NSE**	**NNSE**	**d_r**
Unit	W/m^2	%	W/m^2	W/m^2	%	-	%	-
Φ_{dp}	37.18	22.27	67.86	44.31	26.54	0.69	0.76	0.73
f_{veg}	37.19	22.18	68.00	44.69	26.64	0.69	0.76	0.73

The performance of the Φ_{dp}-d_o and f_{veg}- d_o models in estimating H flux under DI and FI conditions are presented in Figure 4.20 (a - d). Each panel compares the corrected measured H against the model-estimated flux H for both irrigation regimes.

Figure 4.20a and 4.20b illustrate the measured (corrected) vs. modeled H under DI for the Φ_{dp}-d_o and f_{veg}-d_o models, respectively. In both cases, H data points align closely with some under- and overestimations along the 1:1 line at low to mid-range fluxes, with a similar pattern of scatter throughout the growing season, with an R^2 value of 0.7.

Under FI treatment (Fig. 4.20c, d), both d_o-based H estimates continue to track measured H closely, maintaining a strong linear correspondence (points largely clustered around the 1:1 line, consistent with R^2 in the 0.70 - 0.80 range). As in the DI case, fluxes below ~200 W/m² are tightly clustered along the parity line, reflecting minimal bias in this lower range for both models. At higher flux values in the FI treatment (which are less frequent due to ample moisture), the data show a slight increase in dispersion.

Similarly, Figure 4.21 compares corrected (observed) versus model-estimated LE for two different d_o models (Φ_{dp} and f_{veg}) under DI and FI treatments. In subplots (a) and (b), the scatter of points is clustered along the 1:1 line, indicating that the models closely reproduce the measured LE with negligible bias ($R^2 = 0.88$) across low to high flux values.

For the FI treatment, subplots (c) and (d) similarly illustrate a high correspondence between measured and estimated LE for the models, with data points in both cases clustering near the 1:1 line. The Φ_{dp} approach and the f_{veg} approach produces a marginally wider scatter of points ($R^2 = 0.93$). Overall, LE was predicted with higher accuracy than H across the dataset.

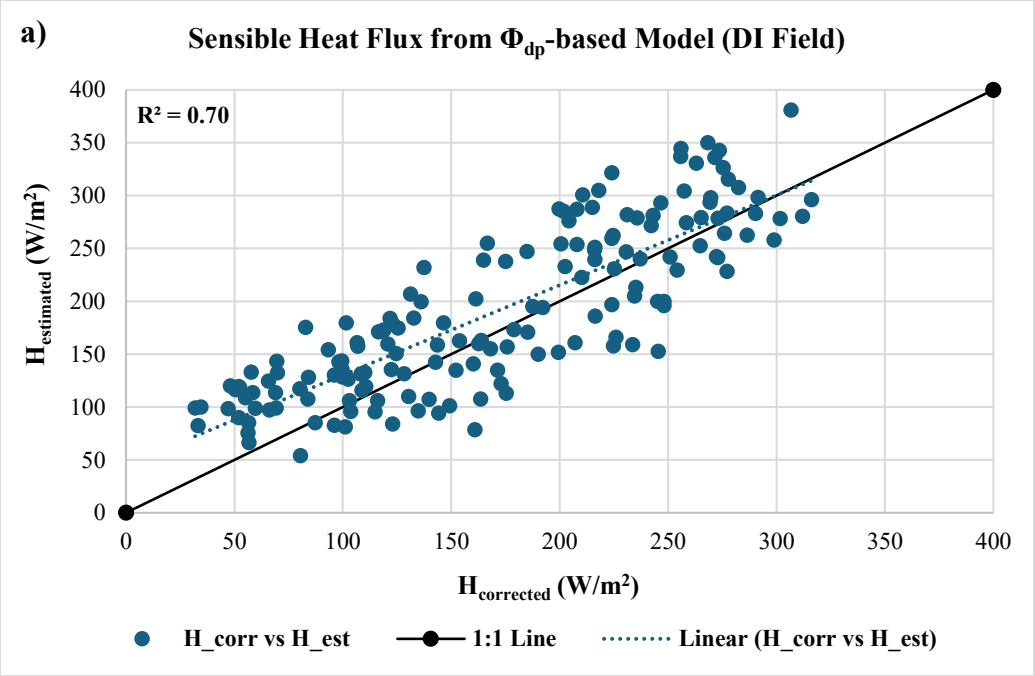
a)
Sensible Heat Flux from Φdp-based Model (DI Field)
R² = 0.70
Hestimated (W/m²)
Hcorrected (W/m²)
0
50
100
150
200
250
300
350
400
H_corr vs H_est
1:1 Line
Linear (H_corr vs H_est)

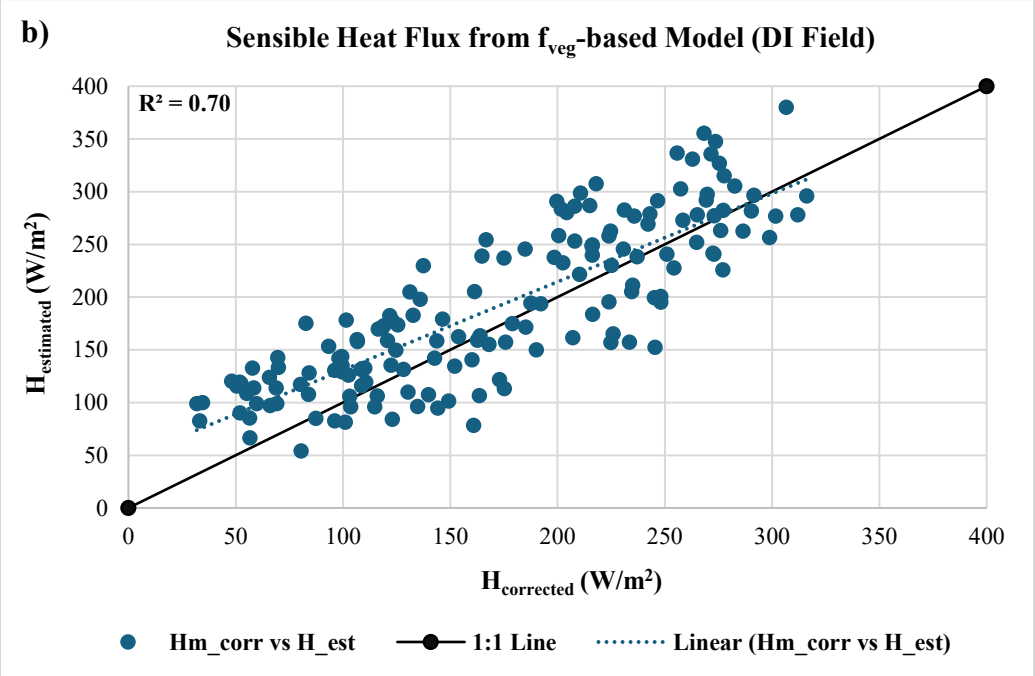
b)
Sensible Heat Flux from fveg-based Model (DI Field)
R² = 0.70
Hestimated (W/m²)
Hcorrected (W/m²)
0
50
100
150
200
250
300
350
400
Hm_corr vs H_est
1:1 Line
Linear (Hm_corr vs H_est)

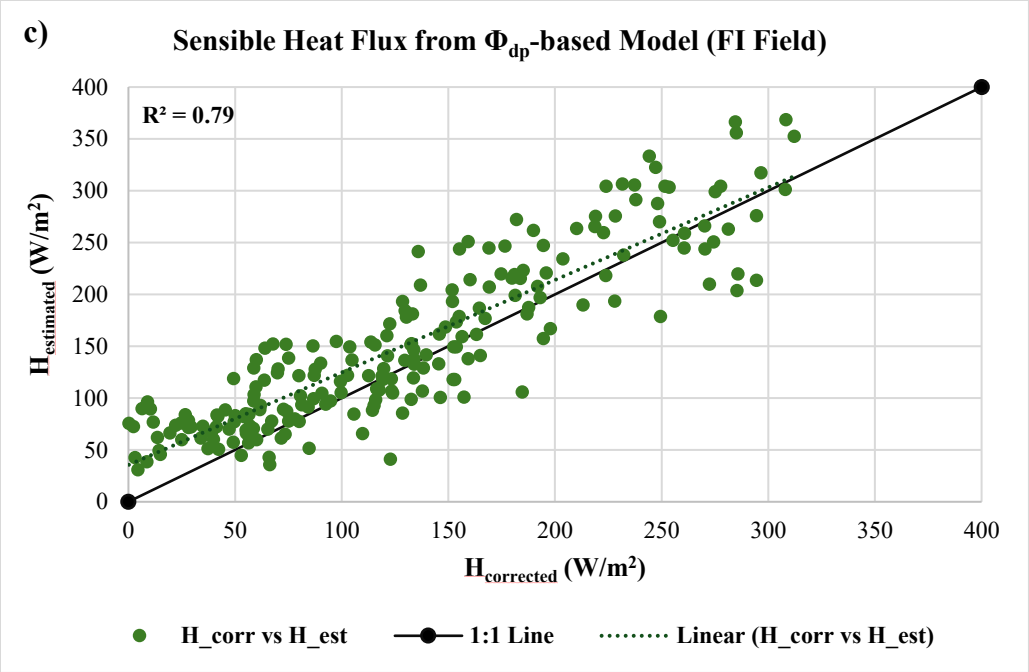

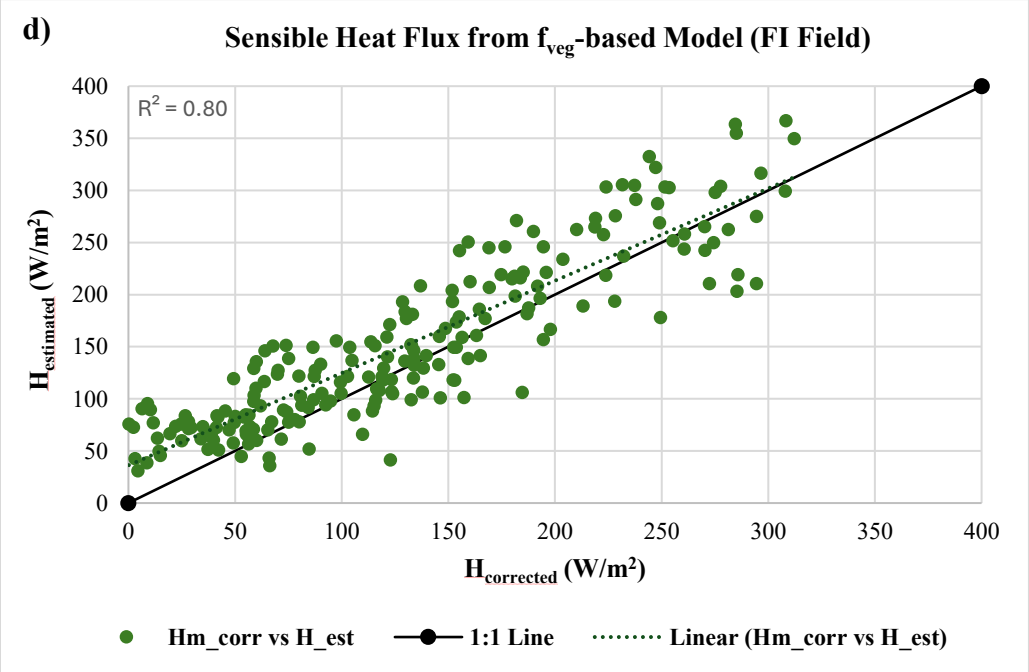

Fig. 4.20. Comparison of measured and modeled sensible heat flux (H) estimated from Φ_{dp}- and f_{veg}-based displacement height (d_o) models under deficit-irrigated (DI) and fully irrigated (FI) conditions. (a) Φ_{dp}-based model for DI field, (b) f_{veg}-based model for DI field, (c) Φ_{dp}-based model for the FI field, and (d) f_{veg}-based model for the FI field. The solid black line represents the 1:1 line, and the dotted line indicates the linear regression fit between measured ($H_{corrected}$) and modeled ($H_{estimated}$) fluxes.

a)

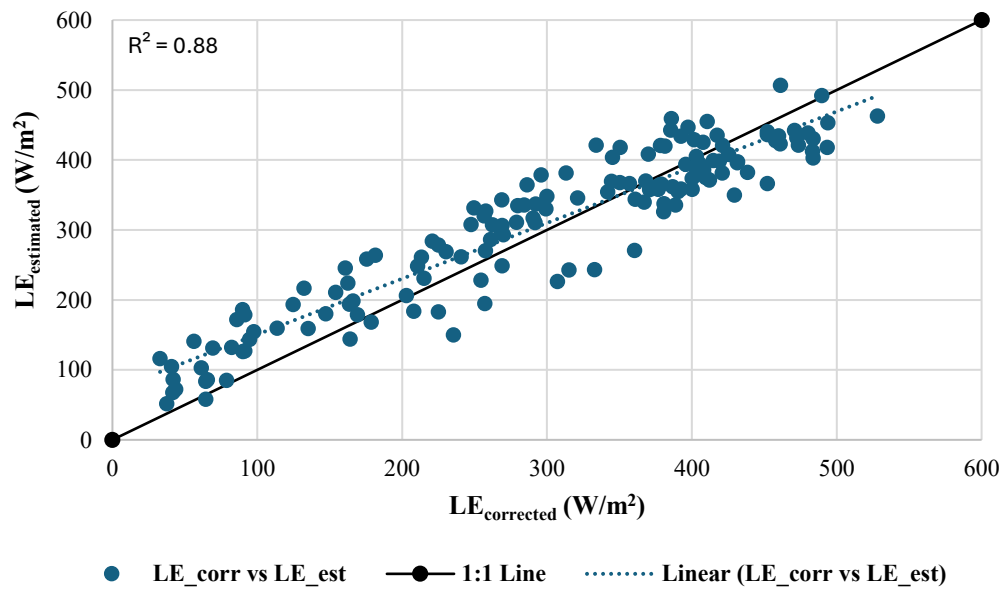
Latent Heat Flux from Φdp-based Model (DI Field)
R² = 0.88
LEestimated (W/m²)
LEcorrected (W/m²)
0
100
200
300
400
500
600
LE_corr vs LE_est
1:1 Line
Linear (LE_corr vs LE_est)

b)

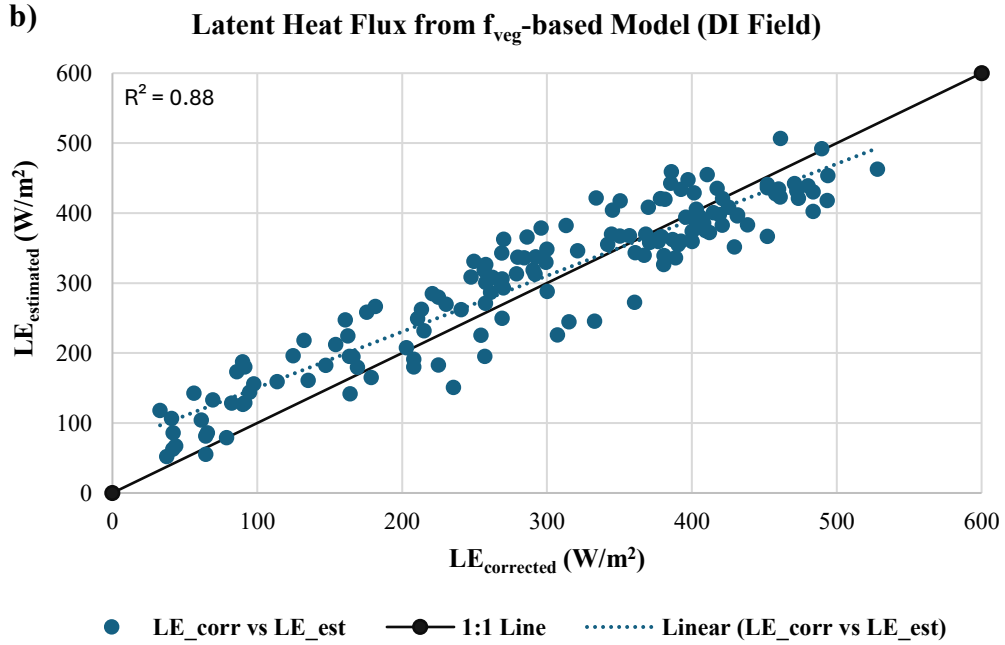
Latent Heat Flux from fveg-based Model (DI Field)
R² = 0.88
LEestimated (W/m²)
LEcorrected (W/m²)
0
100
200
300
400
500
600
LE_corr vs LE_est
1:1 Line
Linear (LE_corr vs LE_est)

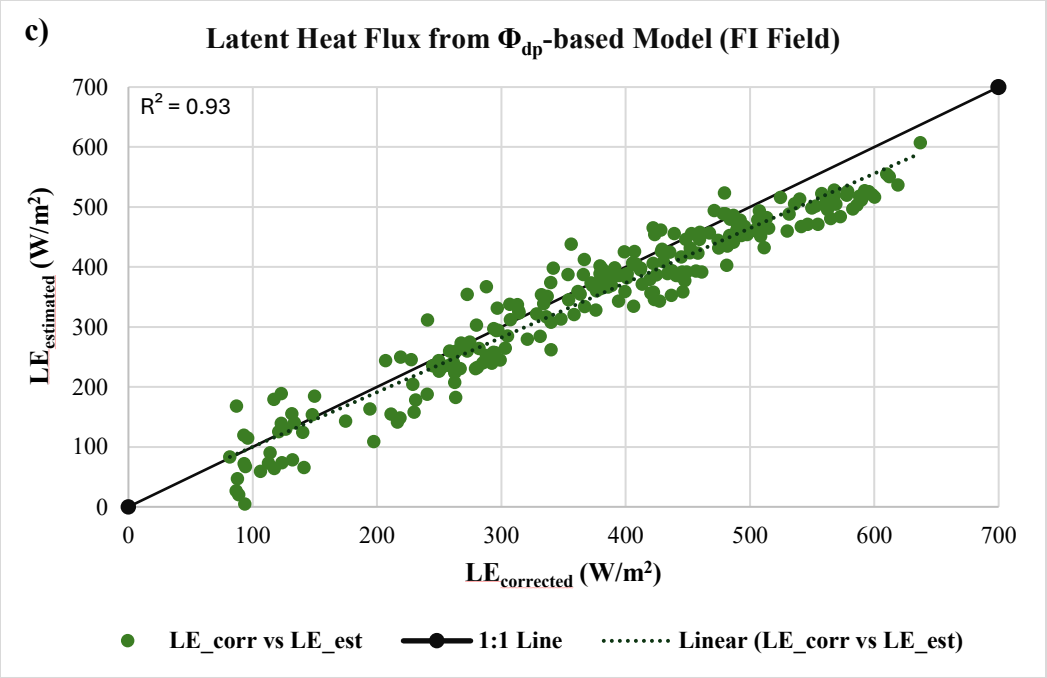

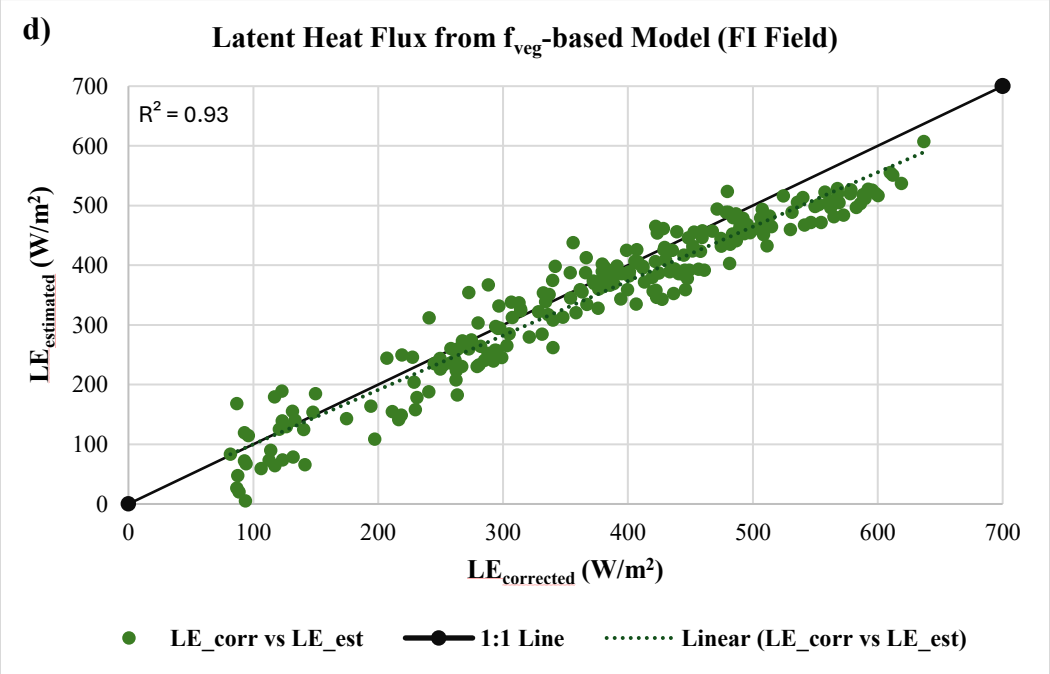

Fig. 4.21. Comparison of measured and modeled latent heat flux (LE) estimated from Φ_{dp}- and f_{veg}-based displacement height models (d_o) under deficit-irrigated (DI) and fully irrigated (FI) conditions. (a) Φ_{dp}-based model for DI field, (b) f_{veg}-based model for DI field, (c) Φ_{dp}-based model for the FI field, and (d) f_{veg}-based model for the FI field. The solid black line represents the 1:1 line, and the dotted line indicates the linear regression fit between measured ($LE_{corrected}$) and modeled ($LE_{estimated}$) fluxes.

4.10.4 Comparative Analysis of New Empirical Dynamic d_o Model and Existing d_o Models for the Estimation of H Heat Fluxes

The H was estimated using the d_o values derived from the three existing empirical models (Pereira et al., 1999; Shaw and Pereira, 1982; Brutsaert, 1982) were evaluated against corrected measured H observations. This evaluation was conducted to assess the relative performance and infer the strengths and limitations of the newly developed empirical dynamic d_o models. Under the FI field, the empirical model of Pereira et al. (1999) achieved the lowest MAE (34.67 W/m^2), while under DI, the f_{veg} model had a slight edge (40.03 W/m^2 vs. 40.71 W/m^2 for Φ_{dp} and 40.77 W/m^2 for Pereira). Brutsaert's d_o model consistently exhibited the highest errors in H estimation, especially in the DI field (e.g., MAE 44.66 W/m^2). RMSE followed a similar pattern: the f_{veg}-based model yielded the smallest RMSE for H flux estimation in both DI (47.05 W/m^2) and FI (42.76 W/m^2) settings, closely trailed by the Φ_{dp} and Pereira models, whereas H estimated from Brutsaert's model yielded the highest RMSE in DI (53.4 W/m^2). These results indicated that the new Φ_{dp} and f_{veg} models performed on par with the best empirical approach in estimating H, with negligible differences (within ~1 W/m^2) in MAE/RMSE across top-performing models.

4.10.5 Seasonal Performance of d_o Models for the Estimation of H Heat Fluxes

The accuracy of H products derived from different d_o models varied across crop growth stages. In June, during early-season development, all models tended to overestimate H, particularly in the FI field, because rapid canopy growth was not well represented by the extrapolated H_c data. In the absence of UAV-based H_c measurements prior to early July, H estimates in the FI field remained positively biased until around July 10, as indicated by higher MBE values. The DI field, in contrast,

had more gradual early-season growth, resulting in smaller early-season errors and fewer extreme outliers in that period. By mid-season (peak vegetative cover in July - August), the H estimates derived from different d_o models exhibited strong consistency with measured and corrected H values, as reflected by notably lower RMSE and MBE. During this stage, both DI and FI fields achieved near-complete canopy closure, which limited soil heat flux and improved the reliability of H estimation by reducing bias. Late in the season (after September), errors grew again as the corn senesced: d_o models tended to overestimate H when the FI field maintained a denser canopy longer, while the DI field's canopy thinned, leading to mismatches in the energy partitioning. In summary, for the H products derived from the d_o models, overestimation was most pronounced at the beginning and end of the growing season (early growth and post-maturity) in the well-watered crop, whereas the deficit-irrigated crop exhibited more consistent performance with smaller deviations during these periods.

4.10.6 Statistical Metrics and Model Robustness for H Estimation

The calculated H results after applying different d_o models yielded moderate to strong agreement with EC-measured corrected half-hourly H fluxes. R^2 values ranged from 0.64 in the worst case, when d_o from Brutsaert's model (DI case) was used, up to 0.79 when the newly proposed vegetation porosity variable (Φ_{dp}, for the FI case) was used for H estimation. These findings indicate a generally higher correlation between measured and estimated H from different d_o models under FI conditions. Efficiency metrics reflected this pattern: NSE scores in the DI field ranged from 0.59 to 0.63 for H estimated from the models, whereas under FI, several d_o-based model-derived H achieved NSE values close to 1.0 (suggesting an excellent fit after removing outliers).

For the DI field, the Φ_{dp}-based d_o model-derived H showed an NSE of 0.62, which was comparable to Pereira's d_0 model-derived H (0.63). The refined index of agreement (d_r) fell within the range of 0.69–0.75 for H estimation for all d_o models, which is considered good agreement. Notably, the highest d_r was observed for H flux estimation from Pereira's d_o model in FI (0.75) and for Shaw and Pereira in DI (0.69). The fact that all d_r values were similar and high suggests that no d_o model-derived H results introduced large errors, and therefore the d_o model performance rankings were not dominated by a few outlier events. The corresponding statistical parameters showing the relationship and bias between measured H and estimated H from the d_o models are summarized in Table 4.3.

4.10.7 Outlier Filtering for Estimated H from Derived d_o Models

To ensure a fair performance evaluation of d_o models, outliers and physically implausible H data were removed prior to analysis as discussed in section 3.8.2. This quality-control step eliminated a similar fraction of data for each d_o model-based estimated H results, with approximately 17% of DI data and 26% of FI data being flagged as outliers. The higher outlier rate for H in the FI field aligns with the early- and late-season overestimation patterns described above. Additionally, the estimated H dataset for the FI field/treatment included a larger number of observations, as both EC1 and EC2 towers recorded heat fluxes for this field, whereas only EC1-based measurements were from the DI field. This dual-tower configuration favored a larger collection of heat fluxes from one field, increased data volume, and contributed to the higher proportion of outliers in the FI dataset. Many of the excluded estimated H from FI corresponded to periods of rapid crop canopy growth and to the crop senesces period, due to a lack of sufficient data during those periods.

For the H dataset estimated for the DI field, some H flux outliers were linked to times when a large portion (~ 25%) of the EC footprint fell outside the research field. Mid-season irrigation events also introduced error as H was occasionally underestimated on and just after irrigation or heavy rainy days (e.g., around DOY 220 - 230 in August), due to inaccurate measurements of heat fluxes for wetting events because of sensor data collection interference. After removing peak H fluxes estimated from the d_o models, the statistical performance metrics showed noticeable improvement.

4.10.8 Comparative Analysis of the New Empirical Dynamic d_o Model and the Existing d_o Models for the Estimation of LE Heat Fluxes

The LE was computed as the residual of the surface EB equation (Eq. 8): $LE = R_n - G - H$. The resulting LE values were compared with the corrected EC-based LE, also derived as a residual of the same energy balance formulation. Because LE was not calculated independently, differences in LE primarily reflect errors in R_n, G, and especially H. Therefore, the results below are reported without attributing LE performance to the proposed d_o formulations.

All five d_o models (Φ_{dp}-based, f_{veg}-based, and the three empirical d_o models) achieved higher predictive skill for LE as a residual, reflecting the stronger biophysical coupling between vegetation parameters and evapotranspiration. MAE values for LE were on the order of 37 - 42 W/m^2 in FI and 35 - 43 W/m^2 in DI, roughly 3 – 5 W/m^2 lower errors than for H, despite the typically larger magnitude of LE fluxes. The Φ_{dp}-based d_o model yielded the lowest RMSE for LE estimation for both fields (48.8 W/m^2 in DI; 44.44 W/m^2 in FI), narrowly outperforming the next best model. In the FI field, the Shaw & Pereira (1982) d_o model produced the smallest MAE (36.55

W/m^2) of all d_o models for estimated LE. In the DI field, errors for these estimated LE were slightly higher and more variable. For instance, Pereira et al.'s d_o model based LE, calculated as residual from EB, the MAE (41.98 W/m^2) was marginally lower than LE that of Φ_{dp}-based d_o model (42.06 W/m^2) and f_{veg} -based d_o model (42.14 W/m^2), while LE from Shaw and Pereira's d_o formulation had the highest MAE (42.99 W/m^2) and RMSE (51.32 W/m^2) in DI. These differences are very small in absolute terms, indicating that for LE, all models clustered near the same performance range. The Φ_{dp}-based d_o model showed a slight overall edge, achieving the highest R^2 (0.93 in FI) for LE, but the f_{veg}-based d_o model and even the traditional approaches were not far behind.

As with H, LE estimation accuracy was generally better for the FI field than for the DI field, although the error range was smaller. The FI field's non-water stress conditions and vigorous crop growth resulted in higher LE fluxes, yielding very high correlation coefficients with the measured LE (R^2 = 0.91 –0.93). Under DI, where LE fluxes were somewhat lower and the crop experienced water stress, R^2 values ranged from ~0.85 to 0.88, which indicated a close relationship between estimated and observed LE values, but lower compared to LE values from the FI field.

Likewise, LE estimates efficiency metrics were higher for the FI field, NSE often approached 1.0, whereas in the DI field case, LE estimates resulted in NSE values in the 0.79 - 0.84 range for the new dynamic d_o models and 0.83 - 0.86 for the empirical ones. The agreement index d_r underscores this pattern: the best agreement was recorded for the FI field (Shaw & Pereira model, $d_r \approx 0.85$), and all d_o models for LE estimation achieved $d_r \geq 0.82$ under FI, whereas in DI d_r values were slightly lower (0.78 - 0.80 for most). In practical terms, all the d_o models resulted in LE in the DI

field very well, but for the FI field case, the LE predictions were even closer to LE measurements. The improved LE performance for the FI case can be attributed to more uniform crop conditions and perhaps the greater magnitude of LE flux, which reduced the relative impact of any fixed sensor or model error. Notably, all LE resulted in a normalized RMSE of 12 - 16% for the FI field data. The corresponding LE estimation evaluation statistical parameters are summarized in Table 4.4.

As with H, model fidelity for LE was generally better in the FI field than in the deficit-treated field, though the gap was minor. The FI field's ample water and vigorous crop growth led to higher LE fluxes and stronger signal-to-noise, yielding very high correlation coefficients (R^2 = 0.91 - 0.93). Under DI, where LE fluxes were somewhat lower and the crop experienced water stress, R^2 values ranged from ~0.85 - 0.88, still indicating a tight relationship between estimated and observed evapotranspiration, but slightly reduced compared to FI.

Likewise, model efficiency metrics were higher for FI: NSE often approached 1.0 for the well-watered field (several models effectively achieved NSE = 1.0 after filtering), whereas in the DI field, NSE values were in the 0.79 - 0.84 range for the new models and 0.83 - 0.86 for the empirical ones. The agreement index d_r underscores this pattern: the best agreement was recorded in the FI field (Shaw & Pereira model, $d_r \approx 0.85$), and all models achieved $d_r \geq 0.82$ under FI, whereas in DI d_r values were slightly lower (0.78 - 0.80 for most). In practical terms, the models predicted latent heat fluxes in the DI field very well, but in the FI field, the predictions were even closer to measurements. The improved performance in the FI case can be attributed to more uniform crop

conditions and perhaps the greater magnitude of LE flux, which reduces the relative impact of any fixed sensor or model error. Notably, all models exhibited better accuracy for LE than for H on the same dataset: for example, normalized RMSE for LE was 12 - 16% in FI compared to 28 - 36% for H. The statistical parameters are summarized in Table 4.4.

Table 4.3: Statistical performance for sensible heat flux (H) estimation, from Φ_{dp}-based and f_{veg} -based displacement height (d_o) models compared with established formulations (Pereira et al., 1999; Shaw and Pereira, 1982; Brutsaert, 1982) under deficit-irrigated (DI) and fully irrigated (FI) conditions. Metrics include MAE, MAD, NSE, RMSE, NMAE, NNSE, NRMSE, coefficient of determination (R^2), and refined index of agreement d_r.

	Unit	**Φ_{dp}-based d_o Model**		**f_{veg}-based d_o Model**		**Pereira et al. (1999) d_o**		**Shaw and Pereira (1982) d_o**		**Brutsaert (1982) d_o**	
Irrigation Type		*DI*	*FI*	*DI*	*FI*	*DI*	*FI*	*DI*	*FI*	*DI*	*FI*
MAE	W/m^2	40.71	35.28	40.03	35.00	40.77	34.67	42.63	37.72	44.07	37.85
MAD	W/m^2	67.11	66.68	65.68	66.36	67.68	68.01	70.71	67.09	71.58	65.84
NSE	-	0.62	0.71	0.61	0.71	0.63	1	0.62	1	0.59	1
RMSE	W/m^2	47.77	43.30	47.05	42.76	48.64	43.48	49.73	47.82	53.40	46.81
NMAE	%	21.41	23.40	21.04	23.24	23.72	26.18	23.91	28.85	24.57	29.40
NNSE	%	0.72	0.77	0.72	0.78	0.73	1	0.73	1	0.71	1
NRMSE	%	25.13	28.71	24.74	28.39	28.29	32.83	27.89	36.57	29.77	36.36
R^2	-	0.70	0.79	0.70	0.80	0.66	0.76	0.66	0.74	0.64	0.74
d_r	-	0.70	0.74	0.69	0.74	0.69	0.75	0.69	0.71	0.69	0.71

Table 4.4: Statistical performance of latent heat flux (LE) estimation, from Φ_{dp}-based and f_{veg} -based displacement height models compared with established formulations (Pereira et al., 1999; Shaw and Pereira, 1982; Brutsaert, 1982) under deficit-irrigated (DI) and fully irrigated (FI) conditions. Metrics include MAE, MAD, NSE, RMSE, NMAE, NNSE, NRMSE, coefficient of determination (R^2), and refined index of agreement d_r.

	Unit	**Φ_{dp}-based d_o Model**		**f_{veg}-based d_o Model**		**Pereira et al. (1999) d_o**		**Shaw and Pereira (1982) d_o**		**Brutsaert (1982) d_o**	
Irrigation Type		*DI*	*FI*	*DI*	*FI*	*DI*	*FI*	*DI*	*FI*	*DI*	*FI*
MAE	W/m^2	42.06	36.85	42.14	37.20	41.98	39.41	42.99	36.55	42.27	42.28
MAD	W/m^2	96.53	108.4	95.40	109.6	100.7	122.8	101.1	125.1	101.2	119.2
NSE	-	0.81	0.89	0.79	0.89	0.88	1	0.83	1	0.83	1
RMSE	W/m^2	48.80	44.44	49.02	45.08	49.94	48.64	51.32	45.47	50.30	51.94
NMAE	%	13.77	10.64	13.89	10.80	13.56	10.71	14.02	9.96	13.82	11.26
NNSE	%	0.84	0.89	0.84	0.89	0.86	1	0.85	1	0.86	1
NRMSE	%	15.98	12.83	16.16	13.09	16.13	13.21	16.73	12.39	16.45	13.83
R^2	-	0.88	0.93	0.88	0.93	0.86	0.91	0.85	0.92	0.86	0.91
d_r	-	0.78	0.83	0.78	0.83	0.79	0.84	0.79	0.85	0.75	0.82

4.10.9. The New Empirical Dynamic d_o Models Improvement Evaluation

The comparison of statistical measures between the Φ_{dp}-based and f_{veg}-based d_o models and existing d_o models showed an improvement. The Φ_{dp}-based d_o model reduced NRMSE in estimated H results by up to 15.6% for DI and 21.1% for FI, while the f_{veg}-based d_o model achieved reductions of 16.9% (DI) and 21.9% (FI) from the existing empirical d_o models. Similarly, in terms of d_r, the Φ_{dp}-based d_o model improved by 0.7% for DI and 3.08% for FI, whereas the f_{veg}-based d_o model showed improvements of 0.4% (DI) and 3.2% (FI) for H estimation. Lastly, for R^2, the Φ_{dp}-based d_o model increased by 9.8% for DI and 7.17% for FI, while the f_{veg}-based d_o model improved by 9.8% (DI) and 8.3% (FI). Overall, both Φ_{dp}- and f_{veg}-based d_o models outperformed existing models, providing more accurate H estimations under varying field conditions.

Uncertainty analysis showed that errors in R_n (±6 %) and G (±15 %), reported by Twine et al. (2000) and Van Loon et al. (1998), combine to yield roughly ±10 % uncertainty in R_n - G. The EC system generally under-measures turbulent fluxes by 10–30 %, giving an overall 20–35 % uncertainty in uncorrected H and LE. After applying energy-balance closure through the BR method, which introduces an additional ± 5–10 % uncertainty in flux partitioning, the corrected fluxes exhibit an overall uncertainty of about ±10–15 % relative to the available energy. Because u_* used in the neutral formulation of d_o is derived from the same EC data, this bias propagates into the d_o estimation, resulting in an approximate 17–25 % uncertainty in d_o.

CHAPTER 5: DISCUSSION, CONCLUSIONS, and RECOMMENDATIONS

5.1 Discussion

This study developed and evaluated two dynamic zero-plane displacement height (d_o) models using remote sensing and field data from two irrigated maize fields. The developed dynamic d_o models were calibrated as a function of newly proposed dynamic canopy porosity (Φ_{dp}), fractional vegetation cover (f_{veg}), and thermal and aerodynamic surface properties. The effect of d_o models developed and three commonly used d_o models on the estimation of H and LE heat fluxes were evaluated with fluxes derived from two eddy covariance (EC) stations. Results confirm the central hypothesis that incorporating dynamic biophysical and aerodynamic variables into the 'd_o' estimates improve corn sensible (H) and latent (LE) heat fluxes estimation.

Across both corn irrigation regimes, the new 'd_o' models translated into strong H and LE performances ($R^2 \approx 0.70$ - 0.80 for H and 0.88 - 0.93 for LE, and MAE 37 - 44 W/m² for H). These resulting heat flux estimation accuracies were comparable to or better than the best traditional LAI-based 'd_o' formulations for heterogeneous crop canopies subjected to different irrigation treatments. The Φ_{dp} and f_{veg}-based 'd_o' models captured canopy–atmosphere interactions by integrating canopy structure, wind direction, and surface–air temperature gradients, variables that conventional static 'd_o' models do not include. This dynamic representation of d_o yielded more realistic heat fluxes, partitioning, and reduced systematic bias in H and LE, especially under heterogeneous or stressed canopy conditions.

Comparatively, Brutsaert's crop height-only dependent 'd_o' model introduced larger errors in heat flux estimates due to its inability to represent canopy density and dynamic wind penetration effects.

Pereira's and Shaw & Pereira's LAI-based d_o approaches improved heat fluxes estimation performance but were insensitive to temporal and directional canopy dynamics. In contrast, the Φ_{dp} and f_{veg} -based 'd_o' formulations dynamically adjusted to changing canopy structure under corresponding weighted heat flux footprint areas, achieving better heat flux estimations. However, the new 'd_o' models were calculated by taking weighted heat flux footprint areas, assuming a rectangular footprint area, which is not the actual footprint area. This assumption was made to simplify the process and may have introduced some errors.

The overall estimation of the energy budget H and LE components improved through the refined d_o estimation. Corrected EC-based heat fluxes resulted in "H + LE", being close to the available energy "R_n - G" across both irrigation strategies. The integration of the pseudo-surface temperature model (PSTM) and UAS-derived crop height model (CHM) successfully captured field-scale heterogeneity, linking multispectral thermal data with aerodynamic parameters.

5.2. Conclusions

This research demonstrates that incorporating dynamic canopy and surface aerodynamic descriptors into 'd_o' modeling substantially improves sensible heat fluxes estimation accuracy. The Φ_{dp}- and f_{veg}-based 'd_o' models captured spatial and temporal variations in crop structure and microclimate, performing better than static 'd_o' approaches. The consistent performance of d_o under both DI and FI regimes validates the hypothesis that integrating biophysical and directional variables strengthens the reliability of remotely sensed evapotranspiration models.

Key findings include:

- Dynamic d_o parameterization reduced H and LE estimation errors by up to 20% relative to fixed-height models.

- H estimation accuracy peaked during mid-season, confirming the role of canopy stability in flux predictability.

- Improved d_o estimation enhanced energy balance closure, reducing the residual between (H + LE) and (R_n - G).

- Both the Φ_{dp}-based and f_{veg}-based 'd_o' models proved adaptable to irrigation strategies, maintaining accuracy across heterogeneous field conditions.

5.3 Recommendations

- *Enhancing Early-Season Canopy Data Acquisition*

  Deploying UAS surveys immediately after emergence to capture bare soil conditions (reference level) and early crop height and density dynamics. Integrating crop growth models or phenological predictors can bridge temporal gaps and mitigate early-season heat flux biases.

- *Calibrating Models Across Crops and Climates*

  Calibrate the Φ_{dp}- and f_{veg}-based 'd_o' models to different crops (e.g., wheat, soybean, orchards, etc.) and environments to test their transferability. Multi-year data inclusion in 'd_o' calibration will establish model robustness for regional evapotranspiration monitoring.

- *Incorporating Three-Dimensional Canopy and Wind Effects*

  Future studies should integrate 3D canopy metrics (e.g., clumping index, gap fraction) and advanced wind–canopy interaction modeling to further enhance aerodynamic realism and support precision irrigation systems.

In summary, the study developed a calibration framework for the estimation of dynamic zero-plane displacement heights using remote sensing and field-based data. By coupling surface temperature and canopy structural heterogeneity with aerodynamic processes, it contributes to more accurate heat flux estimation, better energy balance closure, and improved water management in irrigated cropping systems.

REFERENCES

A. Irmak, R. K. Singh, E. A. Walter-Shea, S. B. Verma, & A. E. Suyker. (2011). Comparison and Analysis of Empirical Equations for Soil Heat Flux for Different Cropping Systems and Irrigation Methods. *Transactions of the ASABE*, *54*(1), 67–80. https://doi.org/10.13031/2013.36261

Al-Majali, Z., & Chávez, J. L. (2024). Assessing Remote Sensing-Based Maize Crop Biophysical Characteristics and Evapotranspiration Estimations. *Journal of Agricultural Science*, *16*(10), 11. https://doi.org/10.5539/jas.v16n10p11

Anderson, M., Neale, C., Li, F., Norman, J., Kustas, W., Jayanthi, H., & Chavez, J. (2004). Upscaling ground observations of vegetation water content, canopy height, and leaf area index during SMEX02 using aircraft and Landsat imagery. *Remote Sensing of Environment*, *92*(4), 447–464. https://doi.org/10.1016/j.rse.2004.03.019

Arslan, İ., Topakcı, M., & Demir, N. (2022). Monitoring Maize Growth and Calculating Plant Heights with Synthetic Aperture Radar (SAR) and Optical Satellite Images. *Agriculture*, *12*(6), 800. https://doi.org/10.3390/agriculture12060800

Aubinet, M., Vesala, T., & Papale, D. (Eds.). (2012). *Eddy Covariance: A Practical Guide to Measurement and Data Analysis*. Springer Netherlands. https://doi.org/10.1007/978-94-007-2351-1

Bastiaanssen, W. G. M., Pelgrum, H., Wang, J., Ma, Y., Moreno, J. F., & Roerink, G. J. (n.d.). *A remote sensing surface energy balance algorithm for land (SEBAL) 2. Validation*.

Brest, C. L., & Goward, S. N. (1987). Deriving surface albedo measurements from narrow band satellite data. *International Journal of Remote Sensing*, *8*(3), 351–367. https://doi.org/10.1080/01431168708948646

Brunsell, N. A., & Gillies, R. R. (n.d.). *Incorporating Surface Emissivity into a Thermal Atmospheric Correction*.

Brutsaert, W. (1982). *Evaporation into the Atmosphere*. Springer Netherlands. https://doi.org/10.1007/978-94-017-1497-6

Chávez, JoséL., Neale, C. M. U., Hipps, L. E., Prueger, J. H., & Kustas, W. P. (2005). Comparing Aircraft-Based Remotely Sensed Energy Balance Fluxes with Eddy Covariance Tower Data Using Heat Flux Source Area Functions. *Journal of Hydrometeorology*, *6*(6), 923–940. https://doi.org/10.1175/JHM467.1

Chávez, J. L., Neale, C. M., Prueger, J. H., & Kustas, W. P. (2008). Daily evapotranspiration estimates from extrapolating instantaneous airborne remote sensing ET values. *Irrigation Science*, *27*(1), 67-81.

Colaizzi, P. D., Evett, S. R., Howell, T. A., & Tolk, J. A. (2004). *Comparison of aerodynamic and radiometric surface temperature using precision weighing lysimeters* (W. Gao & D. R. Shaw, Eds.; p. 215). https://doi.org/10.1117/12.559503

Costa-Filho, E., Chávez, J. L., Zhang, H., & Andales, A. A. (2021). An optimized surface aerodynamic temperature approach to estimate maize sensible heat flux and evapotranspiration. *Agricultural and Forest Meteorology*, *311*, 108683. https://doi.org/10.1016/j.agrformet.2021.108683

Dettinger, M., Udall, B., & Georgakakos, A. (2015). Western water and climate change. *Ecological Applications*, *25*(8), 2069-2093.

Dong, Z., Gao, S., & Fryrear, D. W. (2001). Drag coefficients, roughness length and zero-plane displacement height as disturbed by artificial standing vegetation. *Journal of Arid Environments*, *49*(3), 485-505.

Engelbert, E. A., & Scheuring, A. F. (Eds.). (2023). *Water scarcity: Impacts on western agriculture*. Univ of California Press.

Evans, R. G., & Sadler, E. J. (2008). Methods and technologies to improve efficiency of water use. *Water resources research*, *44*(7).

Ferreira, A. G., Soria-Olivas, E., López, A. J. S., & Lopez-Baeza, E. (2011). Estimating net radiation at surface using artificial neural networks: a new approach. *Theoretical and applied climatology*, *106*(1), 263-279.

Foken, T., Leuning, R., Oncley, S. P., Mauder, M., & Aubinet, M. (2012). Corrections and data quality control. In M. Aubinet, T. Vesala, & D. Papale (Eds.), *Eddy covariance: A practical guide to measurement and data analysis* (pp. 85–131). Dordrecht: Springer. https://doi.org/10.1007/978-94-007-2351-1_4

Grassini, P., Yang, H., Irmak, S., Thorburn, J., Burr, C., & Cassman, K. G. (2011). High-yield irrigated maize in the Western US Corn Belt: II. Irrigation management and crop water productivity. *Field crops research*, *120*(1), 133-141.

Heidbach, K., Schmid, H. P., & Mauder, M. (2017). Experimental evaluation of flux footprint models. *Agricultural and Forest Meteorology*, *246*, 142–153. https://doi.org/10.1016/j.agrformet.2017.06.008

Irmak, S., Mutiibwa, D., Irmak, A., Arkebauer, T. J., Weiss, A., Martin, D. L., & Eisenhauer, D. E. (2008). On the scaling up leaf stomatal resistance to canopy resistance using photosynthetic photon flux density. *Agricultural and Forest Meteorology*, *148*(6-7), 1034-1044.

Jackson, R. D., Pinter Jr, P. J., & Reginato, R. J. (1985). Net radiation calculated from remote multispectral and ground station meteorological data. *Agricultural and forest Meteorology*, *35*(1-4), 153-164.

Karthikeyan, L., Chawla, I., & Mishra, A. K. (2020). A review of remote sensing applications in agriculture for food security: Crop growth and yield, irrigation, and crop losses. *Journal of Hydrology*, *586*, 124905.

Kasampalis, D. A., Alexandridis, T. K., Deva, C., Challinor, A., Moshou, D., & Zalidis, G. (2018). Contribution of remote sensing on crop models: a review. *Journal of Imaging*, *4*(4), 52.

Lloyd, C. R., Bessemoulin, P., Cropley, F. D., Culf, A. D., Dolman, A. J., Elbers, J., ... & Verhoef, A. (1997). A comparison of surface fluxes at the HAPEX-Sahel fallow bush sites. *Journal of Hydrology*, *188*, 400-425.

Mahrt, L., & Vickers, D. (2004). Bulk formulation of the surface heat flux. *Boundary-Layer Meteorology*, *110*(3), 357-379.

Maimaitijiang, M., Sagan, V., Sidike, P., Maimaitiyiming, M., Hartling, S., Peterson, K. T., ... & Fritschi, F. B. (2019). Vegetation index weighted canopy volume model (CVMVI) for soybean biomass estimation from unmanned aerial system-based RGB imagery. *ISPRS journal of photogrammetry and remote sensing*, *151*, 27-41.

Meiyan, S., Mengyuan, S., Qizhou, D., Xiaohong, Y., Baoguo, L., & Yuntao, M. (2022). Estimating the maize above-ground biomass by constructing the tridimensional concept model based on UAV-based digital and multi-spectral images. *Field Crops Research*, *282*, 108491. https://doi.org/10.1016/j.fcr.2022.108491

Mohan, S. V., Nikhil, G. N., Chiranjeevi, P., Reddy, C. N., Rohit, M. V., Kumar, A. N., & Sarkar, O. (2016). Waste biorefinery models towards sustainable circular bioeconomy: critical review and future perspectives. *Bioresource technology*, *215*, 2-12.

Molion, L. C. B., & Moore, C. J. (1983). Estimating the zero-plane displacement for tall vegetation using a mass conservation method. *Boundary-Layer Meteorology*, *26*(2), 115-125.

Ning, T., Feng, Q., Li, R., & Yang, L. (2022). Interaction between wind speed and net radiation controls reference evapotranspiration variance in the inland river basin of Northwest China. *Hydrological Processes*, *36*(6), e14620.

Pereira, L. S., Perrier, A., Allen, R. G., & Alves, I. (1999a). Evapotranspiration: Concepts and Future Trends. *Journal of Irrigation and Drainage Engineering*, *125*(2), 45–51. https://doi.org/10.1061/(asce)0733-9437(1999)125:2(45)

Pereira, L. S., Perrier, A., Allen, R. G., & Alves, I. (1999b). Evapotranspiration: Concepts and Future Trends. *Journal of Irrigation and Drainage Engineering*, *125*(2), 45–51. https://doi.org/10.1061/(ASCE)0733-9437(1999)125:2(45)

Peters, R. T., & Evett, S. R. (2008). Automation of a Center Pivot Using the Temperature-Time-Threshold Method of Irrigation Scheduling. *Journal of Irrigation and Drainage Engineering*, *134*(3), 286–291. https://doi.org/10.1061/(ASCE)0733-9437(2008)134:3(286)

Picard, A., Davis, R. S., Gläser, M., & Fujii, K. (2008). Revised formula for the density of moist air (CIPM-2007). *Metrologia*, *45*(2), 149–155. https://doi.org/10.1088/0026-1394/45/2/004

Raupach, M. R. (1994). Simplified expressions for vegetation roughness length and zero-plane displacement as functions of canopy height and area index. *Boundary-layer meteorology*, *71*(1), 211-216.

Sharma, B., Molden, D., & Cook, S. (2015). Water use efficiency in agriculture: Measurement, current situation and trends.

Schaudt, K. J., & Dickinson, R. E. (2000). An approach to deriving roughness length and zero-plane displacement height from satellite data, prototyped with BOREAS data. *Agricultural and Forest Meteorology*, *104*(2), 143-155.

Shanmugapriya, P., Rathika, S., Ramesh, T., & Janaki, P. (2019). Applications of remote sensing in agriculture-A Review. *Int. J. Curr. Microbiol. Appl. Sci*, *8*(01), 2270-2283.

Shaw, R. H., & Pereira, A. R. (1982). Aerodynamic roughness of a plant canopy: A numerical experiment. *Agricultural Meteorology*, *26*(1), 51–65. https://doi.org/10.1016/0002-1571(82)90057-7

Singh, R. K., Irmak, A., Irmak, S., & Martin, D. L. (2008). Application of SEBAL Model for Mapping Evapotranspiration and Estimating Surface Energy Fluxes in South-Central Nebraska. *Journal of Irrigation and Drainage Engineering*, *134*(3), 273–285. https://doi.org/10.1061/(ASCE)0733-9437(2008)134:3(273)

Technical Committee on Standardization of Reference Evapotranspiration. (2005). *The ASCE Standardized Reference Evapotranspiration Equation* (R. G. Allen, I. A. Walter, R. L. Elliott, T. A. Howell, D. Itenfisu, M. E. Jensen, & R. L. Snyder, Eds.). American Society of Civil Engineers. https://doi.org/10.1061/9780784408056

Twine, T. E., Kustas, W. P., Norman, J. M., Cook, D. R., Houser, P. R., Meyers, T. P., Prueger, J. H., Starks, P. J., & Wesely, M. L. (2000). Correcting eddy-covariance flux underestimates over a grassland. *Agricultural and Forest Meteorology*, *103*(3), 279–300. https://doi.org/10.1016/S0168-1923(00)00123-4

Van Loon, W. K. P., Bastings, H. M. H., & Moors, E. J. (1998). Calibration of soil heat flux sensors. *Agricultural and Forest Meteorology*, *92*(1), 1-8.

Vickers, D., & Mahrt, L. (1997). Quality Control and Flux Sampling Problems for Tower and Aircraft Data. *Journal of Atmospheric and Oceanic Technology*, *14*(3), 512–526. https://doi.org/10.1175/1520-0426(1997)014%253C0512:QCAFSP%253E2.0.CO;2

Willmott, C. J. (1981). ON THE VALIDATION OF MODELS. *Physical Geography*, *2*(2), 184–194. https://doi.org/10.1080/02723646.1981.10642213

Willmott, C. J., Robeson, S. M., & Matsuura, K. (2012). A refined index of model performance. *International Journal of Climatology*, *32*(13), 2088–2094. https://doi.org/10.1002/joc.2419

Xie, Y., Xu, J., Pu, Y., Huang, L., Zhang, M., Xiao, W., & Lee, X. (2025). Estimation of Sensible and Latent Heat Fluxes from Different Ecosystems Using the Daily-Scale Flux Variance Method. *Atmosphere*, *16*(9), 1030.

APPENDICES

Appendix A: Equations for the Parameters Required to Calculate the Corrected IRT

NDVI was calculated for the PlanetScope Imagery as:

$$NDVI = \frac{NIR - Red}{NIR + Red} \quad \text{(A1)}$$

Next, the scaled NDVI (N*) was then calculated for the station points as:

$$N^* = \frac{NDVI - NDVI_0}{NDVI_{max} - NDVI_0} \quad \text{(A2)}$$

where $NDVI_0 = 0.15$ represents bare soil; $NDVI_{max} = 0.9$ represents healthy vegetation.

Fractional vegetation cover (f_c) was calculated for the station points as:

$$f_c = (N^*)^2 \quad \text{(A3)}$$

and surface thermal emissivity (dimensionless) was calculated for the station points as:

$$\varepsilon_s = (f_c \times 0.98) + [(1 - f_c) \times 0.93] \quad \text{(A4)}$$

where 0.98 is the emissivity of healthy green vegetation and 0.93 is the emissivity of bare soil.

Appendix B: Equations for the Parameters Required to Calculate the R_n

Albedo was derived from PlanetScope red and NIR SR values using the method applied by Chávez et al. (2005) as:

$$\alpha = (0.512 \times \text{Red}) + (0.418 \times \text{NIR}) \quad \text{(A5)}$$

ε_s was estimated by calculating NDVI-based f_c, using equation A3, applied across the entire raster image of the field, following Brest & Goward (1987).

For SAT tower-based data, T_a and RH measured at 10 m height from two SAT towers were averaged to represent field-scale conditions. Air saturation vapor pressure (e_s) was calculated as:

$$e_s = 0.6108 \times \exp^{\left(\frac{17.2 \times T_a}{T_a + 237.3}\right)} \quad \text{(A6)}$$

where T_a is in °C; e_s is in kPa.

Actual vapor pressure (e_a) was then obtained as:

$$e_a = \frac{RH_{mean}}{100} \times e_s \quad \text{(A7)}$$

where RH is in %; e_a is in kPa, as e_s is in kPa as well.

Thermal atmospheric emissivity (ε_a) was computed using Brutsaert (1975):

$$\varepsilon_a = 1.24 \times \left(\frac{e_a}{T_a}\right)^{\frac{1}{7}} \quad \text{(A8)}$$

where e_a is in mb, T_a is in K.

Appendix C: Equations for the Parameters Required to Calculate Corrected H and LE

The EBC correction was applied according to the following relationship:

$$R_n = H + LE + G + \Delta \quad \text{(A9)}$$

where Δ is the residual, which needs to be balanced for closure by proportionally distributing it between H and LE while maintaining the Bowen ratio (β) as follows:

$$\beta = \frac{H}{LE} = \frac{\Delta H}{\Delta LE} \quad \text{(A10)}$$

$$\Delta = \Delta H + \Delta LE \quad \text{(A11)}$$

Then the adjustment term for H is:

$$\Delta H = \beta \times LE \quad \text{(A12)}$$

From the EBC equation, the Δ becomes:

$$\Delta = R_n - H + LE + G \text{……..……..(A13)}$$

Substituting $\Delta H = \beta \times LE$ in the EB equation, the adjustment term for LE becomes:

$$\Delta LE = \frac{R_n - G - [(1+\beta) \times LE]}{(1+\beta)} \text{……..…..(A14)}$$

Appendix D: **Fig. A1. Raw PlanetScope band reflectance values (RGB, and NIR) within 5 m radius buffer areas around MSR stations and during the 2024 growing season. The time-series plots show high-frequency fluctuations and irregular spikes caused by atmospheric scattering, illumination variation, and sensor noise, illustrating the need for polynomial smoothing in subsequent analyses**

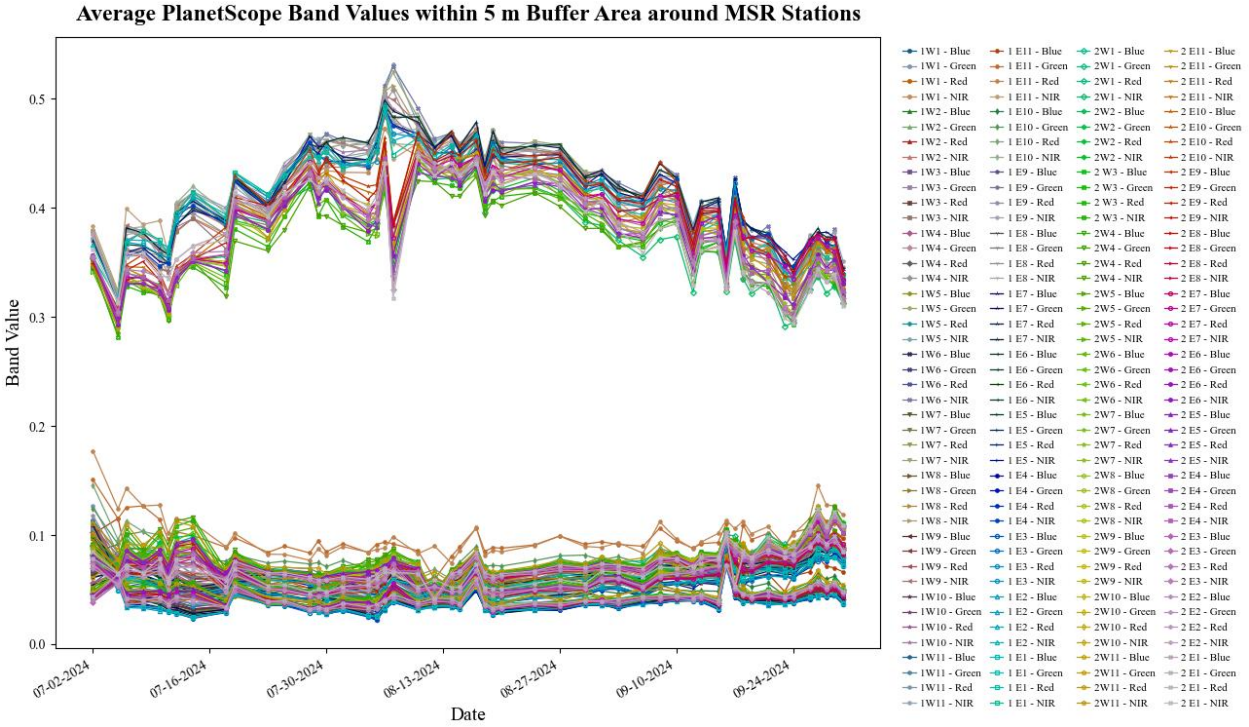

Appendix E: **Fig. A2-A45. Polynomial regression fits for PlanetScope raw reflectance data (red, green, blue, and NIR bands) across selected field stations (ST 1.1, ST 1.2, ST 2.1, ST 2.2, MSR 1 W1 – 1 W11, MSR 2 E1 – 2 E11, and MSR 2 W1 – 2W11). Each subfigure shows observed band values and fitted polynomial curves (degree 3 or 5) representing seasonal reflectance trends (DOY 160–290). All models achieved strong goodness of fit ($R^2 > 0.80$), illustrating consistent canopy spectral dynamics across the growing season under varying field conditions.**

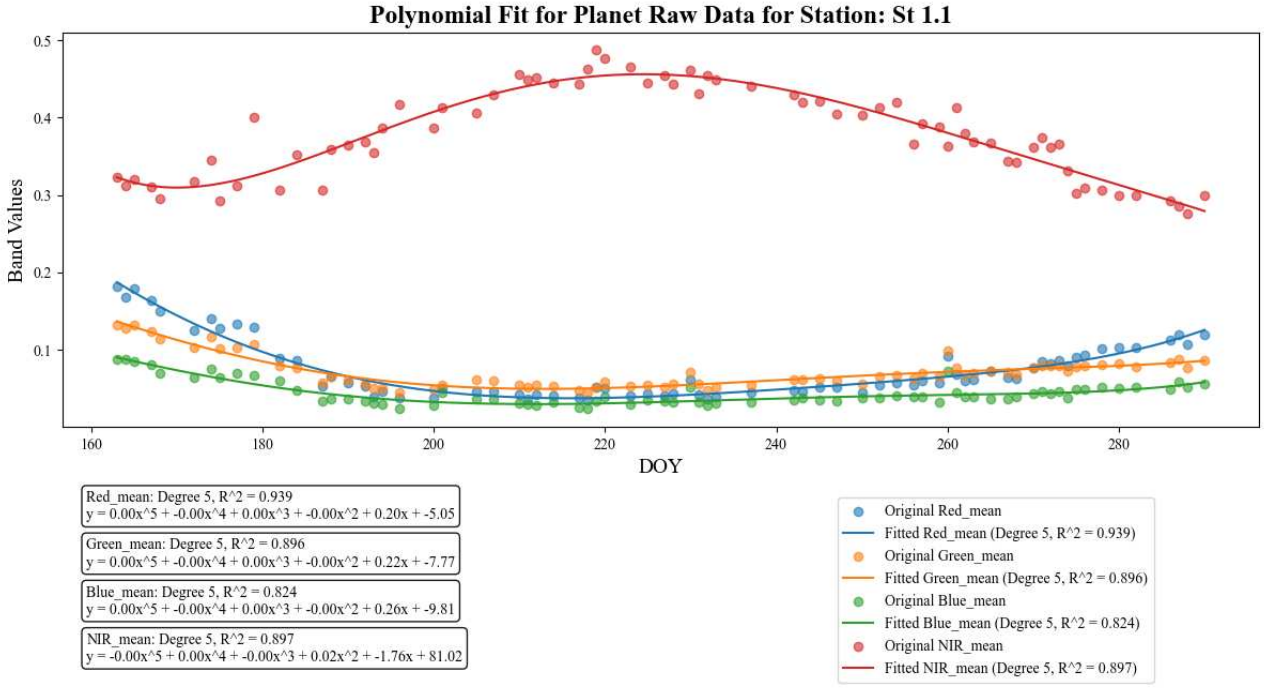

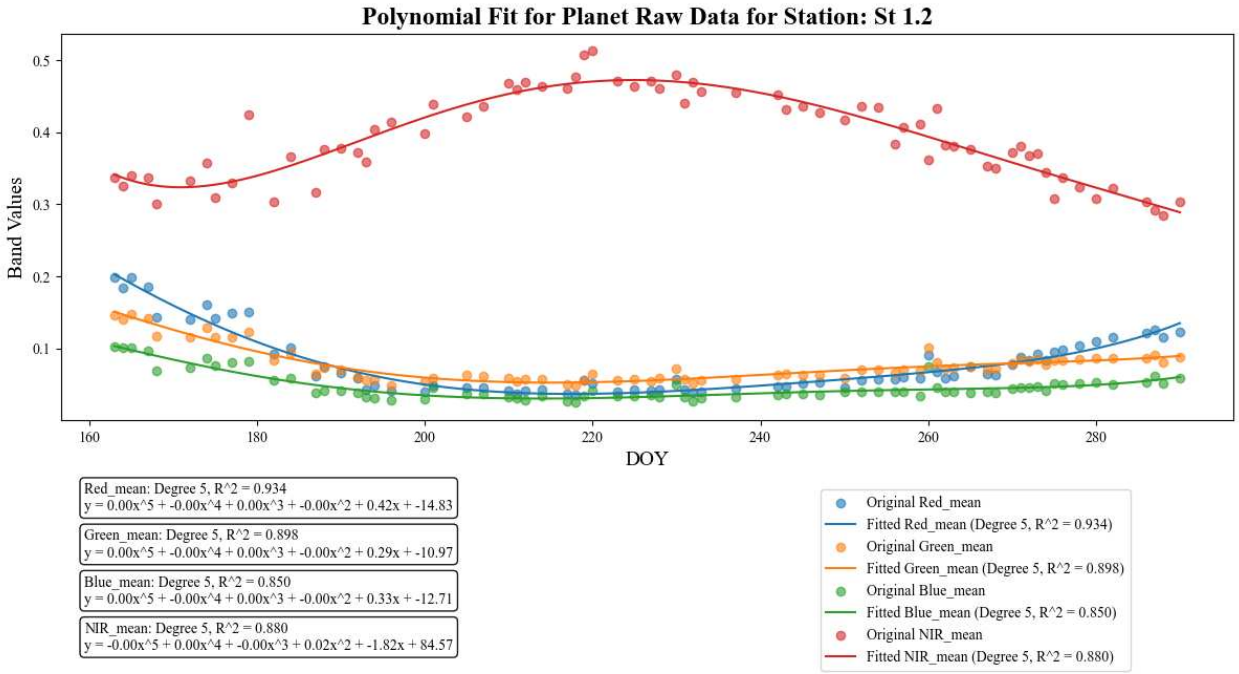
Polynomial Fit for Planet Raw Data for Station: St 1.2
Band Values
DOY
Red_mean: Degree 5, R^2 = 0.934
y = 0.00x^5 + -0.00x^4 + 0.00x^3 + -0.00x^2 + 0.42x + -14.83
Green_mean: Degree 5, R^2 = 0.898
y = 0.00x^5 + -0.00x^4 + 0.00x^3 + -0.00x^2 + 0.29x + -10.97
Blue_mean: Degree 5, R^2 = 0.850
y = 0.00x^5 + -0.00x^4 + 0.00x^3 + -0.00x^2 + 0.33x + -12.71
NIR_mean: Degree 5, R^2 = 0.880
y = -0.00x^5 + 0.00x^4 + -0.00x^3 + 0.02x^2 + -1.82x + 84.57
Original Red_mean
Fitted Red_mean (Degree 5, R^2 = 0.934)
Original Green_mean
Fitted Green_mean (Degree 5, R^2 = 0.898)
Original Blue_mean
Fitted Blue_mean (Degree 5, R^2 = 0.850)
Original NIR_mean
Fitted NIR_mean (Degree 5, R^2 = 0.880)

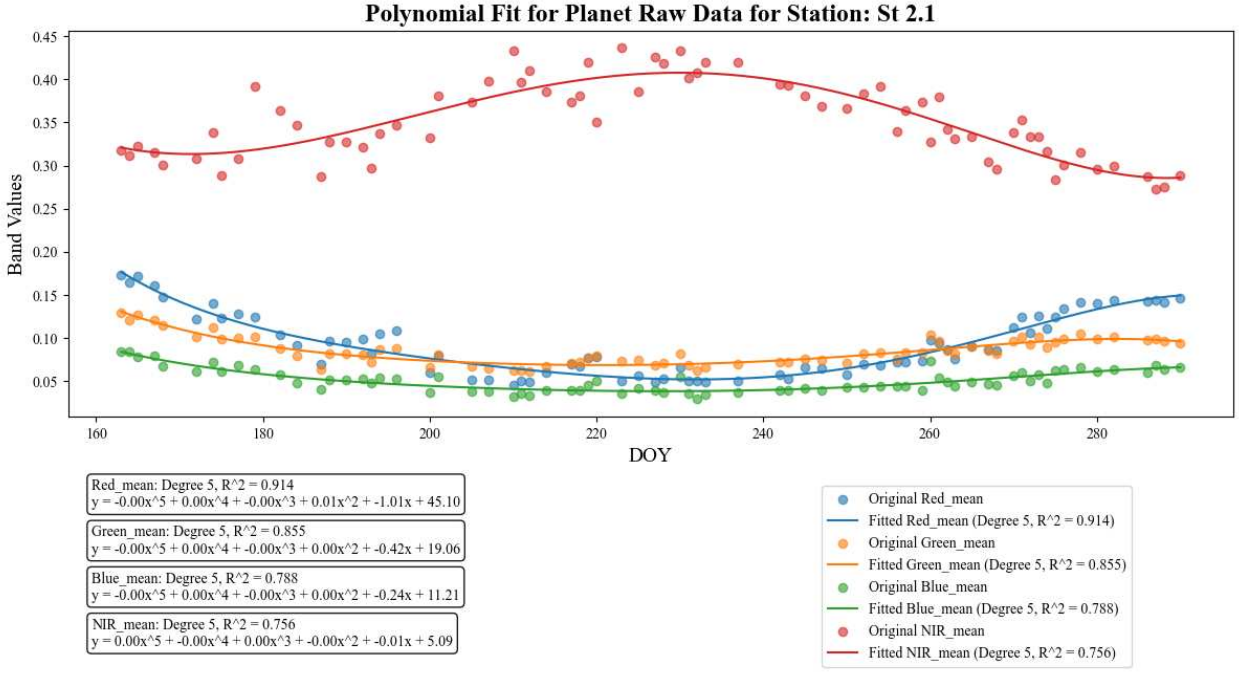
Polynomial Fit for Planet Raw Data for Station: St 2.1
Band Values
DOY
Red_mean: Degree 5, R^2 = 0.914
y = -0.00x^5 + 0.00x^4 + -0.00x^3 + 0.01x^2 + -1.01x + 45.10
Green_mean: Degree 5, R^2 = 0.855
y = -0.00x^5 + 0.00x^4 + -0.00x^3 + 0.00x^2 + -0.42x + 19.06
Blue_mean: Degree 5, R^2 = 0.788
y = -0.00x^5 + 0.00x^4 + -0.00x^3 + 0.00x^2 + -0.24x + 11.21
NIR_mean: Degree 5, R^2 = 0.756
y = 0.00x^5 + -0.00x^4 + 0.00x^3 + -0.00x^2 + -0.01x + 5.09
Original Red_mean
Fitted Red_mean (Degree 5, R^2 = 0.914)
Original Green_mean
Fitted Green_mean (Degree 5, R^2 = 0.855)
Original Blue_mean
Fitted Blue_mean (Degree 5, R^2 = 0.788)
Original NIR_mean
Fitted NIR_mean (Degree 5, R^2 = 0.756)

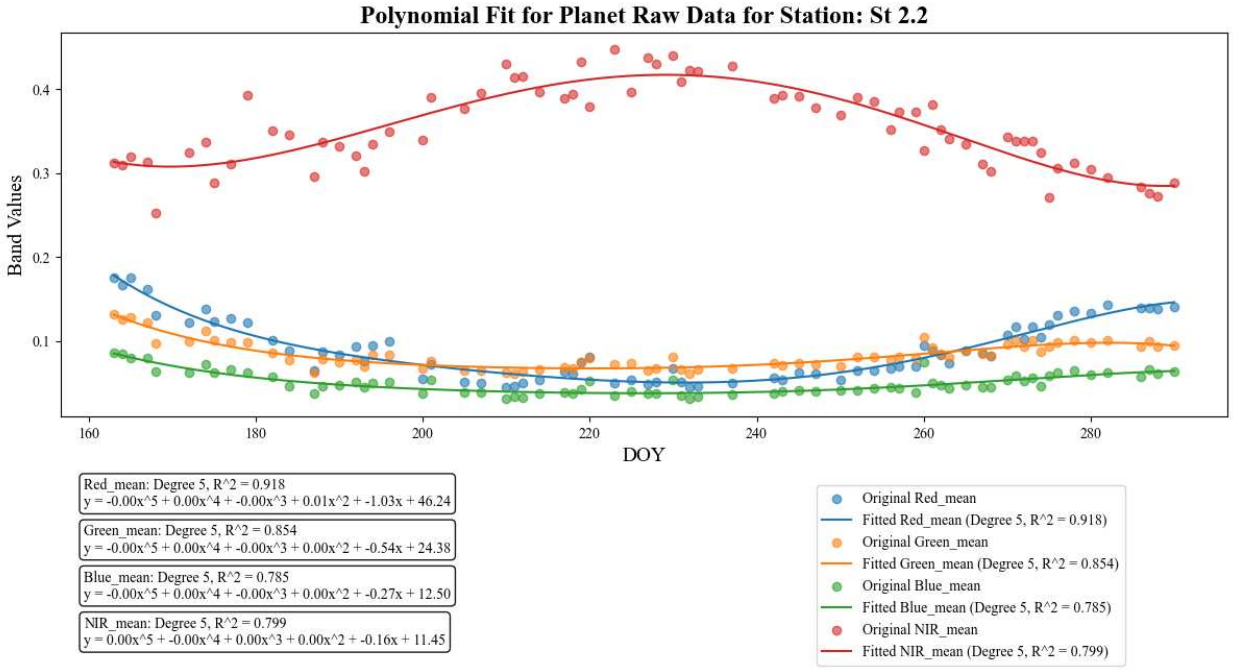
Polynomial Fit for Planet Raw Data for Station: St 2.2
Band Values
DOY
Red_mean: Degree 5, R^2 = 0.918
y = -0.00x^5 + 0.00x^4 + -0.00x^3 + 0.01x^2 + -1.03x + 46.24
Green_mean: Degree 5, R^2 = 0.854
y = -0.00x^5 + 0.00x^4 + -0.00x^3 + 0.00x^2 + -0.54x + 24.38
Blue_mean: Degree 5, R^2 = 0.785
y = -0.00x^5 + 0.00x^4 + -0.00x^3 + 0.00x^2 + -0.27x + 12.50
NIR_mean: Degree 5, R^2 = 0.799
y = 0.00x^5 + -0.00x^4 + 0.00x^3 + 0.00x^2 + -0.16x + 11.45
Original Red_mean
Fitted Red_mean (Degree 5, R^2 = 0.918)
Original Green_mean
Fitted Green_mean (Degree 5, R^2 = 0.854)
Original Blue_mean
Fitted Blue_mean (Degree 5, R^2 = 0.785)
Original NIR_mean
Fitted NIR_mean (Degree 5, R^2 = 0.799)

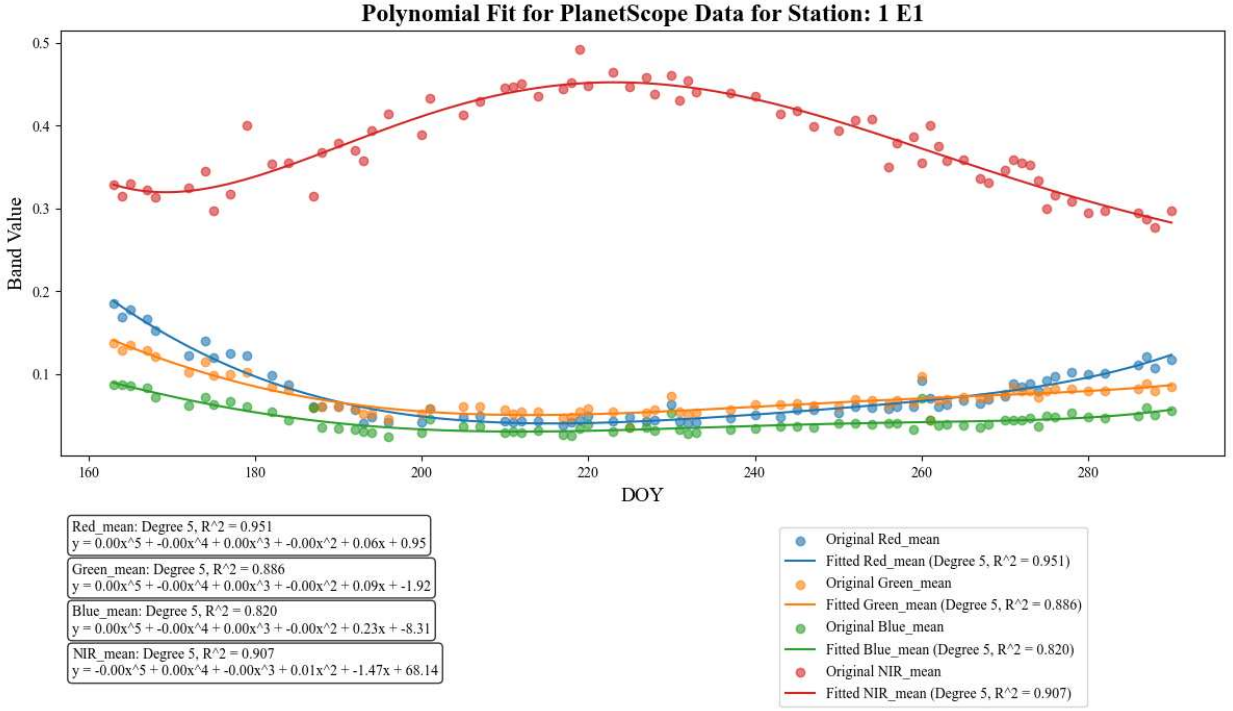
Polynomial Fit for PlanetScope Data for Station: 1 E1
Band Value
DOY
Red_mean: Degree 5, R^2 = 0.951
y = 0.00x^5 + -0.00x^4 + 0.00x^3 + -0.00x^2 + 0.06x + 0.95
Green_mean: Degree 5, R^2 = 0.886
y = 0.00x^5 + -0.00x^4 + 0.00x^3 + -0.00x^2 + 0.09x + -1.92
Blue_mean: Degree 5, R^2 = 0.820
y = 0.00x^5 + -0.00x^4 + 0.00x^3 + -0.00x^2 + 0.23x + -8.31
NIR_mean: Degree 5, R^2 = 0.907
y = -0.00x^5 + 0.00x^4 + -0.00x^3 + 0.01x^2 + -1.47x + 68.14
Original Red_mean
Fitted Red_mean (Degree 5, R^2 = 0.951)
Original Green_mean
Fitted Green_mean (Degree 5, R^2 = 0.886)
Original Blue_mean
Fitted Blue_mean (Degree 5, R^2 = 0.820)
Original NIR_mean
Fitted NIR_mean (Degree 5, R^2 = 0.907)

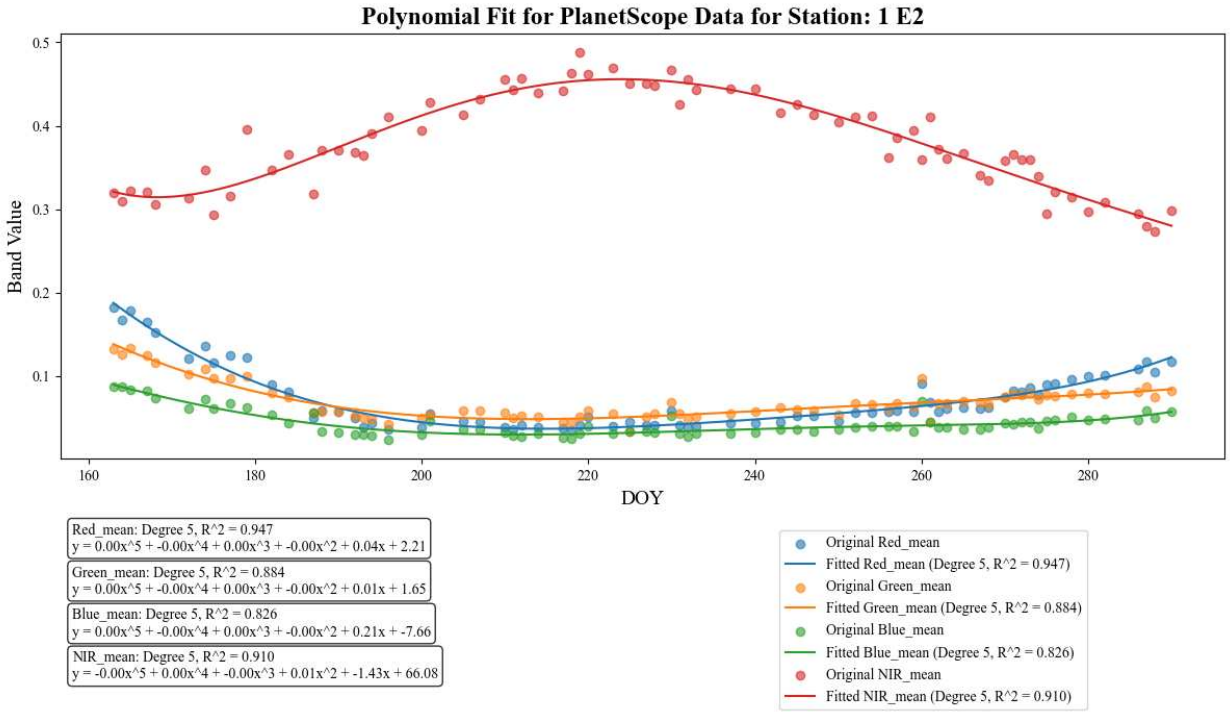
Polynomial Fit for PlanetScope Data for Station: 1 E2
Band Value
DOY
Red_mean: Degree 5, R^2 = 0.947
y = 0.00x^5 + -0.00x^4 + 0.00x^3 + -0.00x^2 + 0.04x + 2.21
Green_mean: Degree 5, R^2 = 0.884
y = 0.00x^5 + -0.00x^4 + 0.00x^3 + -0.00x^2 + 0.01x + 1.65
Blue_mean: Degree 5, R^2 = 0.826
y = 0.00x^5 + -0.00x^4 + 0.00x^3 + -0.00x^2 + 0.21x + -7.66
NIR_mean: Degree 5, R^2 = 0.910
y = -0.00x^5 + 0.00x^4 + -0.00x^3 + 0.01x^2 + -1.43x + 66.08
Original Red_mean
Fitted Red_mean (Degree 5, R^2 = 0.947)
Original Green_mean
Fitted Green_mean (Degree 5, R^2 = 0.884)
Original Blue_mean
Fitted Blue_mean (Degree 5, R^2 = 0.826)
Original NIR_mean
Fitted NIR_mean (Degree 5, R^2 = 0.910)

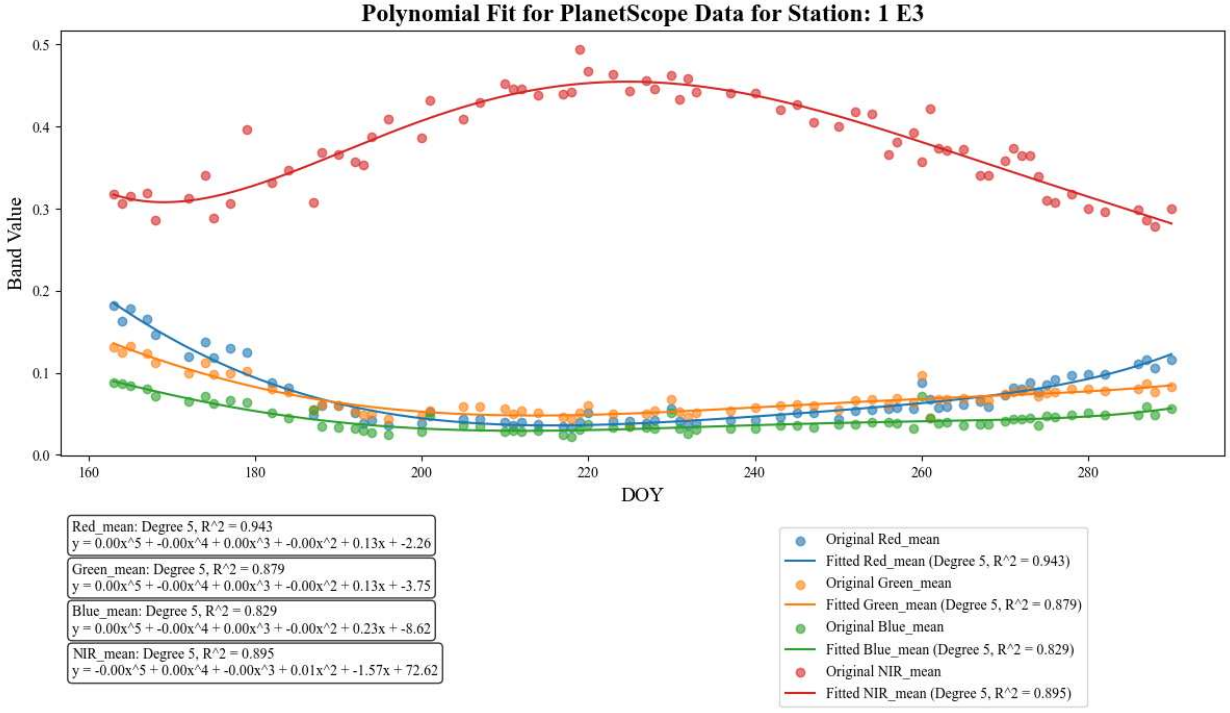
Polynomial Fit for PlanetScope Data for Station: 1 E3
Band Value
DOY
Red_mean: Degree 5, R^2 = 0.943
y = 0.00x^5 + -0.00x^4 + 0.00x^3 + -0.00x^2 + 0.13x + -2.26
Green_mean: Degree 5, R^2 = 0.879
y = 0.00x^5 + -0.00x^4 + 0.00x^3 + -0.00x^2 + 0.13x + -3.75
Blue_mean: Degree 5, R^2 = 0.829
y = 0.00x^5 + -0.00x^4 + 0.00x^3 + -0.00x^2 + 0.23x + -8.62
NIR_mean: Degree 5, R^2 = 0.895
y = -0.00x^5 + 0.00x^4 + -0.00x^3 + 0.01x^2 + -1.57x + 72.62
Original Red_mean
Fitted Red_mean (Degree 5, R^2 = 0.943)
Original Green_mean
Fitted Green_mean (Degree 5, R^2 = 0.879)
Original Blue_mean
Fitted Blue_mean (Degree 5, R^2 = 0.829)
Original NIR_mean
Fitted NIR_mean (Degree 5, R^2 = 0.895)

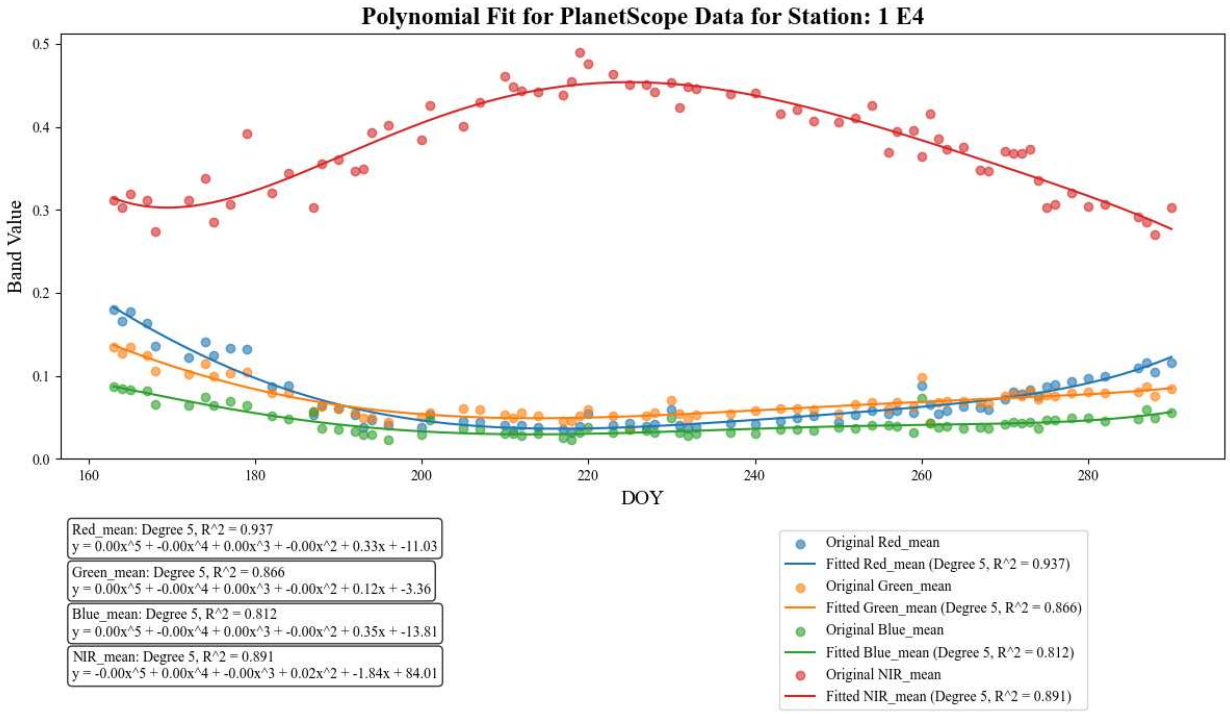
Polynomial Fit for PlanetScope Data for Station: 1 E4
Band Value
DOY
Red_mean: Degree 5, R^2 = 0.937
y = 0.00x^5 + -0.00x^4 + 0.00x^3 + -0.00x^2 + 0.33x + -11.03
Green_mean: Degree 5, R^2 = 0.866
y = 0.00x^5 + -0.00x^4 + 0.00x^3 + -0.00x^2 + 0.12x + -3.36
Blue_mean: Degree 5, R^2 = 0.812
y = 0.00x^5 + -0.00x^4 + 0.00x^3 + -0.00x^2 + 0.35x + -13.81
NIR_mean: Degree 5, R^2 = 0.891
y = -0.00x^5 + 0.00x^4 + -0.00x^3 + 0.02x^2 + -1.84x + 84.01
Original Red_mean
Fitted Red_mean (Degree 5, R^2 = 0.937)
Original Green_mean
Fitted Green_mean (Degree 5, R^2 = 0.866)
Original Blue_mean
Fitted Blue_mean (Degree 5, R^2 = 0.812)
Original NIR_mean
Fitted NIR_mean (Degree 5, R^2 = 0.891)

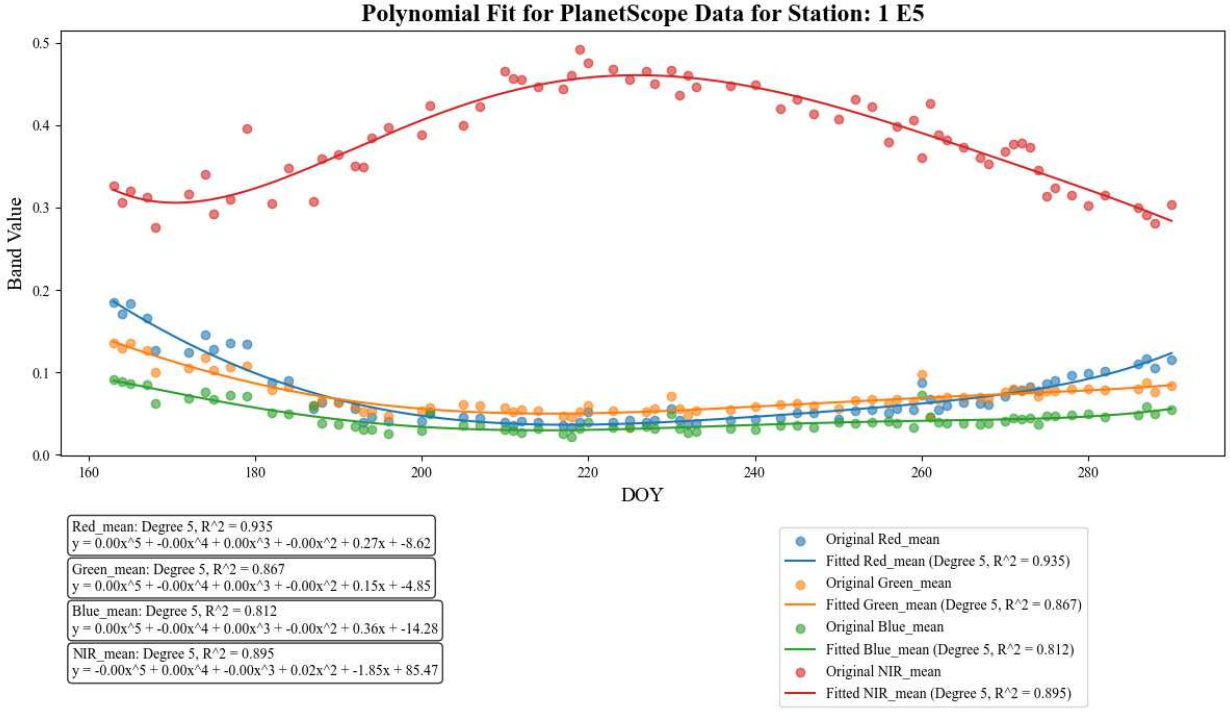
Polynomial Fit for PlanetScope Data for Station: 1 E5
Band Value
DOY
Red_mean: Degree 5, R^2 = 0.935
y = 0.00x^5 + -0.00x^4 + 0.00x^3 + -0.00x^2 + 0.27x + -8.62
Green_mean: Degree 5, R^2 = 0.867
y = 0.00x^5 + -0.00x^4 + 0.00x^3 + -0.00x^2 + 0.15x + -4.85
Blue_mean: Degree 5, R^2 = 0.812
y = 0.00x^5 + -0.00x^4 + 0.00x^3 + -0.00x^2 + 0.36x + -14.28
NIR_mean: Degree 5, R^2 = 0.895
y = -0.00x^5 + 0.00x^4 + -0.00x^3 + 0.02x^2 + -1.85x + 85.47
Original Red_mean
Fitted Red_mean (Degree 5, R^2 = 0.935)
Original Green_mean
Fitted Green_mean (Degree 5, R^2 = 0.867)
Original Blue_mean
Fitted Blue_mean (Degree 5, R^2 = 0.812)
Original NIR_mean
Fitted NIR_mean (Degree 5, R^2 = 0.895)

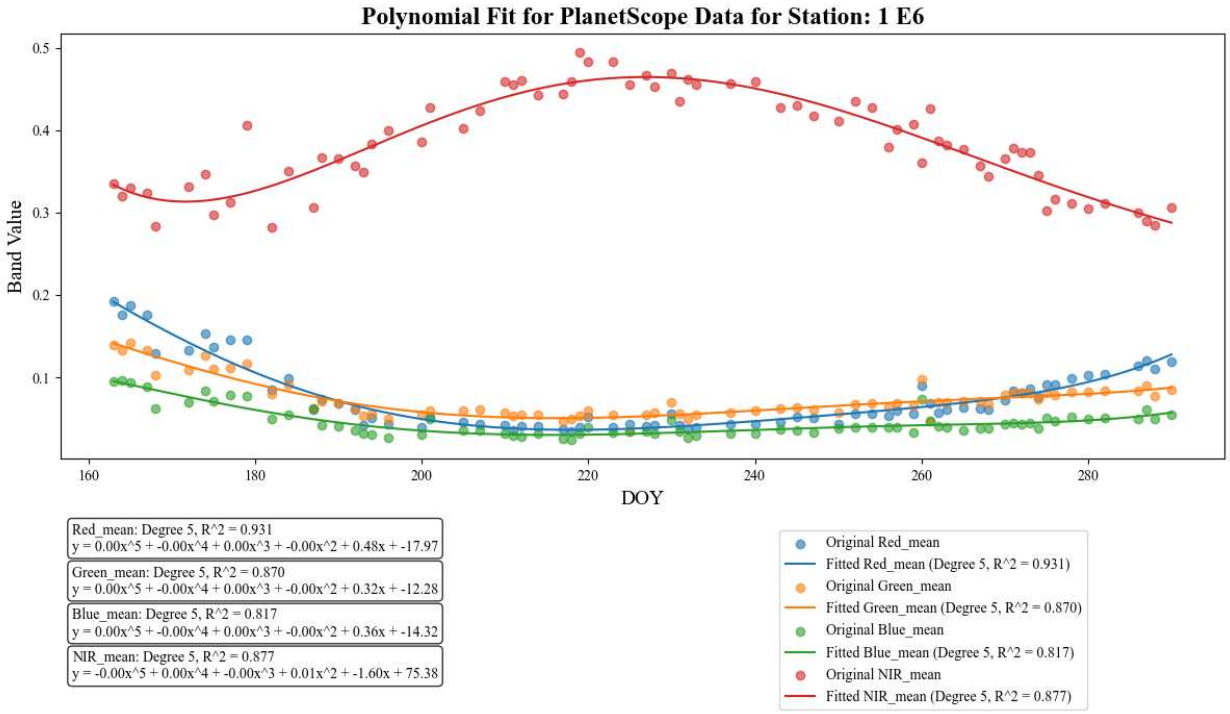
Polynomial Fit for PlanetScope Data for Station: 1 E6
Band Value
DOY
0.5
0.4
0.3
0.2
0.1
160
180
200
220
240
260
280
Red_mean: Degree 5, R^2 = 0.931
y = 0.00x^5 + -0.00x^4 + 0.00x^3 + -0.00x^2 + 0.48x + -17.97
Green_mean: Degree 5, R^2 = 0.870
y = 0.00x^5 + -0.00x^4 + 0.00x^3 + -0.00x^2 + 0.32x + -12.28
Blue_mean: Degree 5, R^2 = 0.817
y = 0.00x^5 + -0.00x^4 + 0.00x^3 + -0.00x^2 + 0.36x + -14.32
NIR_mean: Degree 5, R^2 = 0.877
y = -0.00x^5 + 0.00x^4 + -0.00x^3 + 0.01x^2 + -1.60x + 75.38
Original Red_mean
Fitted Red_mean (Degree 5, R^2 = 0.931)
Original Green_mean
Fitted Green_mean (Degree 5, R^2 = 0.870)
Original Blue_mean
Fitted Blue_mean (Degree 5, R^2 = 0.817)
Original NIR_mean
Fitted NIR_mean (Degree 5, R^2 = 0.877)

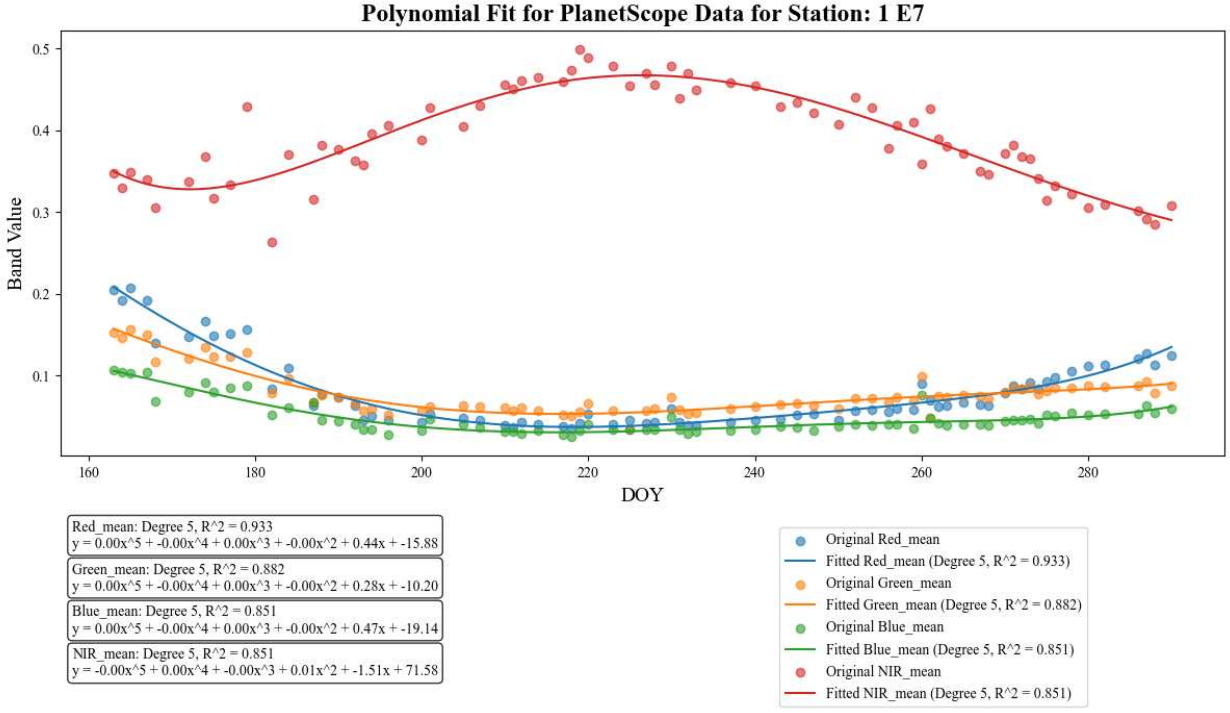
Polynomial Fit for PlanetScope Data for Station: 1 E7
Band Value
DOY
0.5
0.4
0.3
0.2
0.1
160
180
200
220
240
260
280
Red_mean: Degree 5, R^2 = 0.933
y = 0.00x^5 + -0.00x^4 + 0.00x^3 + -0.00x^2 + 0.44x + -15.88
Green_mean: Degree 5, R^2 = 0.882
y = 0.00x^5 + -0.00x^4 + 0.00x^3 + -0.00x^2 + 0.28x + -10.20
Blue_mean: Degree 5, R^2 = 0.851
y = 0.00x^5 + -0.00x^4 + 0.00x^3 + -0.00x^2 + 0.47x + -19.14
NIR_mean: Degree 5, R^2 = 0.851
y = -0.00x^5 + 0.00x^4 + -0.00x^3 + 0.01x^2 + -1.51x + 71.58
Original Red_mean
Fitted Red_mean (Degree 5, R^2 = 0.933)
Original Green_mean
Fitted Green_mean (Degree 5, R^2 = 0.882)
Original Blue_mean
Fitted Blue_mean (Degree 5, R^2 = 0.851)
Original NIR_mean
Fitted NIR_mean (Degree 5, R^2 = 0.851)

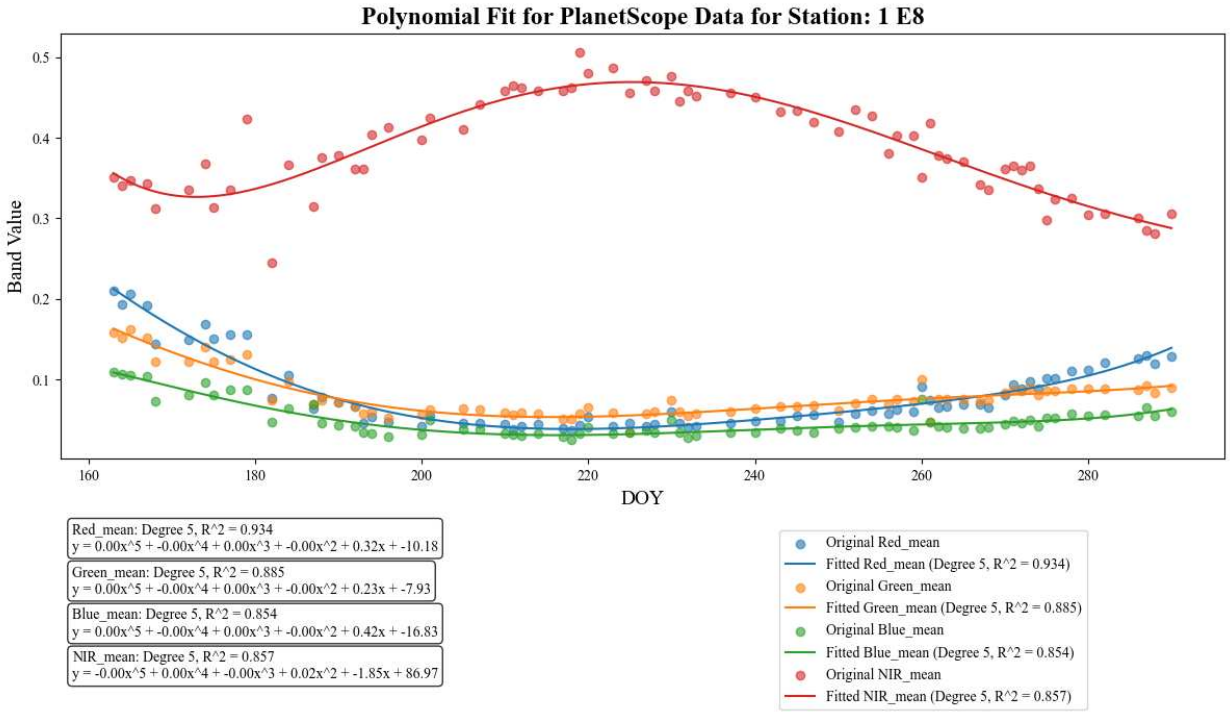
Polynomial Fit for PlanetScope Data for Station: 1 E8
Band Value
DOY
Red_mean: Degree 5, R^2 = 0.934
y = 0.00x^5 + -0.00x^4 + 0.00x^3 + -0.00x^2 + 0.32x + -10.18
Green_mean: Degree 5, R^2 = 0.885
y = 0.00x^5 + -0.00x^4 + 0.00x^3 + -0.00x^2 + 0.23x + -7.93
Blue_mean: Degree 5, R^2 = 0.854
y = 0.00x^5 + -0.00x^4 + 0.00x^3 + -0.00x^2 + 0.42x + -16.83
NIR_mean: Degree 5, R^2 = 0.857
y = -0.00x^5 + 0.00x^4 + -0.00x^3 + 0.02x^2 + -1.85x + 86.97
Original Red_mean
Fitted Red_mean (Degree 5, R^2 = 0.934)
Original Green_mean
Fitted Green_mean (Degree 5, R^2 = 0.885)
Original Blue_mean
Fitted Blue_mean (Degree 5, R^2 = 0.854)
Original NIR_mean
Fitted NIR_mean (Degree 5, R^2 = 0.857)

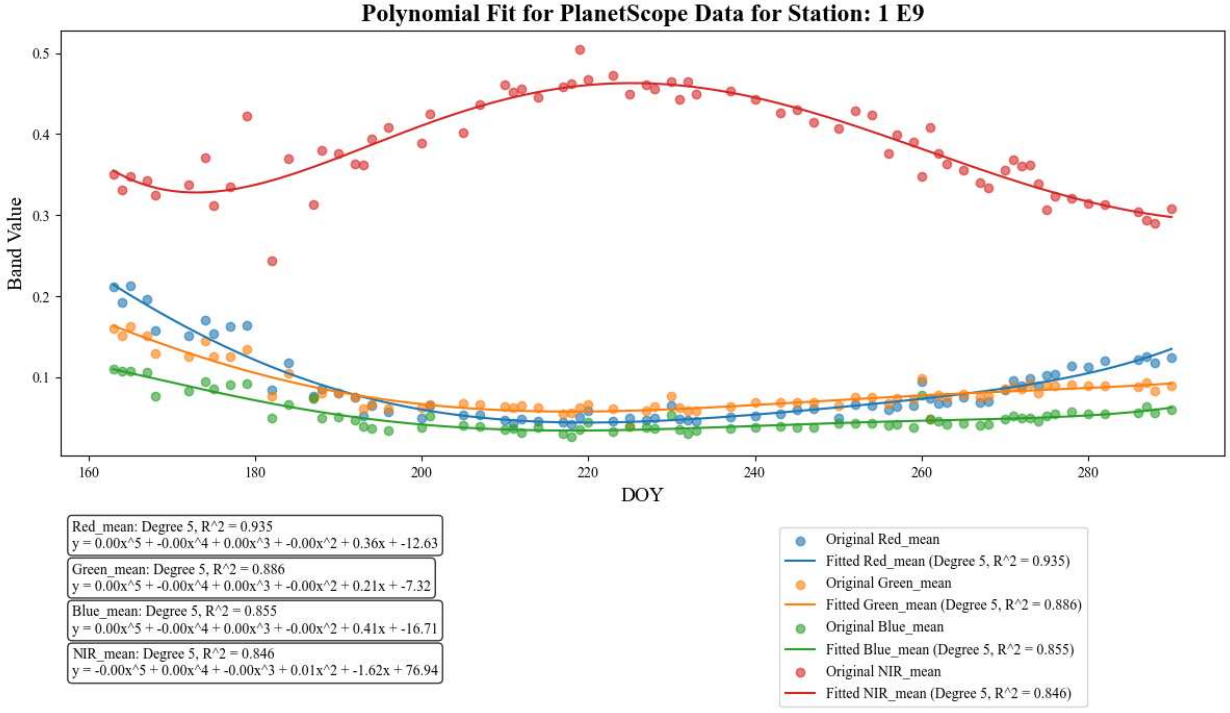
Polynomial Fit for PlanetScope Data for Station: 1 E9
Band Value
DOY
Red_mean: Degree 5, R^2 = 0.935
y = 0.00x^5 + -0.00x^4 + 0.00x^3 + -0.00x^2 + 0.36x + -12.63
Green_mean: Degree 5, R^2 = 0.886
y = 0.00x^5 + -0.00x^4 + 0.00x^3 + -0.00x^2 + 0.21x + -7.32
Blue_mean: Degree 5, R^2 = 0.855
y = 0.00x^5 + -0.00x^4 + 0.00x^3 + -0.00x^2 + 0.41x + -16.71
NIR_mean: Degree 5, R^2 = 0.846
y = -0.00x^5 + 0.00x^4 + -0.00x^3 + 0.01x^2 + -1.62x + 76.94
Original Red_mean
Fitted Red_mean (Degree 5, R^2 = 0.935)
Original Green_mean
Fitted Green_mean (Degree 5, R^2 = 0.886)
Original Blue_mean
Fitted Blue_mean (Degree 5, R^2 = 0.855)
Original NIR_mean
Fitted NIR_mean (Degree 5, R^2 = 0.846)

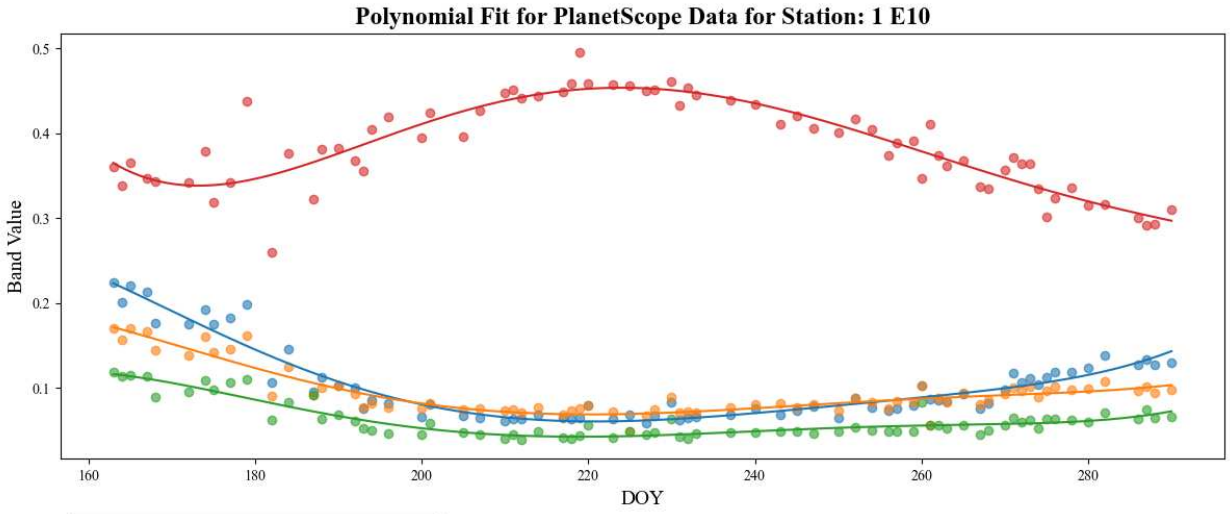

Red_mean: Degree 5, R^2 = 0.919
y = 0.00x^5 + -0.00x^4 + 0.00x^3 + -0.01x^2 + 0.78x + -31.92

Green_mean: Degree 5, R^2 = 0.871
y = 0.00x^5 + -0.00x^4 + 0.00x^3 + -0.00x^2 + 0.52x + -21.67

Blue_mean: Degree 5, R^2 = 0.851
y = 0.00x^5 + -0.00x^4 + 0.00x^3 + -0.01x^2 + 0.74x + -31.60

NIR_mean: Degree 5, R^2 = 0.818
y = -0.00x^5 + 0.00x^4 + -0.00x^3 + 0.01x^2 + -1.69x + 79.11

Original Red_mean
Fitted Red_mean (Degree 5, R^2 = 0.919)
Original Green_mean
Fitted Green_mean (Degree 5, R^2 = 0.871)
Original Blue_mean
Fitted Blue_mean (Degree 5, R^2 = 0.851)
Original NIR_mean
Fitted NIR_mean (Degree 5, R^2 = 0.818)

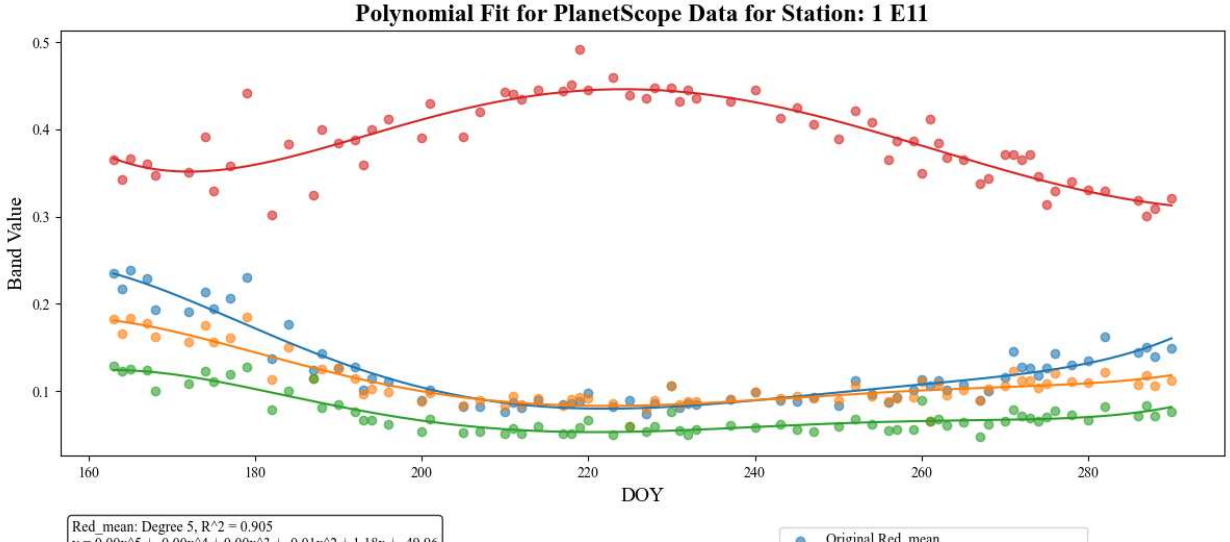

Red_mean: Degree 5, R^2 = 0.905
y = 0.00x^5 + -0.00x^4 + 0.00x^3 + -0.01x^2 + 1.18x + -49.96

Green_mean: Degree 5, R^2 = 0.854
y = 0.00x^5 + -0.00x^4 + 0.00x^3 + -0.01x^2 + 0.82x + -35.13

Blue_mean: Degree 5, R^2 = 0.838
y = 0.00x^5 + -0.00x^4 + 0.00x^3 + -0.01x^2 + 0.97x + -41.87

NIR_mean: Degree 5, R^2 = 0.792
y = -0.00x^5 + 0.00x^4 + -0.00x^3 + 0.01x^2 + -1.03x + 49.33

Original Red_mean
Fitted Red_mean (Degree 5, R^2 = 0.905)
Original Green_mean
Fitted Green_mean (Degree 5, R^2 = 0.854)
Original Blue_mean
Fitted Blue_mean (Degree 5, R^2 = 0.838)
Original NIR_mean
Fitted NIR_mean (Degree 5, R^2 = 0.792)

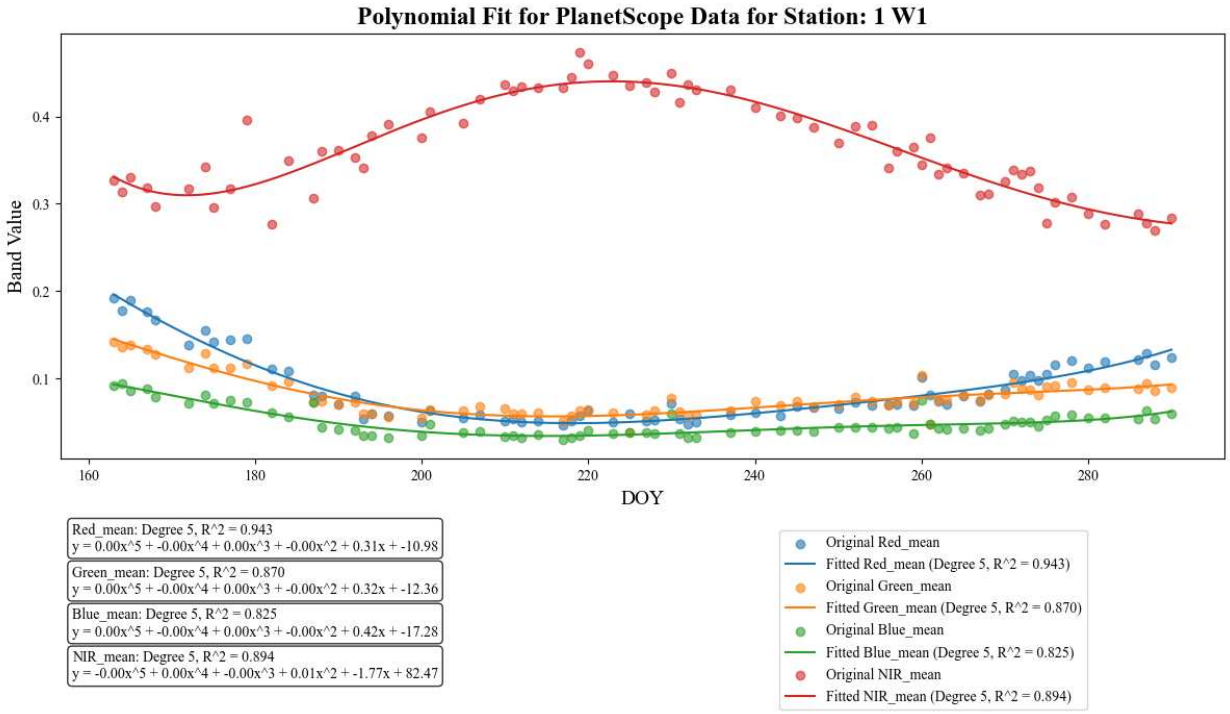
Polynomial Fit for PlanetScope Data for Station: 1 W1
Band Value
DOY
0.1
0.2
0.3
0.4
160
180
200
220
240
260
280
Red_mean: Degree 5, R^2 = 0.943
y = 0.00x^5 + -0.00x^4 + 0.00x^3 + -0.00x^2 + 0.31x + -10.98
Green_mean: Degree 5, R^2 = 0.870
y = 0.00x^5 + -0.00x^4 + 0.00x^3 + -0.00x^2 + 0.32x + -12.36
Blue_mean: Degree 5, R^2 = 0.825
y = 0.00x^5 + -0.00x^4 + 0.00x^3 + -0.00x^2 + 0.42x + -17.28
NIR_mean: Degree 5, R^2 = 0.894
y = -0.00x^5 + 0.00x^4 + -0.00x^3 + 0.01x^2 + -1.77x + 82.47
Original Red_mean
Fitted Red_mean (Degree 5, R^2 = 0.943)
Original Green_mean
Fitted Green_mean (Degree 5, R^2 = 0.870)
Original Blue_mean
Fitted Blue_mean (Degree 5, R^2 = 0.825)
Original NIR_mean
Fitted NIR_mean (Degree 5, R^2 = 0.894)

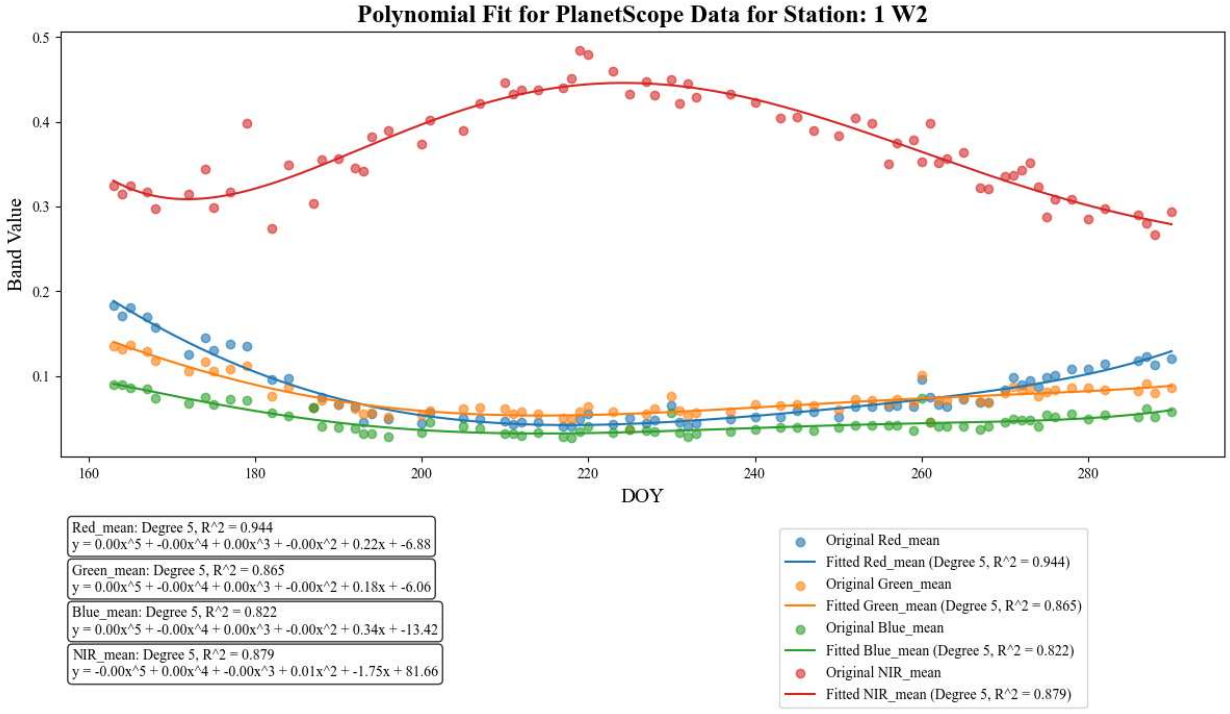
Polynomial Fit for PlanetScope Data for Station: 1 W2
Band Value
DOY
0.1
0.2
0.3
0.4
0.5
160
180
200
220
240
260
280
Red_mean: Degree 5, R^2 = 0.944
y = 0.00x^5 + -0.00x^4 + 0.00x^3 + -0.00x^2 + 0.22x + -6.88
Green_mean: Degree 5, R^2 = 0.865
y = 0.00x^5 + -0.00x^4 + 0.00x^3 + -0.00x^2 + 0.18x + -6.06
Blue_mean: Degree 5, R^2 = 0.822
y = 0.00x^5 + -0.00x^4 + 0.00x^3 + -0.00x^2 + 0.34x + -13.42
NIR_mean: Degree 5, R^2 = 0.879
y = -0.00x^5 + 0.00x^4 + -0.00x^3 + 0.01x^2 + -1.75x + 81.66
Original Red_mean
Fitted Red_mean (Degree 5, R^2 = 0.944)
Original Green_mean
Fitted Green_mean (Degree 5, R^2 = 0.865)
Original Blue_mean
Fitted Blue_mean (Degree 5, R^2 = 0.822)
Original NIR_mean
Fitted NIR_mean (Degree 5, R^2 = 0.879)

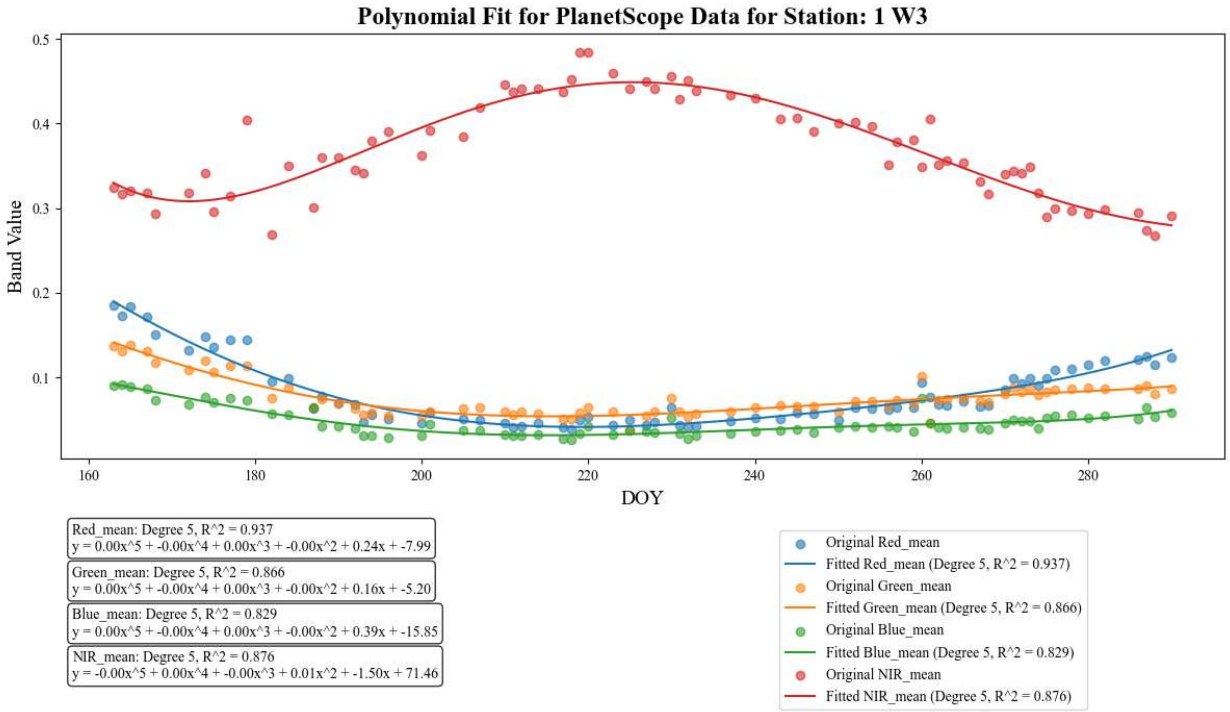
Polynomial Fit for PlanetScope Data for Station: 1 W3
Band Value
DOY
0.5
0.4
0.3
0.2
0.1
160
180
200
220
240
260
280
Red_mean: Degree 5, R^2 = 0.937
y = 0.00x^5 + -0.00x^4 + 0.00x^3 + -0.00x^2 + 0.24x + -7.99
Green_mean: Degree 5, R^2 = 0.866
y = 0.00x^5 + -0.00x^4 + 0.00x^3 + -0.00x^2 + 0.16x + -5.20
Blue_mean: Degree 5, R^2 = 0.829
y = 0.00x^5 + -0.00x^4 + 0.00x^3 + -0.00x^2 + 0.39x + -15.85
NIR_mean: Degree 5, R^2 = 0.876
y = -0.00x^5 + 0.00x^4 + -0.00x^3 + 0.01x^2 + -1.50x + 71.46
Original Red_mean
Fitted Red_mean (Degree 5, R^2 = 0.937)
Original Green_mean
Fitted Green_mean (Degree 5, R^2 = 0.866)
Original Blue_mean
Fitted Blue_mean (Degree 5, R^2 = 0.829)
Original NIR_mean
Fitted NIR_mean (Degree 5, R^2 = 0.876)

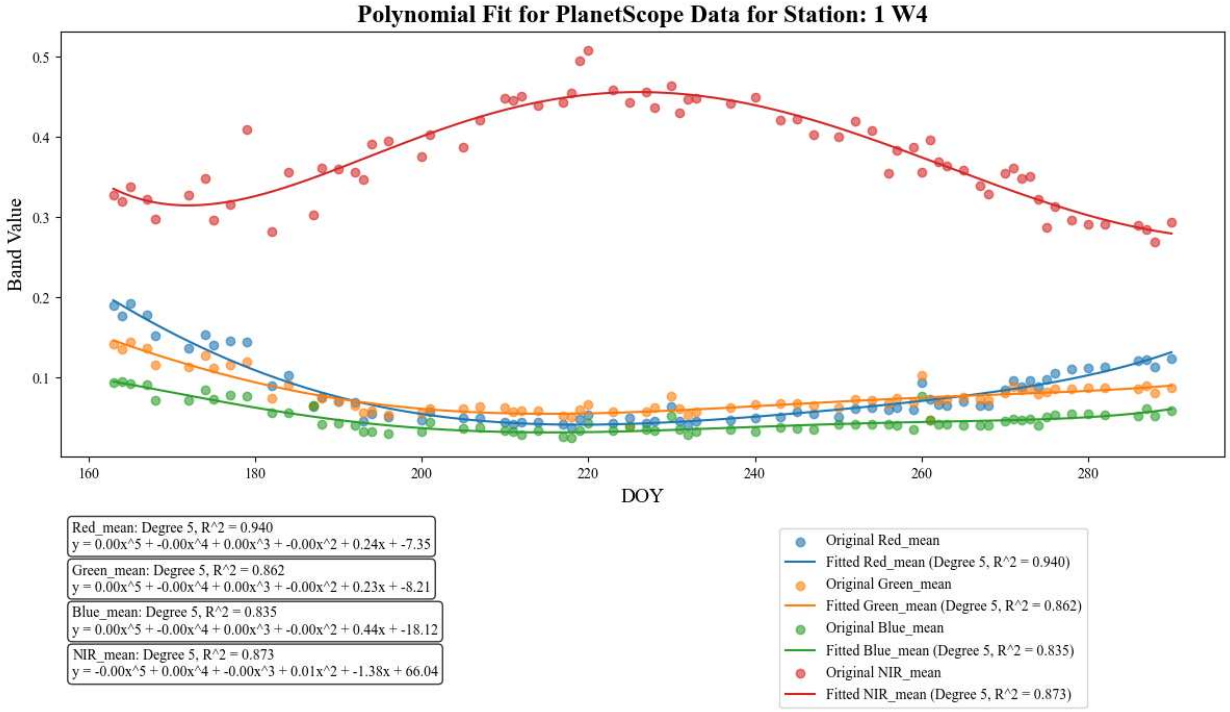
Polynomial Fit for PlanetScope Data for Station: 1 W4
Band Value
DOY
0.5
0.4
0.3
0.2
0.1
160
180
200
220
240
260
280
Red_mean: Degree 5, R^2 = 0.940
y = 0.00x^5 + -0.00x^4 + 0.00x^3 + -0.00x^2 + 0.24x + -7.35
Green_mean: Degree 5, R^2 = 0.862
y = 0.00x^5 + -0.00x^4 + 0.00x^3 + -0.00x^2 + 0.23x + -8.21
Blue_mean: Degree 5, R^2 = 0.835
y = 0.00x^5 + -0.00x^4 + 0.00x^3 + -0.00x^2 + 0.44x + -18.12
NIR_mean: Degree 5, R^2 = 0.873
y = -0.00x^5 + 0.00x^4 + -0.00x^3 + 0.01x^2 + -1.38x + 66.04
Original Red_mean
Fitted Red_mean (Degree 5, R^2 = 0.940)
Original Green_mean
Fitted Green_mean (Degree 5, R^2 = 0.862)
Original Blue_mean
Fitted Blue_mean (Degree 5, R^2 = 0.835)
Original NIR_mean
Fitted NIR_mean (Degree 5, R^2 = 0.873)

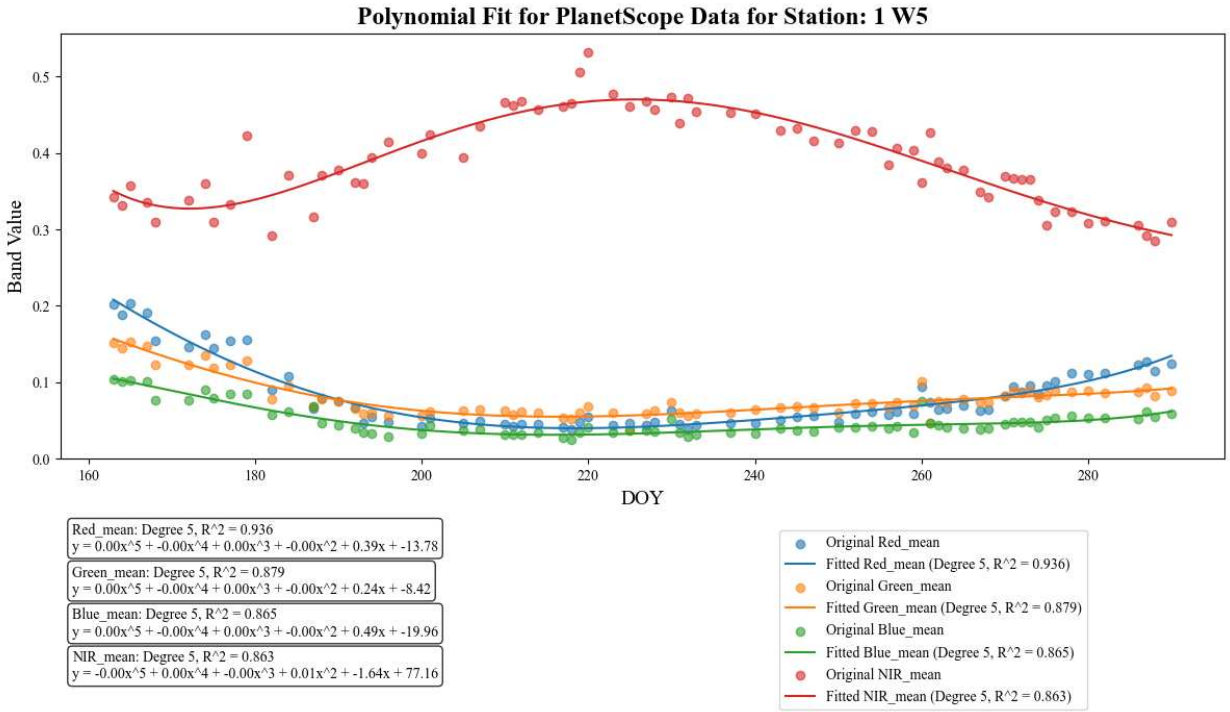
Polynomial Fit for PlanetScope Data for Station: 1 W5
Band Value
DOY
Red_mean: Degree 5, R^2 = 0.936
y = 0.00x^5 + -0.00x^4 + 0.00x^3 + -0.00x^2 + 0.39x + -13.78
Green_mean: Degree 5, R^2 = 0.879
y = 0.00x^5 + -0.00x^4 + 0.00x^3 + -0.00x^2 + 0.24x + -8.42
Blue_mean: Degree 5, R^2 = 0.865
y = 0.00x^5 + -0.00x^4 + 0.00x^3 + -0.00x^2 + 0.49x + -19.96
NIR_mean: Degree 5, R^2 = 0.863
y = -0.00x^5 + 0.00x^4 + -0.00x^3 + 0.01x^2 + -1.64x + 77.16
Original Red_mean
Fitted Red_mean (Degree 5, R^2 = 0.936)
Original Green_mean
Fitted Green_mean (Degree 5, R^2 = 0.879)
Original Blue_mean
Fitted Blue_mean (Degree 5, R^2 = 0.865)
Original NIR_mean
Fitted NIR_mean (Degree 5, R^2 = 0.863)

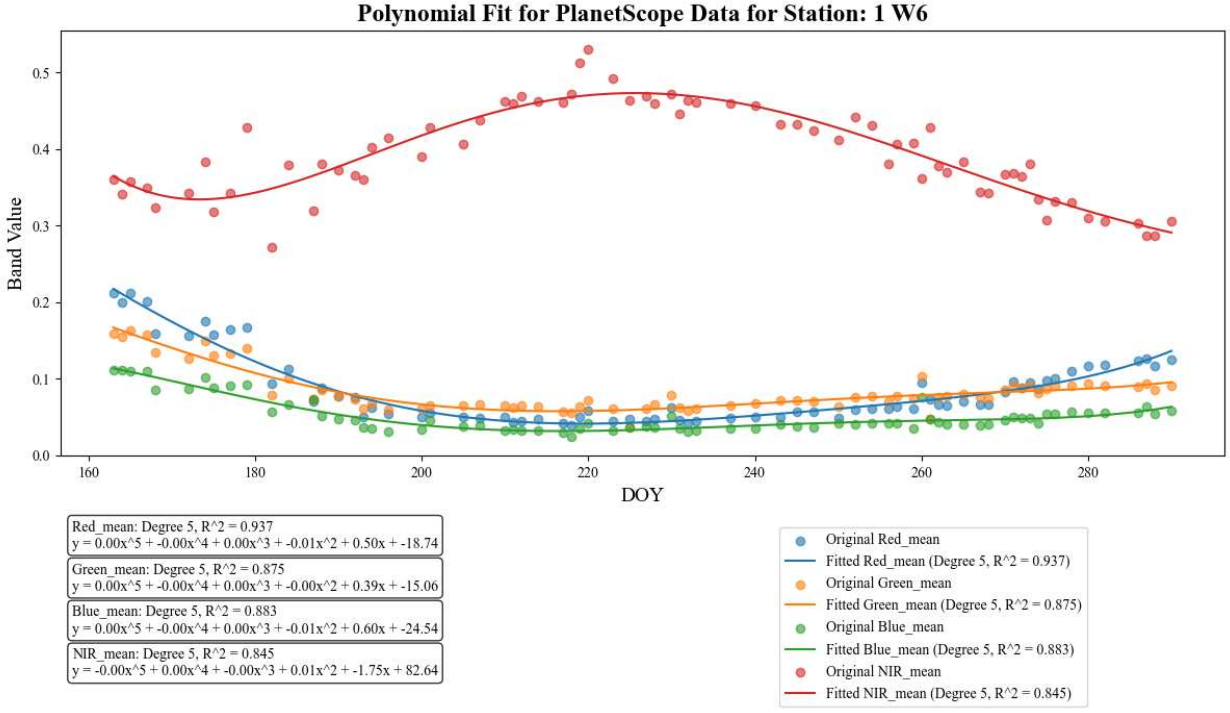
Polynomial Fit for PlanetScope Data for Station: 1 W6
Band Value
DOY
Red_mean: Degree 5, R^2 = 0.937
y = 0.00x^5 + -0.00x^4 + 0.00x^3 + -0.01x^2 + 0.50x + -18.74
Green_mean: Degree 5, R^2 = 0.875
y = 0.00x^5 + -0.00x^4 + 0.00x^3 + -0.00x^2 + 0.39x + -15.06
Blue_mean: Degree 5, R^2 = 0.883
y = 0.00x^5 + -0.00x^4 + 0.00x^3 + -0.01x^2 + 0.60x + -24.54
NIR_mean: Degree 5, R^2 = 0.845
y = -0.00x^5 + 0.00x^4 + -0.00x^3 + 0.01x^2 + -1.75x + 82.64
Original Red_mean
Fitted Red_mean (Degree 5, R^2 = 0.937)
Original Green_mean
Fitted Green_mean (Degree 5, R^2 = 0.875)
Original Blue_mean
Fitted Blue_mean (Degree 5, R^2 = 0.883)
Original NIR_mean
Fitted NIR_mean (Degree 5, R^2 = 0.845)

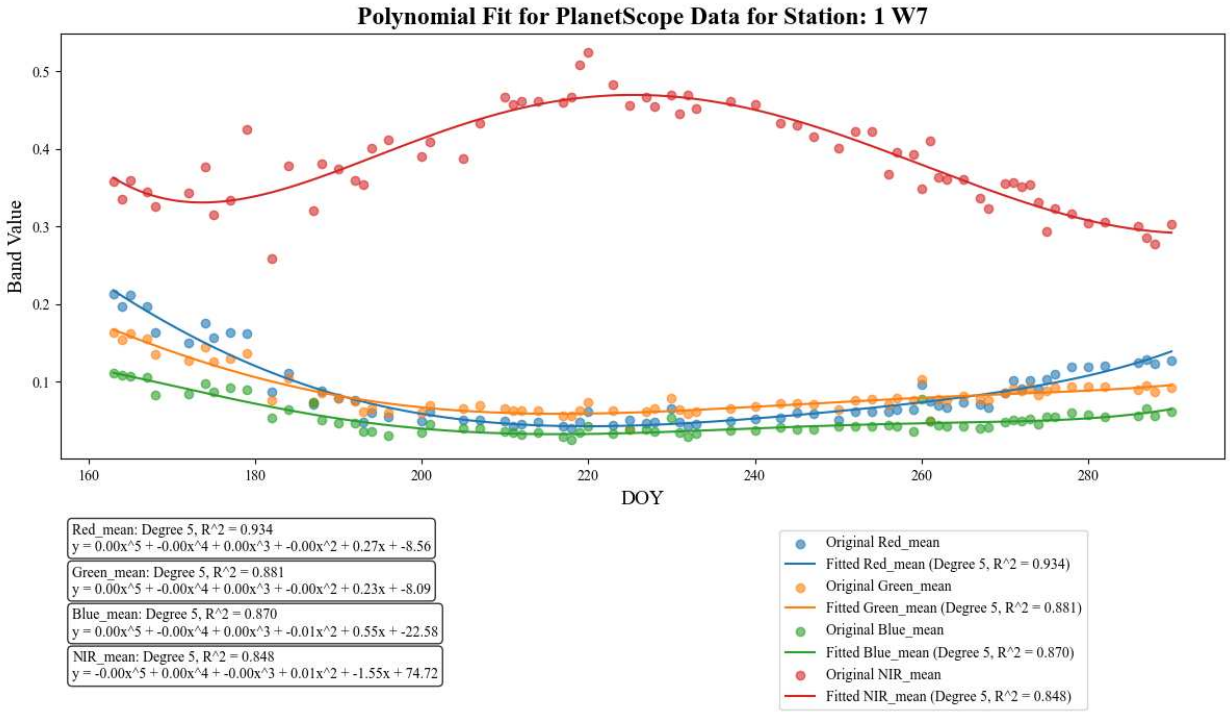
Polynomial Fit for PlanetScope Data for Station: 1 W7
Band Value
DOY
Red_mean: Degree 5, R^2 = 0.934
y = 0.00x^5 + -0.00x^4 + 0.00x^3 + -0.00x^2 + 0.27x + -8.56
Green_mean: Degree 5, R^2 = 0.881
y = 0.00x^5 + -0.00x^4 + 0.00x^3 + -0.00x^2 + 0.23x + -8.09
Blue_mean: Degree 5, R^2 = 0.870
y = 0.00x^5 + -0.00x^4 + 0.00x^3 + -0.01x^2 + 0.55x + -22.58
NIR_mean: Degree 5, R^2 = 0.848
y = -0.00x^5 + 0.00x^4 + -0.00x^3 + 0.01x^2 + -1.55x + 74.72
Original Red_mean
Fitted Red_mean (Degree 5, R^2 = 0.934)
Original Green_mean
Fitted Green_mean (Degree 5, R^2 = 0.881)
Original Blue_mean
Fitted Blue_mean (Degree 5, R^2 = 0.870)
Original NIR_mean
Fitted NIR_mean (Degree 5, R^2 = 0.848)

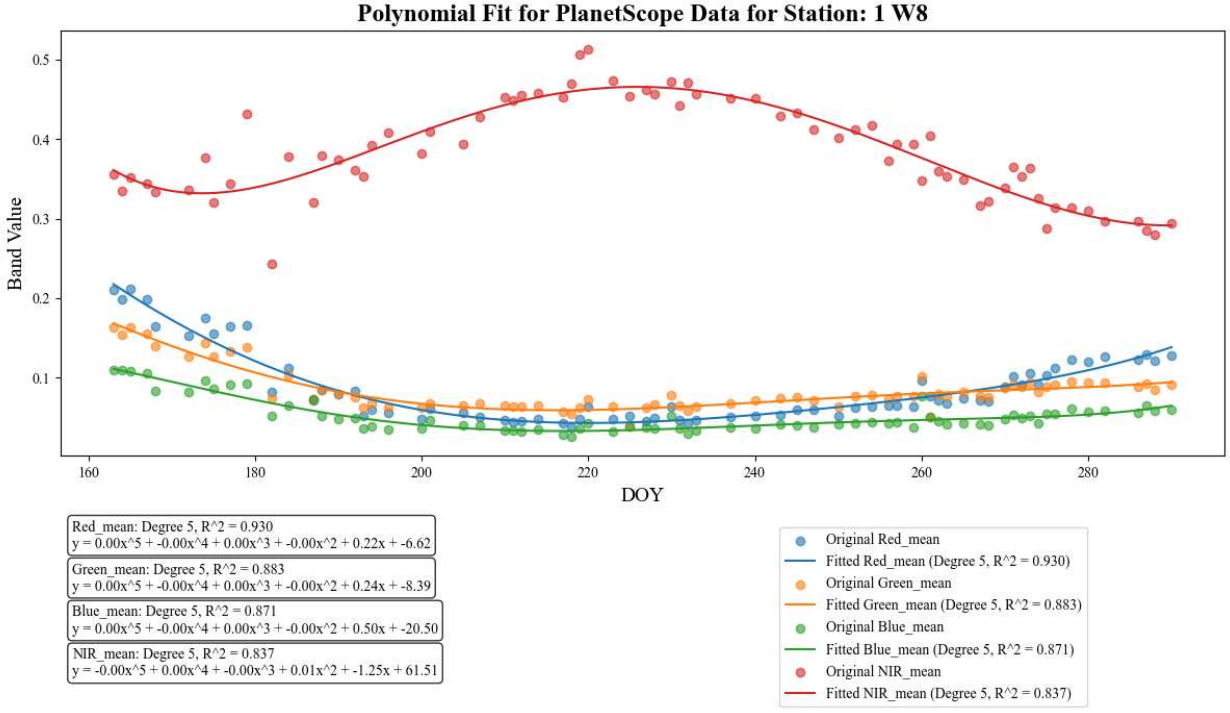
Polynomial Fit for PlanetScope Data for Station: 1 W8
Band Value
DOY
Red_mean: Degree 5, R^2 = 0.930
y = 0.00x^5 + -0.00x^4 + 0.00x^3 + -0.00x^2 + 0.22x + -6.62
Green_mean: Degree 5, R^2 = 0.883
y = 0.00x^5 + -0.00x^4 + 0.00x^3 + -0.00x^2 + 0.24x + -8.39
Blue_mean: Degree 5, R^2 = 0.871
y = 0.00x^5 + -0.00x^4 + 0.00x^3 + -0.00x^2 + 0.50x + -20.50
NIR_mean: Degree 5, R^2 = 0.837
y = -0.00x^5 + 0.00x^4 + -0.00x^3 + 0.01x^2 + -1.25x + 61.51
Original Red_mean
Fitted Red_mean (Degree 5, R^2 = 0.930)
Original Green_mean
Fitted Green_mean (Degree 5, R^2 = 0.883)
Original Blue_mean
Fitted Blue_mean (Degree 5, R^2 = 0.871)
Original NIR_mean
Fitted NIR_mean (Degree 5, R^2 = 0.837)

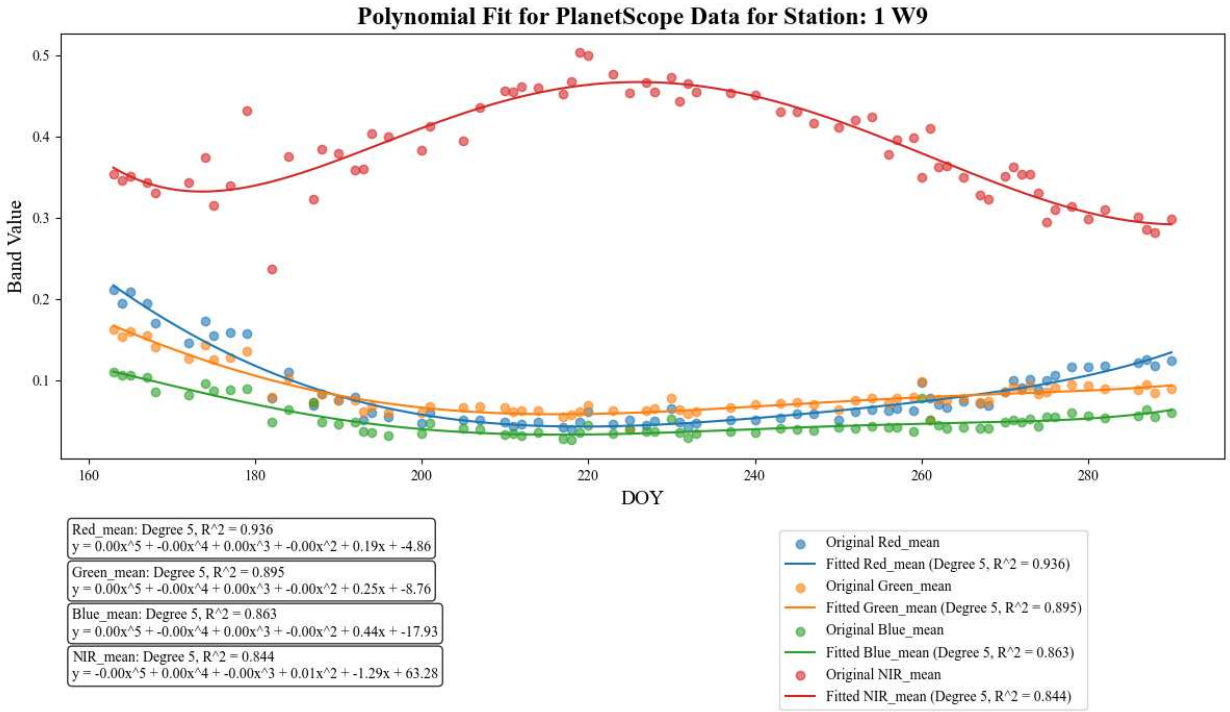
Polynomial Fit for PlanetScope Data for Station: 1 W9
Band Value
DOY
Red_mean: Degree 5, R^2 = 0.936
y = 0.00x^5 + -0.00x^4 + 0.00x^3 + -0.00x^2 + 0.19x + -4.86
Green_mean: Degree 5, R^2 = 0.895
y = 0.00x^5 + -0.00x^4 + 0.00x^3 + -0.00x^2 + 0.25x + -8.76
Blue_mean: Degree 5, R^2 = 0.863
y = 0.00x^5 + -0.00x^4 + 0.00x^3 + -0.00x^2 + 0.44x + -17.93
NIR_mean: Degree 5, R^2 = 0.844
y = -0.00x^5 + 0.00x^4 + -0.00x^3 + 0.01x^2 + -1.29x + 63.28
Original Red_mean
Fitted Red_mean (Degree 5, R^2 = 0.936)
Original Green_mean
Fitted Green_mean (Degree 5, R^2 = 0.895)
Original Blue_mean
Fitted Blue_mean (Degree 5, R^2 = 0.863)
Original NIR_mean
Fitted NIR_mean (Degree 5, R^2 = 0.844)

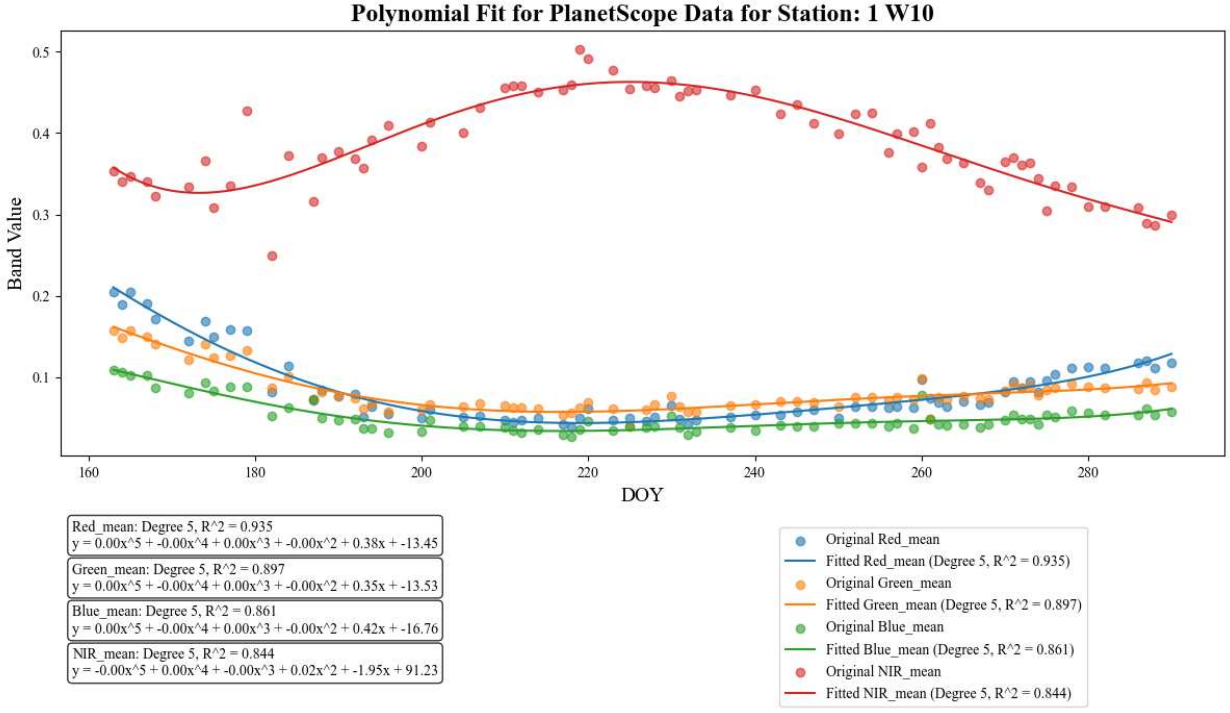
Polynomial Fit for PlanetScope Data for Station: 1 W10
Band Value
DOY
Red_mean: Degree 5, R^2 = 0.935
y = 0.00x^5 + -0.00x^4 + 0.00x^3 + -0.00x^2 + 0.38x + -13.45
Green_mean: Degree 5, R^2 = 0.897
y = 0.00x^5 + -0.00x^4 + 0.00x^3 + -0.00x^2 + 0.35x + -13.53
Blue_mean: Degree 5, R^2 = 0.861
y = 0.00x^5 + -0.00x^4 + 0.00x^3 + -0.00x^2 + 0.42x + -16.76
NIR_mean: Degree 5, R^2 = 0.844
y = -0.00x^5 + 0.00x^4 + -0.00x^3 + 0.02x^2 + -1.95x + 91.23
Original Red_mean
Fitted Red_mean (Degree 5, R^2 = 0.935)
Original Green_mean
Fitted Green_mean (Degree 5, R^2 = 0.897)
Original Blue_mean
Fitted Blue_mean (Degree 5, R^2 = 0.861)
Original NIR_mean
Fitted NIR_mean (Degree 5, R^2 = 0.844)

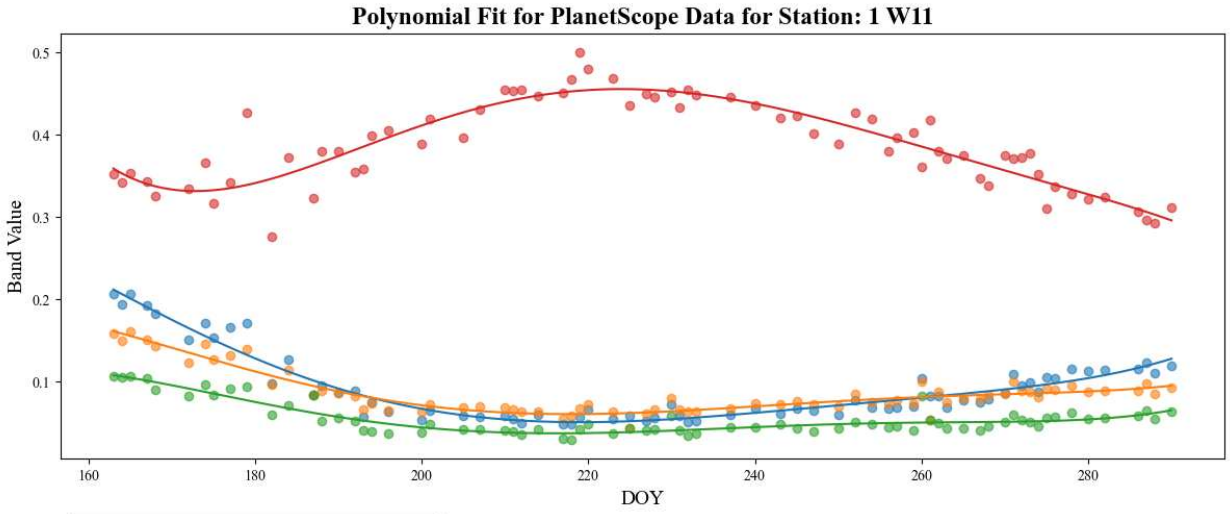

Red_mean: Degree 5, R^2 = 0.933
y = 0.00x^5 + -0.00x^4 + 0.00x^3 + -0.01x^2 + 0.60x + -23.36

Green_mean: Degree 5, R^2 = 0.897
y = 0.00x^5 + -0.00x^4 + 0.00x^3 + -0.01x^2 + 0.57x + -23.41

Blue_mean: Degree 5, R^2 = 0.843
y = 0.00x^5 + -0.00x^4 + 0.00x^3 + -0.01x^2 + 0.68x + -28.52

NIR_mean: Degree 5, R^2 = 0.829
y = -0.00x^5 + 0.00x^4 + -0.00x^3 + 0.02x^2 + -2.05x + 94.42

Original Red_mean
Fitted Red_mean (Degree 5, R^2 = 0.933)
Original Green_mean
Fitted Green_mean (Degree 5, R^2 = 0.897)
Original Blue_mean
Fitted Blue_mean (Degree 5, R^2 = 0.843)
Original NIR_mean
Fitted NIR_mean (Degree 5, R^2 = 0.829)

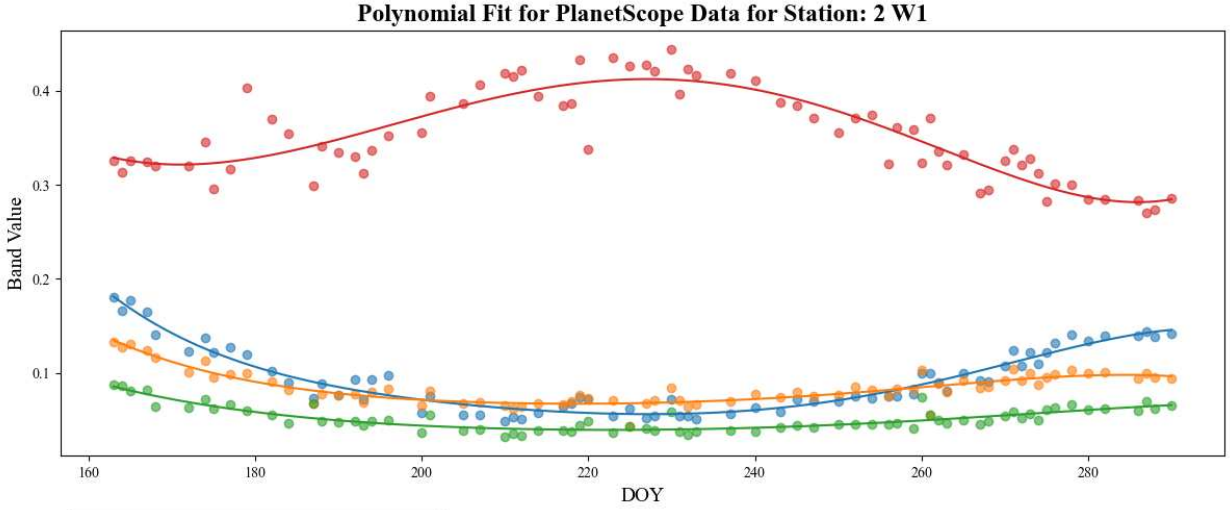

Red_mean: Degree 5, R^2 = 0.935
y = -0.00x^5 + 0.00x^4 + -0.00x^3 + 0.01x^2 + -0.89x + 40.30

Green_mean: Degree 5, R^2 = 0.832
y = -0.00x^5 + 0.00x^4 + -0.00x^3 + 0.00x^2 + -0.40x + 18.82

Blue_mean: Degree 5, R^2 = 0.786
y = -0.00x^5 + 0.00x^4 + -0.00x^3 + 0.00x^2 + -0.14x + 6.89

NIR_mean: Degree 5, R^2 = 0.785
y = 0.00x^5 + -0.00x^4 + 0.00x^3 + -0.00x^2 + -0.05x + 7.03

Original Red_mean
Fitted Red_mean (Degree 5, R^2 = 0.935)
Original Green_mean
Fitted Green_mean (Degree 5, R^2 = 0.832)
Original Blue_mean
Fitted Blue_mean (Degree 5, R^2 = 0.786)
Original NIR_mean
Fitted NIR_mean (Degree 5, R^2 = 0.785)

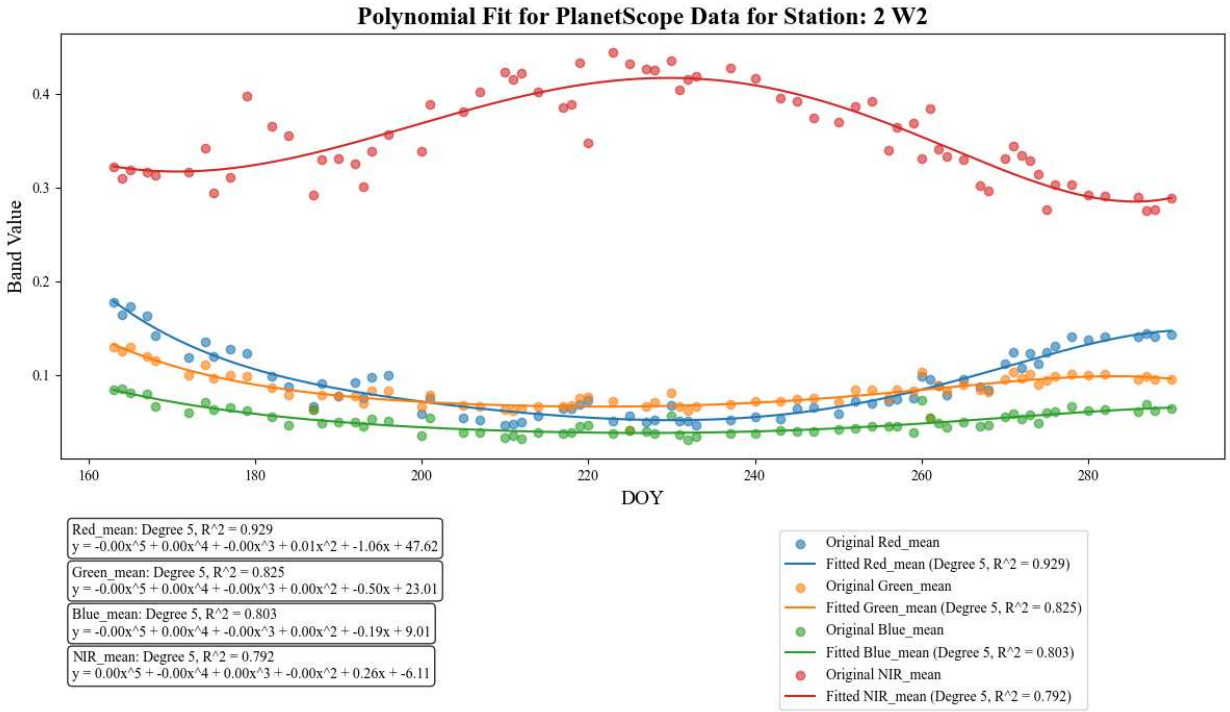
Polynomial Fit for PlanetScope Data for Station: 2 W2
Band Value
DOY
Red_mean: Degree 5, R^2 = 0.929
y = -0.00x^5 + 0.00x^4 + -0.00x^3 + 0.01x^2 + -1.06x + 47.62
Green_mean: Degree 5, R^2 = 0.825
y = -0.00x^5 + 0.00x^4 + -0.00x^3 + 0.00x^2 + -0.50x + 23.01
Blue_mean: Degree 5, R^2 = 0.803
y = -0.00x^5 + 0.00x^4 + -0.00x^3 + 0.00x^2 + -0.19x + 9.01
NIR_mean: Degree 5, R^2 = 0.792
y = 0.00x^5 + -0.00x^4 + 0.00x^3 + -0.00x^2 + 0.26x + -6.11
Original Red_mean
Fitted Red_mean (Degree 5, R^2 = 0.929)
Original Green_mean
Fitted Green_mean (Degree 5, R^2 = 0.825)
Original Blue_mean
Fitted Blue_mean (Degree 5, R^2 = 0.803)
Original NIR_mean
Fitted NIR_mean (Degree 5, R^2 = 0.792)

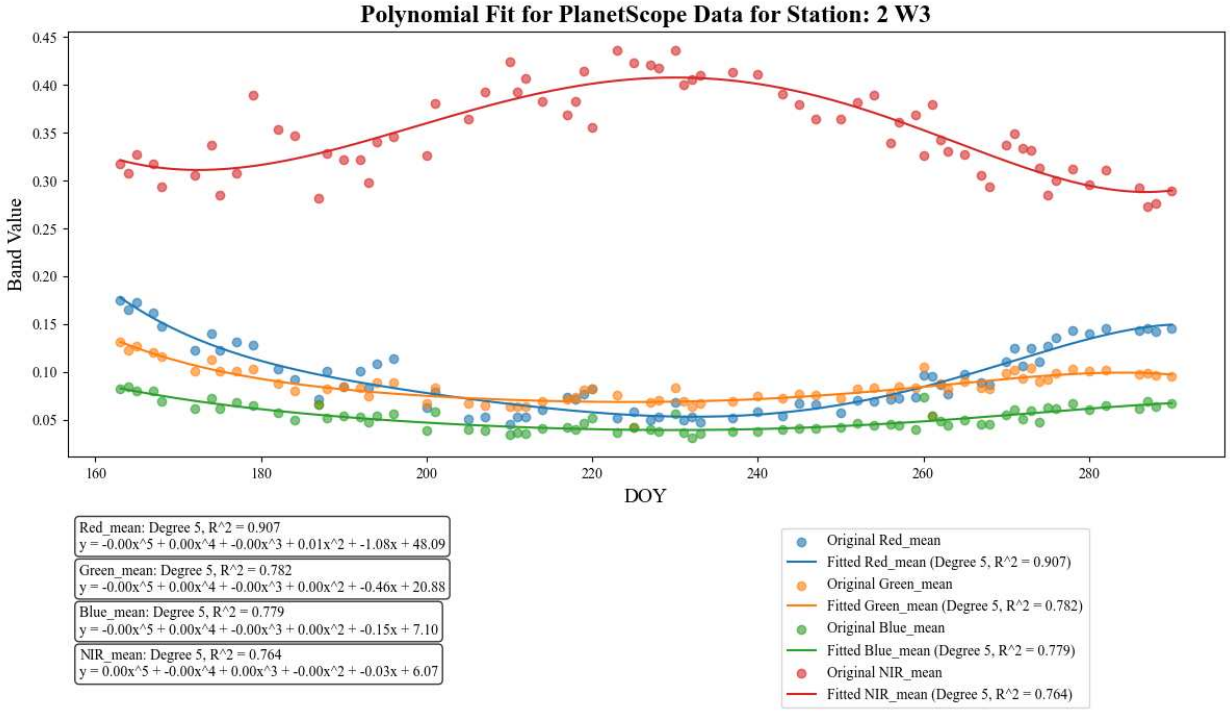
Polynomial Fit for PlanetScope Data for Station: 2 W3
Band Value
DOY
Red_mean: Degree 5, R^2 = 0.907
y = -0.00x^5 + 0.00x^4 + -0.00x^3 + 0.01x^2 + -1.08x + 48.09
Green_mean: Degree 5, R^2 = 0.782
y = -0.00x^5 + 0.00x^4 + -0.00x^3 + 0.00x^2 + -0.46x + 20.88
Blue_mean: Degree 5, R^2 = 0.779
y = -0.00x^5 + 0.00x^4 + -0.00x^3 + 0.00x^2 + -0.15x + 7.10
NIR_mean: Degree 5, R^2 = 0.764
y = 0.00x^5 + -0.00x^4 + 0.00x^3 + -0.00x^2 + -0.03x + 6.07
Original Red_mean
Fitted Red_mean (Degree 5, R^2 = 0.907)
Original Green_mean
Fitted Green_mean (Degree 5, R^2 = 0.782)
Original Blue_mean
Fitted Blue_mean (Degree 5, R^2 = 0.779)
Original NIR_mean
Fitted NIR_mean (Degree 5, R^2 = 0.764)

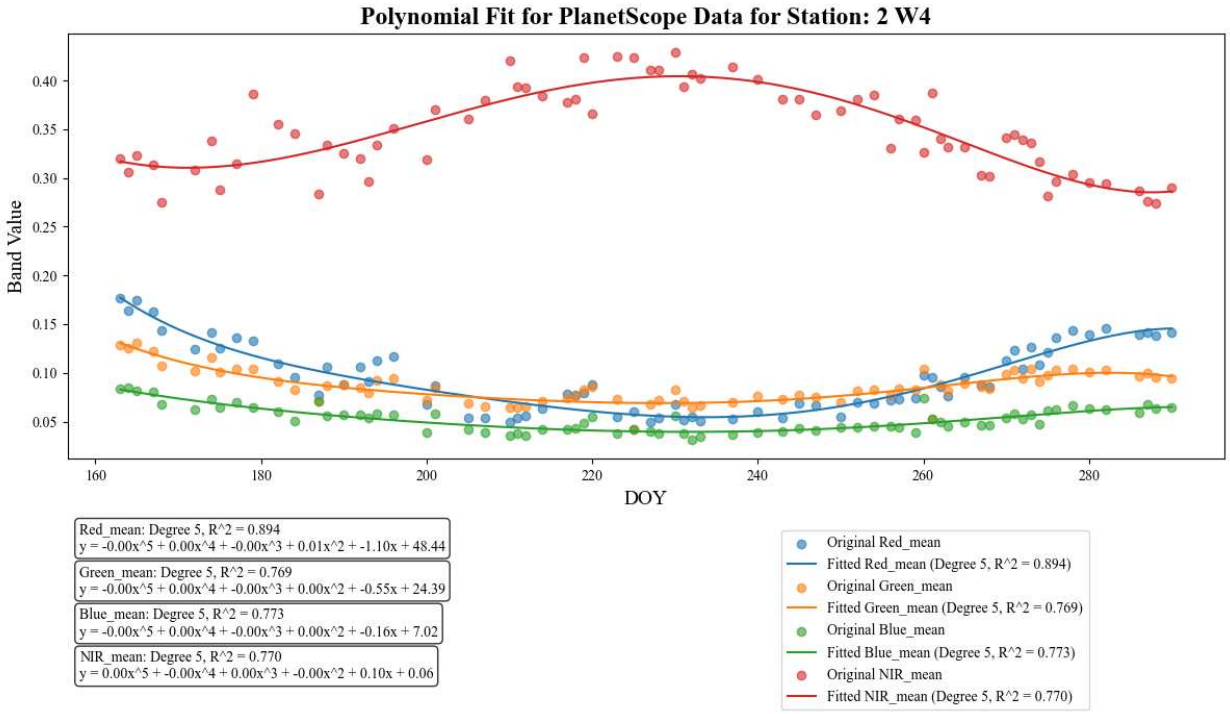
Polynomial Fit for PlanetScope Data for Station: 2 W4
Band Value
DOY
Red_mean: Degree 5, R^2 = 0.894
y = -0.00x^5 + 0.00x^4 + -0.00x^3 + 0.01x^2 + -1.10x + 48.44
Green_mean: Degree 5, R^2 = 0.769
y = -0.00x^5 + 0.00x^4 + -0.00x^3 + 0.00x^2 + -0.55x + 24.39
Blue_mean: Degree 5, R^2 = 0.773
y = -0.00x^5 + 0.00x^4 + -0.00x^3 + 0.00x^2 + -0.16x + 7.02
NIR_mean: Degree 5, R^2 = 0.770
y = 0.00x^5 + -0.00x^4 + 0.00x^3 + -0.00x^2 + 0.10x + 0.06
Original Red_mean
Fitted Red_mean (Degree 5, R^2 = 0.894)
Original Green_mean
Fitted Green_mean (Degree 5, R^2 = 0.769)
Original Blue_mean
Fitted Blue_mean (Degree 5, R^2 = 0.773)
Original NIR_mean
Fitted NIR_mean (Degree 5, R^2 = 0.770)

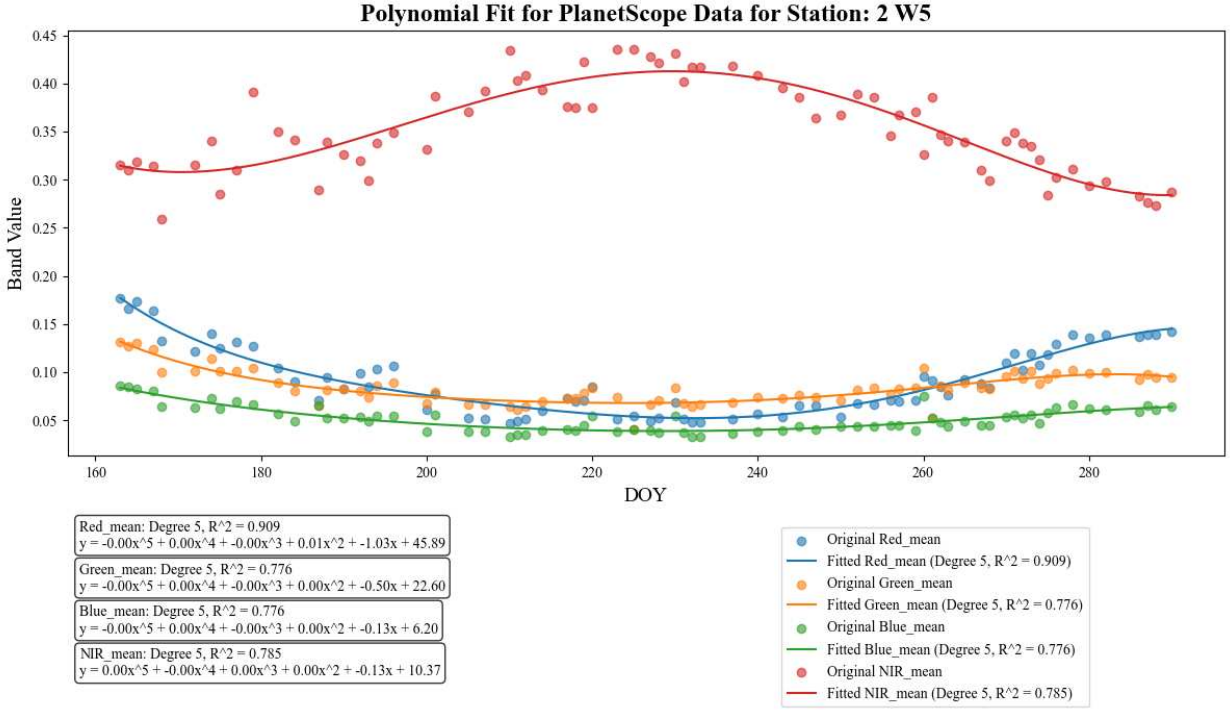
Polynomial Fit for PlanetScope Data for Station: 2 W5
Band Value
DOY
Red_mean: Degree 5, R^2 = 0.909
y = -0.00x^5 + 0.00x^4 + -0.00x^3 + 0.01x^2 + -1.03x + 45.89
Green_mean: Degree 5, R^2 = 0.776
y = -0.00x^5 + 0.00x^4 + -0.00x^3 + 0.00x^2 + -0.50x + 22.60
Blue_mean: Degree 5, R^2 = 0.776
y = -0.00x^5 + 0.00x^4 + -0.00x^3 + 0.00x^2 + -0.13x + 6.20
NIR_mean: Degree 5, R^2 = 0.785
y = 0.00x^5 + -0.00x^4 + 0.00x^3 + 0.00x^2 + -0.13x + 10.37
Original Red_mean
Fitted Red_mean (Degree 5, R^2 = 0.909)
Original Green_mean
Fitted Green_mean (Degree 5, R^2 = 0.776)
Original Blue_mean
Fitted Blue_mean (Degree 5, R^2 = 0.776)
Original NIR_mean
Fitted NIR_mean (Degree 5, R^2 = 0.785)

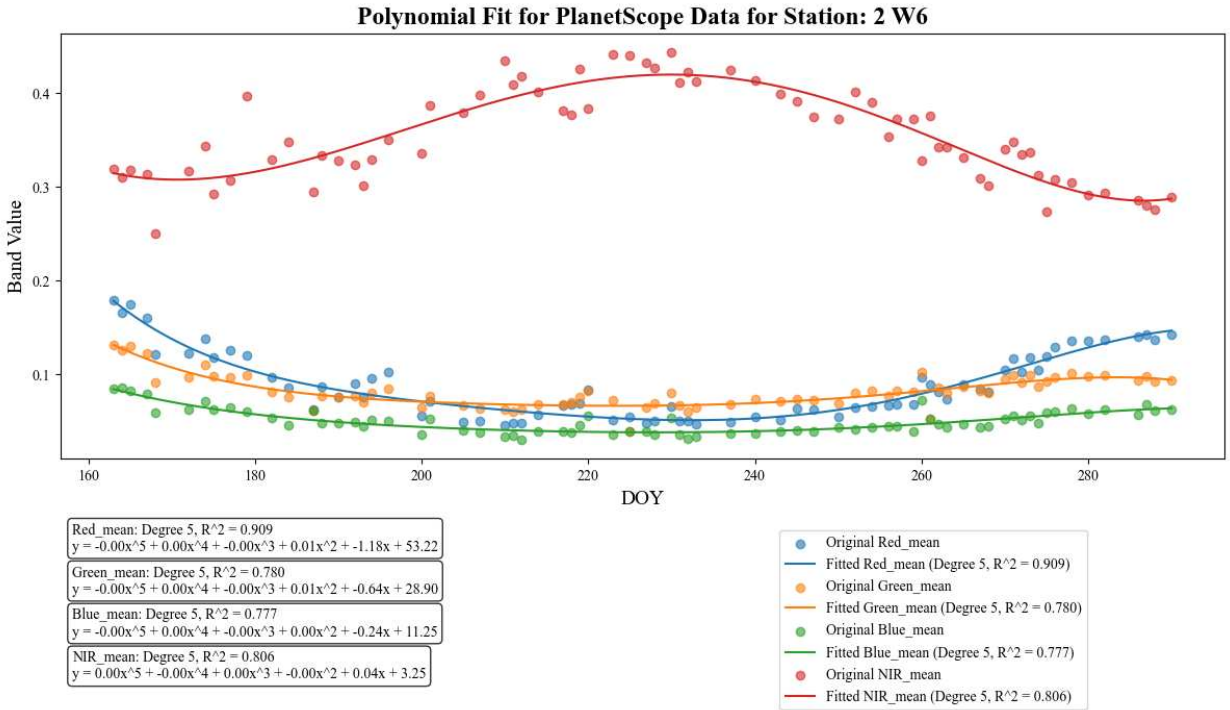
Polynomial Fit for PlanetScope Data for Station: 2 W6
Band Value
DOY
Red_mean: Degree 5, R^2 = 0.909
y = -0.00x^5 + 0.00x^4 + -0.00x^3 + 0.01x^2 + -1.18x + 53.22
Green_mean: Degree 5, R^2 = 0.780
y = -0.00x^5 + 0.00x^4 + -0.00x^3 + 0.01x^2 + -0.64x + 28.90
Blue_mean: Degree 5, R^2 = 0.777
y = -0.00x^5 + 0.00x^4 + -0.00x^3 + 0.00x^2 + -0.24x + 11.25
NIR_mean: Degree 5, R^2 = 0.806
y = 0.00x^5 + -0.00x^4 + 0.00x^3 + -0.00x^2 + 0.04x + 3.25
Original Red_mean
Fitted Red_mean (Degree 5, R^2 = 0.909)
Original Green_mean
Fitted Green_mean (Degree 5, R^2 = 0.780)
Original Blue_mean
Fitted Blue_mean (Degree 5, R^2 = 0.777)
Original NIR_mean
Fitted NIR_mean (Degree 5, R^2 = 0.806)

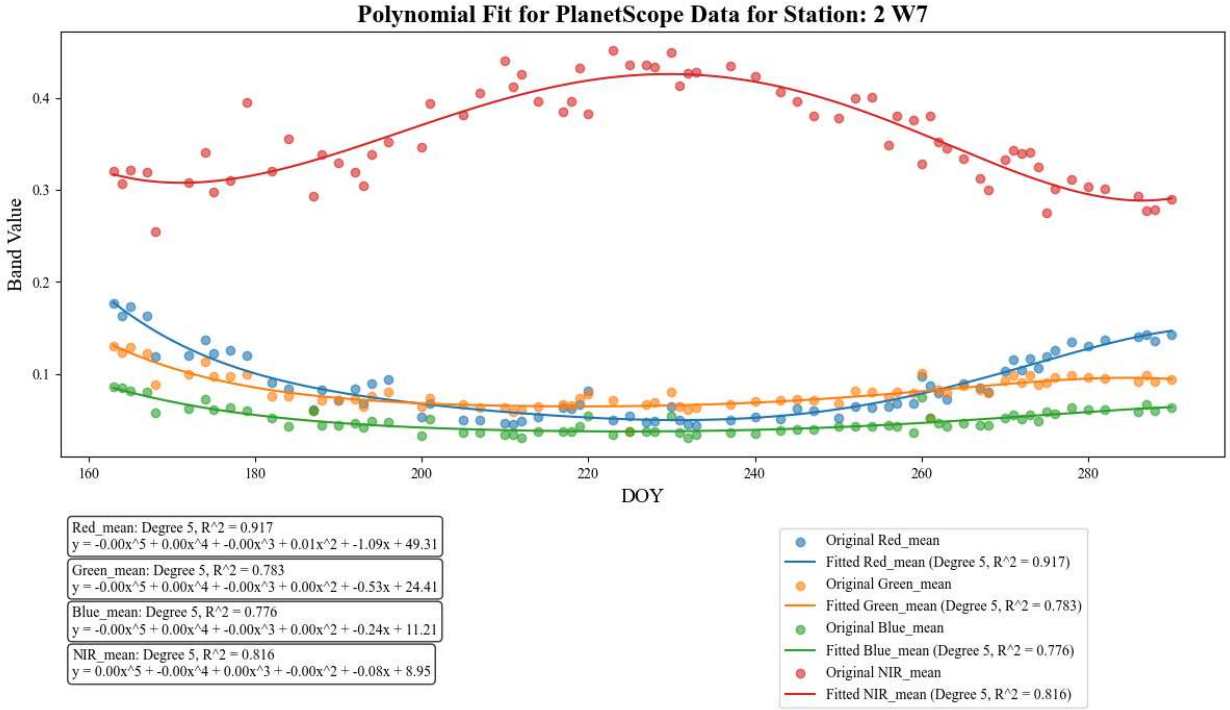
Polynomial Fit for PlanetScope Data for Station: 2 W7
Band Value
DOY
Red_mean: Degree 5, R^2 = 0.917
y = -0.00x^5 + 0.00x^4 + -0.00x^3 + 0.01x^2 + -1.09x + 49.31
Green_mean: Degree 5, R^2 = 0.783
y = -0.00x^5 + 0.00x^4 + -0.00x^3 + 0.00x^2 + -0.53x + 24.41
Blue_mean: Degree 5, R^2 = 0.776
y = -0.00x^5 + 0.00x^4 + -0.00x^3 + 0.00x^2 + -0.24x + 11.21
NIR_mean: Degree 5, R^2 = 0.816
y = 0.00x^5 + -0.00x^4 + 0.00x^3 + -0.00x^2 + -0.08x + 8.95
Original Red_mean
Fitted Red_mean (Degree 5, R^2 = 0.917)
Original Green_mean
Fitted Green_mean (Degree 5, R^2 = 0.783)
Original Blue_mean
Fitted Blue_mean (Degree 5, R^2 = 0.776)
Original NIR_mean
Fitted NIR_mean (Degree 5, R^2 = 0.816)

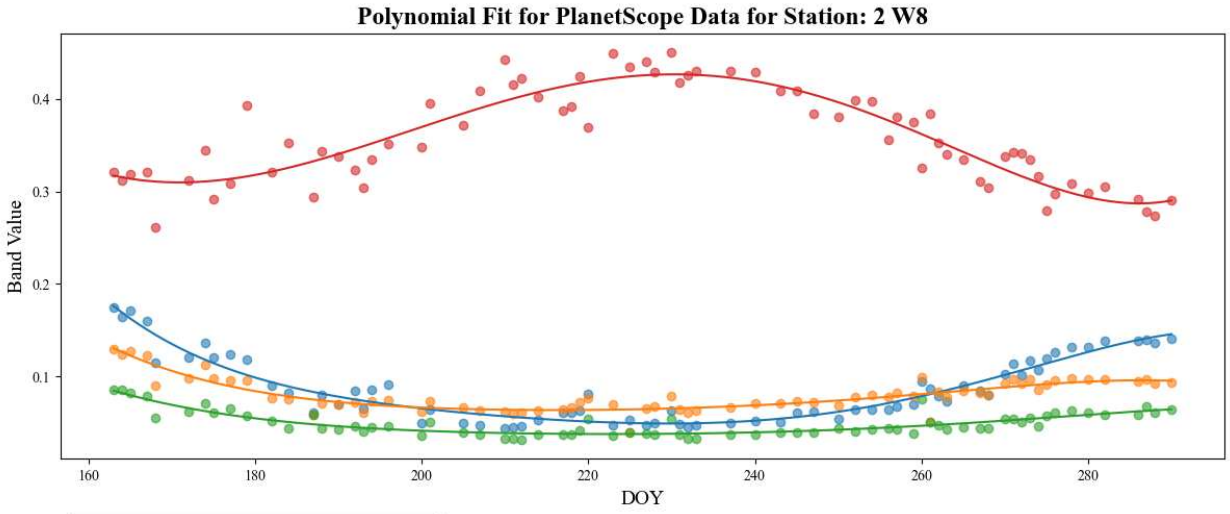

Red_mean: Degree 5, R^2 = 0.919
y = -0.00x^5 + 0.00x^4 + -0.00x^3 + 0.01x^2 + -1.04x + 47.00

Green_mean: Degree 5, R^2 = 0.806
y = -0.00x^5 + 0.00x^4 + -0.00x^3 + 0.00x^2 + -0.47x + 21.88

Blue_mean: Degree 5, R^2 = 0.772
y = -0.00x^5 + 0.00x^4 + -0.00x^3 + 0.00x^2 + -0.23x + 10.89

NIR_mean: Degree 5, R^2 = 0.822
y = 0.00x^5 + -0.00x^4 + 0.00x^3 + -0.00x^2 + 0.14x + -0.73

Original Red_mean
Fitted Red_mean (Degree 5, R^2 = 0.919)
Original Green_mean
Fitted Green_mean (Degree 5, R^2 = 0.806)
Original Blue_mean
Fitted Blue_mean (Degree 5, R^2 = 0.772)
Original NIR_mean
Fitted NIR_mean (Degree 5, R^2 = 0.822)

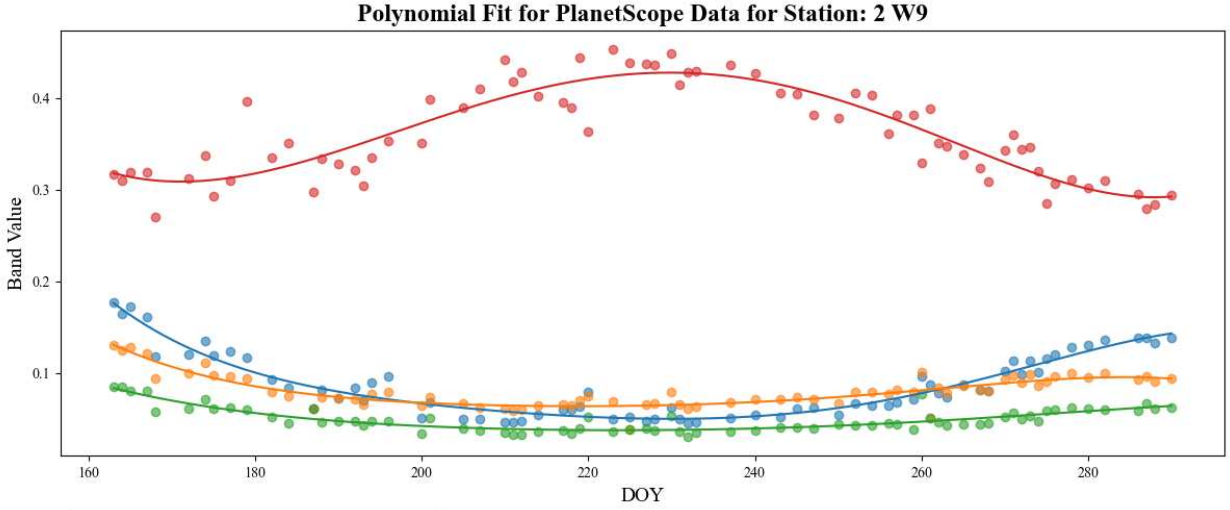

Red_mean: Degree 5, R^2 = 0.920
y = -0.00x^5 + 0.00x^4 + -0.00x^3 + 0.01x^2 + -0.97x + 43.99

Green_mean: Degree 5, R^2 = 0.815
y = -0.00x^5 + 0.00x^4 + -0.00x^3 + 0.00x^2 + -0.50x + 22.94

Blue_mean: Degree 5, R^2 = 0.775
y = -0.00x^5 + 0.00x^4 + -0.00x^3 + 0.00x^2 + -0.16x + 7.87

NIR_mean: Degree 5, R^2 = 0.809
y = 0.00x^5 + -0.00x^4 + 0.00x^3 + 0.00x^2 + -0.20x + 14.01

Original Red_mean
Fitted Red_mean (Degree 5, R^2 = 0.920)
Original Green_mean
Fitted Green_mean (Degree 5, R^2 = 0.815)
Original Blue_mean
Fitted Blue_mean (Degree 5, R^2 = 0.775)
Original NIR_mean
Fitted NIR_mean (Degree 5, R^2 = 0.809)

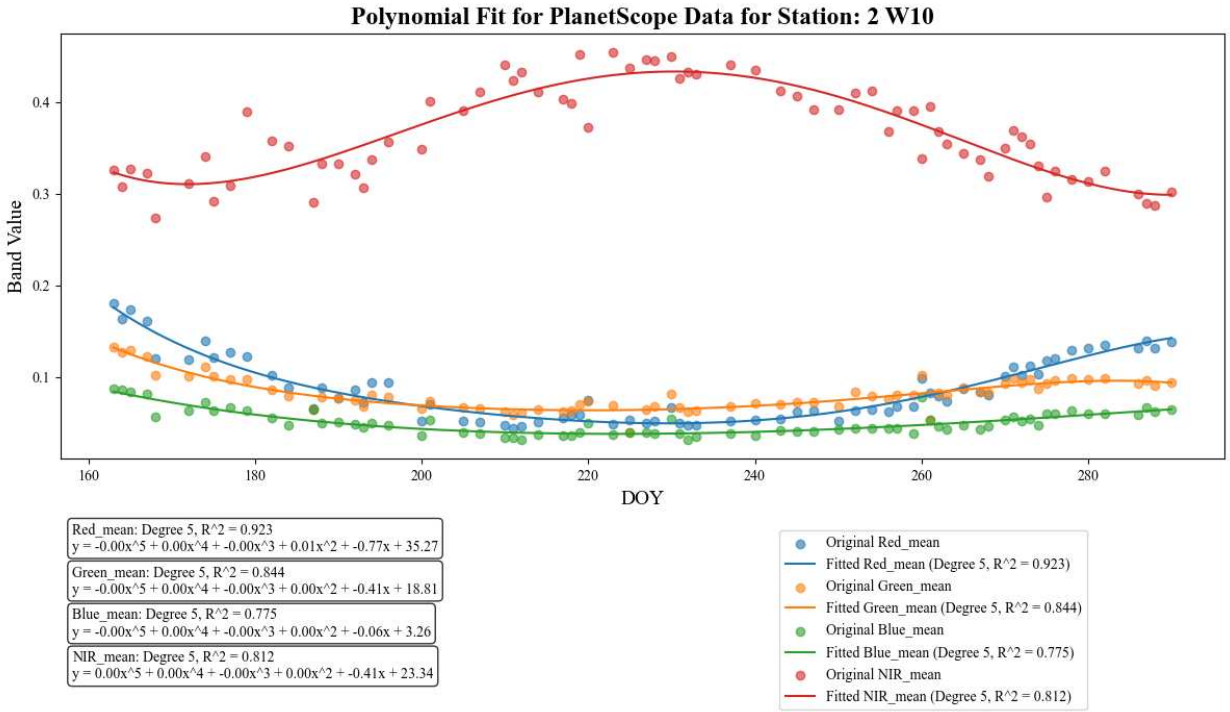
Polynomial Fit for PlanetScope Data for Station: 2 W10
Band Value
DOY
0.1
0.2
0.3
0.4
160
180
200
220
240
260
280
Red_mean: Degree 5, R^2 = 0.923
y = -0.00x^5 + 0.00x^4 + -0.00x^3 + 0.01x^2 + -0.77x + 35.27
Green_mean: Degree 5, R^2 = 0.844
y = -0.00x^5 + 0.00x^4 + -0.00x^3 + 0.00x^2 + -0.41x + 18.81
Blue_mean: Degree 5, R^2 = 0.775
y = -0.00x^5 + 0.00x^4 + -0.00x^3 + 0.00x^2 + -0.06x + 3.26
NIR_mean: Degree 5, R^2 = 0.812
y = 0.00x^5 + 0.00x^4 + -0.00x^3 + 0.00x^2 + -0.41x + 23.34
Original Red_mean
Fitted Red_mean (Degree 5, R^2 = 0.923)
Original Green_mean
Fitted Green_mean (Degree 5, R^2 = 0.844)
Original Blue_mean
Fitted Blue_mean (Degree 5, R^2 = 0.775)
Original NIR_mean
Fitted NIR_mean (Degree 5, R^2 = 0.812)

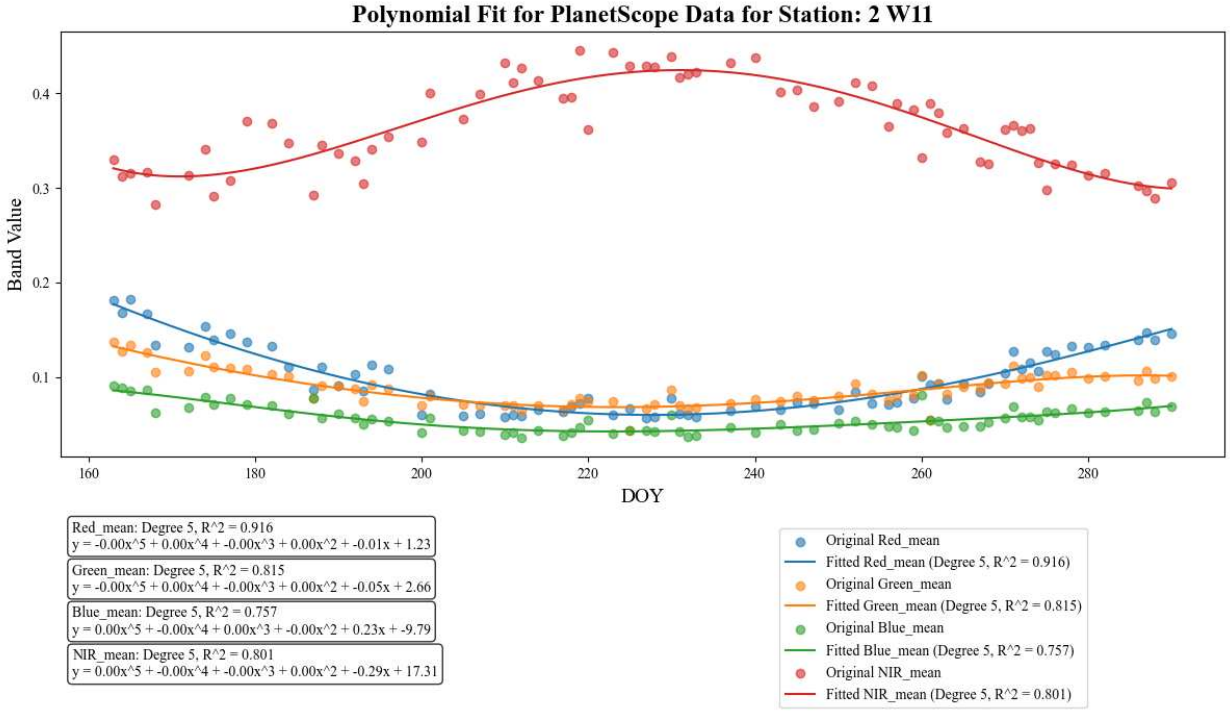
Polynomial Fit for PlanetScope Data for Station: 2 W11
Band Value
DOY
0.1
0.2
0.3
0.4
160
180
200
220
240
260
280
Red_mean: Degree 5, R^2 = 0.916
y = -0.00x^5 + 0.00x^4 + -0.00x^3 + 0.00x^2 + -0.01x + 1.23
Green_mean: Degree 5, R^2 = 0.815
y = -0.00x^5 + 0.00x^4 + -0.00x^3 + 0.00x^2 + -0.05x + 2.66
Blue_mean: Degree 5, R^2 = 0.757
y = 0.00x^5 + -0.00x^4 + 0.00x^3 + -0.00x^2 + 0.23x + -9.79
NIR_mean: Degree 5, R^2 = 0.801
y = 0.00x^5 + -0.00x^4 + -0.00x^3 + 0.00x^2 + -0.29x + 17.31
Original Red_mean
Fitted Red_mean (Degree 5, R^2 = 0.916)
Original Green_mean
Fitted Green_mean (Degree 5, R^2 = 0.815)
Original Blue_mean
Fitted Blue_mean (Degree 5, R^2 = 0.757)
Original NIR_mean
Fitted NIR_mean (Degree 5, R^2 = 0.801)

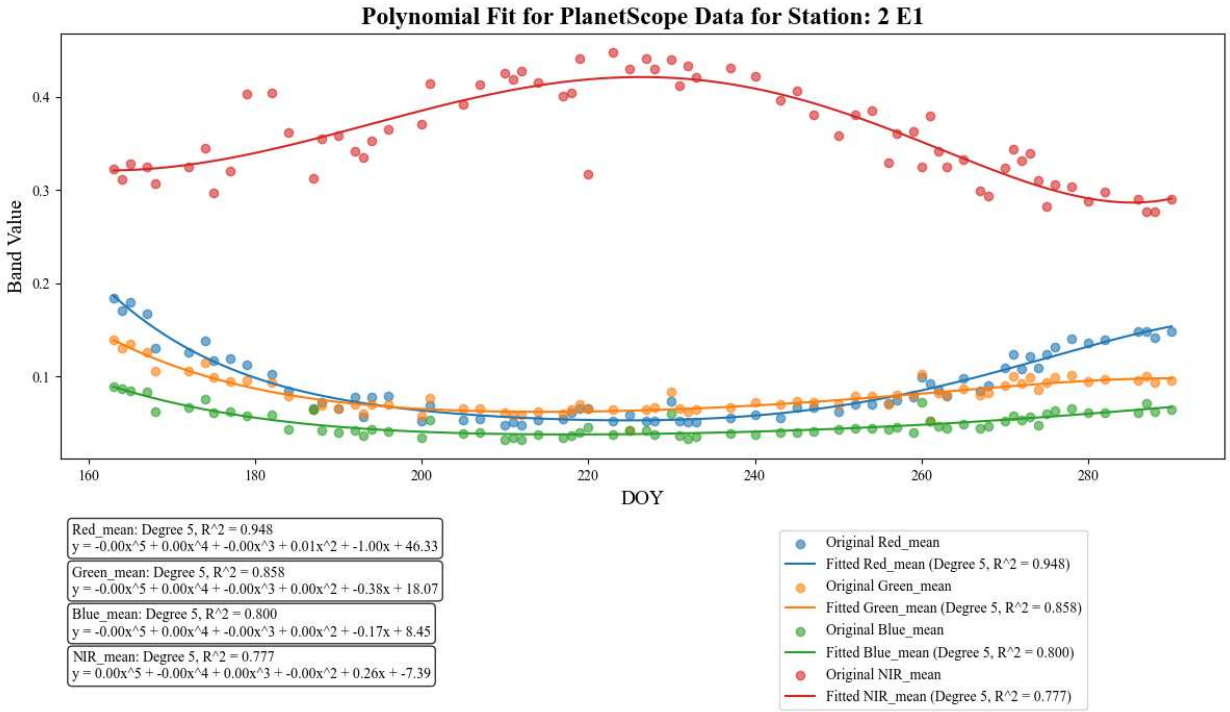
Polynomial Fit for PlanetScope Data for Station: 2 E1
Band Value
DOY
0.1
0.2
0.3
0.4
160
180
200
220
240
260
280
Red_mean: Degree 5, R^2 = 0.948
y = -0.00x^5 + 0.00x^4 + -0.00x^3 + 0.01x^2 + -1.00x + 46.33
Green_mean: Degree 5, R^2 = 0.858
y = -0.00x^5 + 0.00x^4 + -0.00x^3 + 0.00x^2 + -0.38x + 18.07
Blue_mean: Degree 5, R^2 = 0.800
y = -0.00x^5 + 0.00x^4 + -0.00x^3 + 0.00x^2 + -0.17x + 8.45
NIR_mean: Degree 5, R^2 = 0.777
y = 0.00x^5 + -0.00x^4 + 0.00x^3 + -0.00x^2 + 0.26x + -7.39
Original Red_mean
Fitted Red_mean (Degree 5, R^2 = 0.948)
Original Green_mean
Fitted Green_mean (Degree 5, R^2 = 0.858)
Original Blue_mean
Fitted Blue_mean (Degree 5, R^2 = 0.800)
Original NIR_mean
Fitted NIR_mean (Degree 5, R^2 = 0.777)

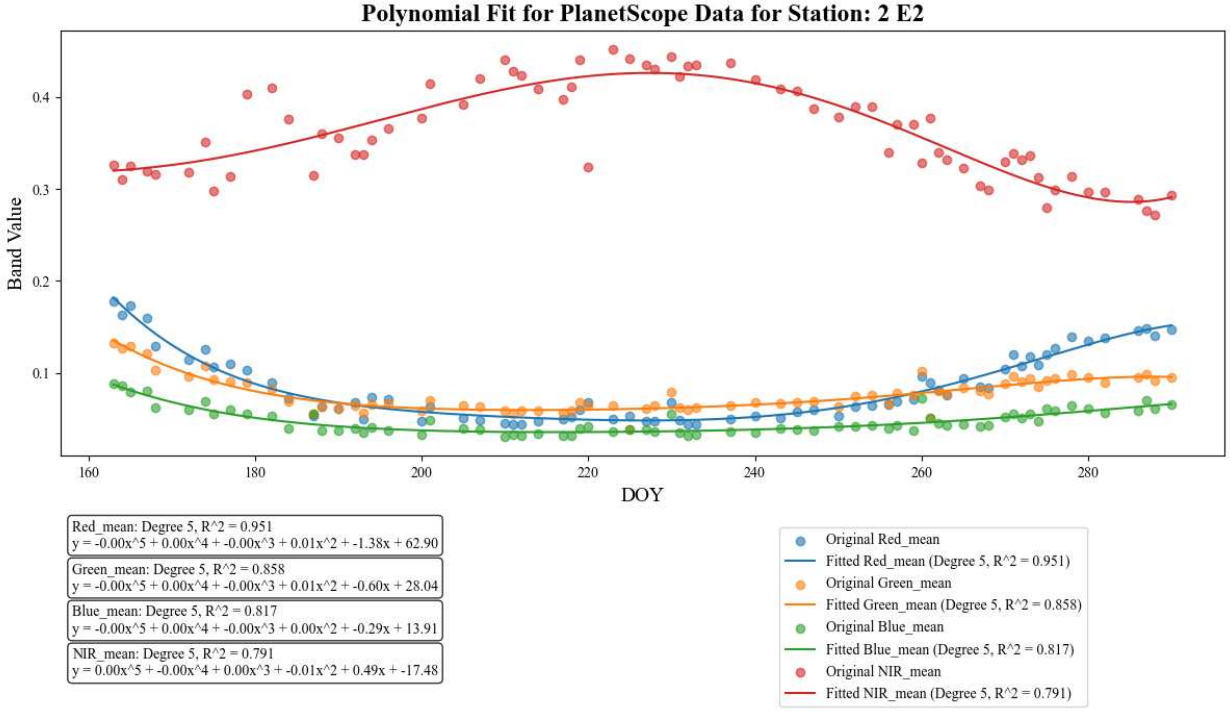
Polynomial Fit for PlanetScope Data for Station: 2 E2
Band Value
DOY
0.1
0.2
0.3
0.4
160
180
200
220
240
260
280
Red_mean: Degree 5, R^2 = 0.951
y = -0.00x^5 + 0.00x^4 + -0.00x^3 + 0.01x^2 + -1.38x + 62.90
Green_mean: Degree 5, R^2 = 0.858
y = -0.00x^5 + 0.00x^4 + -0.00x^3 + 0.01x^2 + -0.60x + 28.04
Blue_mean: Degree 5, R^2 = 0.817
y = -0.00x^5 + 0.00x^4 + -0.00x^3 + 0.00x^2 + -0.29x + 13.91
NIR_mean: Degree 5, R^2 = 0.791
y = 0.00x^5 + -0.00x^4 + 0.00x^3 + -0.01x^2 + 0.49x + -17.48
Original Red_mean
Fitted Red_mean (Degree 5, R^2 = 0.951)
Original Green_mean
Fitted Green_mean (Degree 5, R^2 = 0.858)
Original Blue_mean
Fitted Blue_mean (Degree 5, R^2 = 0.817)
Original NIR_mean
Fitted NIR_mean (Degree 5, R^2 = 0.791)

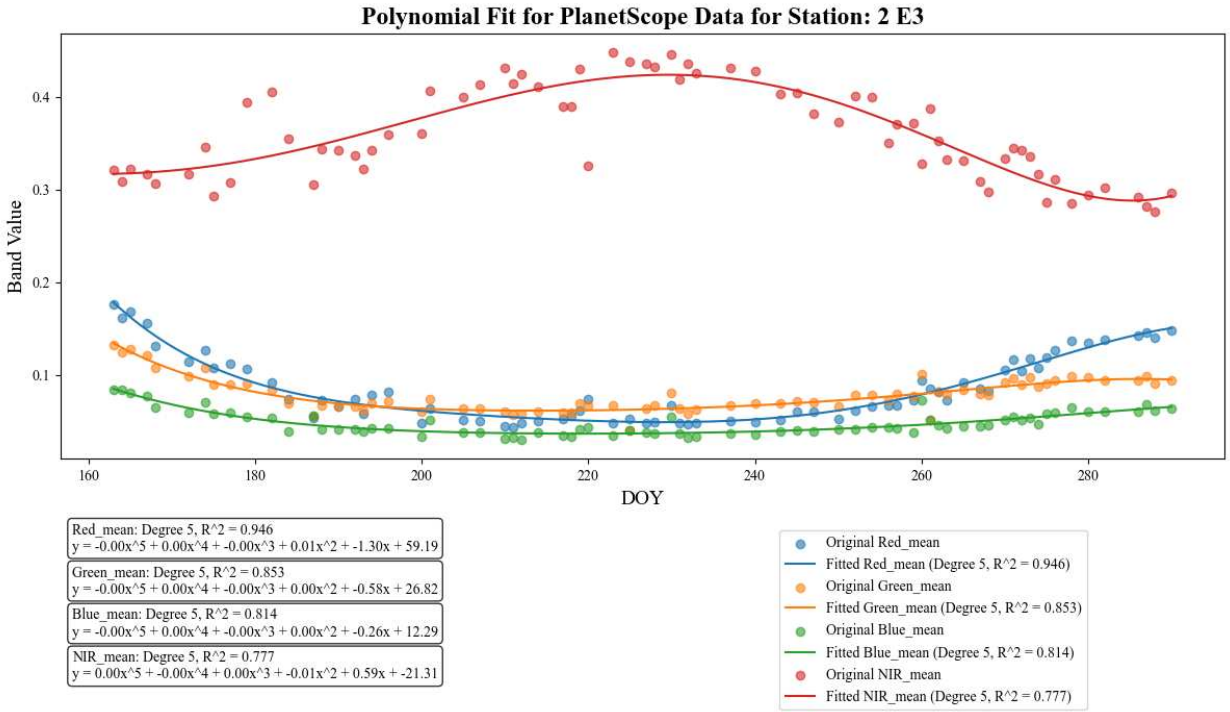
Polynomial Fit for PlanetScope Data for Station: 2 E3
Band Value
DOY
0.1
0.2
0.3
0.4
160
180
200
220
240
260
280
Red_mean: Degree 5, R^2 = 0.946
y = -0.00x^5 + 0.00x^4 + -0.00x^3 + 0.01x^2 + -1.30x + 59.19
Green_mean: Degree 5, R^2 = 0.853
y = -0.00x^5 + 0.00x^4 + -0.00x^3 + 0.00x^2 + -0.58x + 26.82
Blue_mean: Degree 5, R^2 = 0.814
y = -0.00x^5 + 0.00x^4 + -0.00x^3 + 0.00x^2 + -0.26x + 12.29
NIR_mean: Degree 5, R^2 = 0.777
y = 0.00x^5 + -0.00x^4 + 0.00x^3 + -0.01x^2 + 0.59x + -21.31
Original Red_mean
Fitted Red_mean (Degree 5, R^2 = 0.946)
Original Green_mean
Fitted Green_mean (Degree 5, R^2 = 0.853)
Original Blue_mean
Fitted Blue_mean (Degree 5, R^2 = 0.814)
Original NIR_mean
Fitted NIR_mean (Degree 5, R^2 = 0.777)

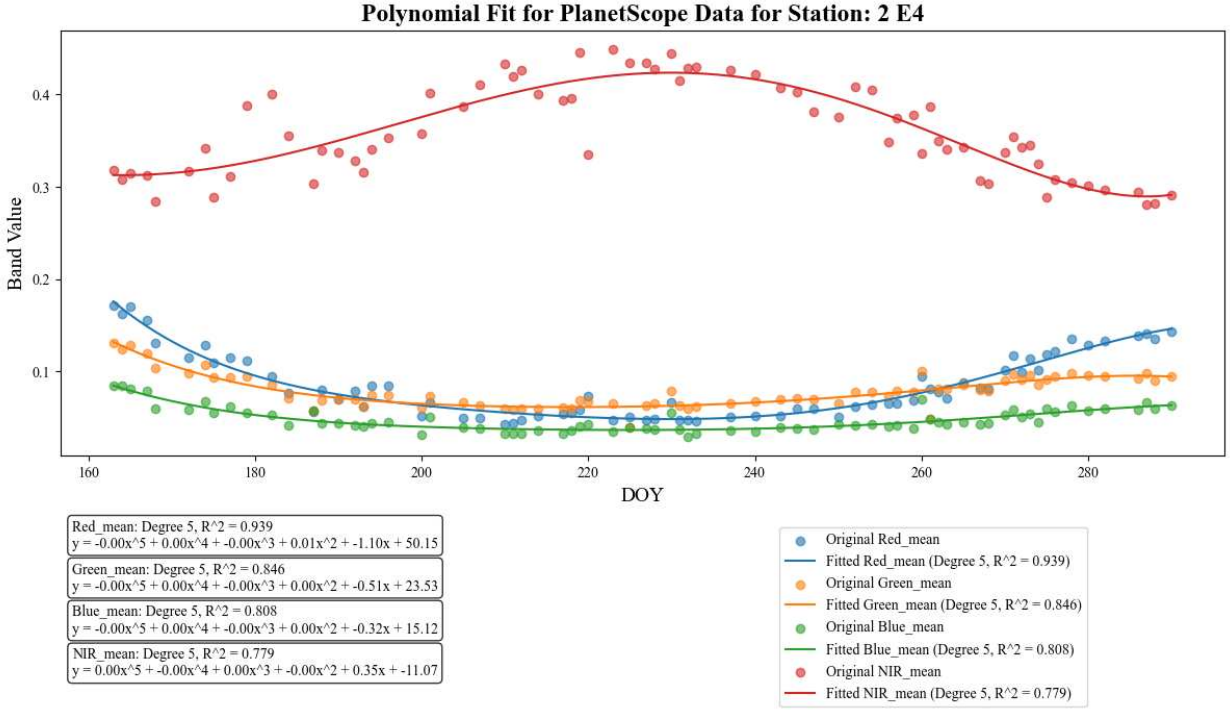
Polynomial Fit for PlanetScope Data for Station: 2 E4
Band Value
DOY
0.1
0.2
0.3
0.4
160
180
200
220
240
260
280
Red_mean: Degree 5, R^2 = 0.939
y = -0.00x^5 + 0.00x^4 + -0.00x^3 + 0.01x^2 + -1.10x + 50.15
Green_mean: Degree 5, R^2 = 0.846
y = -0.00x^5 + 0.00x^4 + -0.00x^3 + 0.00x^2 + -0.51x + 23.53
Blue_mean: Degree 5, R^2 = 0.808
y = -0.00x^5 + 0.00x^4 + -0.00x^3 + 0.00x^2 + -0.32x + 15.12
NIR_mean: Degree 5, R^2 = 0.779
y = 0.00x^5 + -0.00x^4 + 0.00x^3 + -0.00x^2 + 0.35x + -11.07
Original Red_mean
Fitted Red_mean (Degree 5, R^2 = 0.939)
Original Green_mean
Fitted Green_mean (Degree 5, R^2 = 0.846)
Original Blue_mean
Fitted Blue_mean (Degree 5, R^2 = 0.808)
Original NIR_mean
Fitted NIR_mean (Degree 5, R^2 = 0.779)

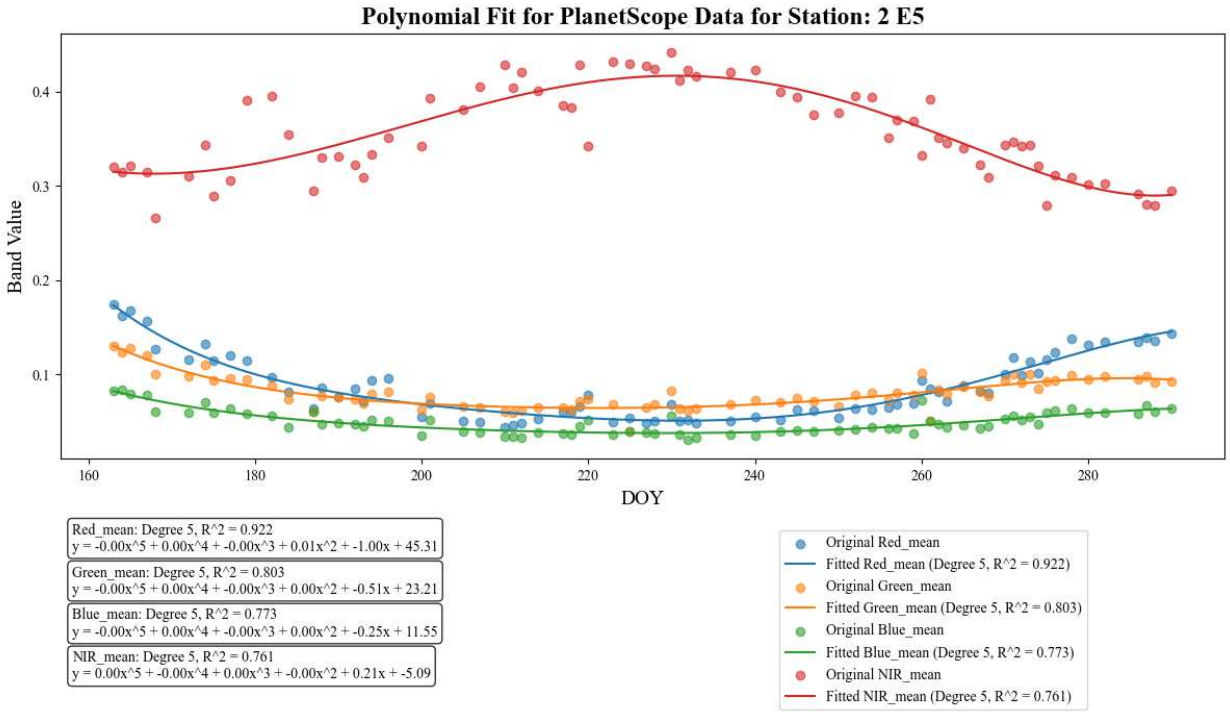
Polynomial Fit for PlanetScope Data for Station: 2 E5
Band Value
DOY
Red_mean: Degree 5, R^2 = 0.922
y = -0.00x^5 + 0.00x^4 + -0.00x^3 + 0.01x^2 + -1.00x + 45.31
Green_mean: Degree 5, R^2 = 0.803
y = -0.00x^5 + 0.00x^4 + -0.00x^3 + 0.00x^2 + -0.51x + 23.21
Blue_mean: Degree 5, R^2 = 0.773
y = -0.00x^5 + 0.00x^4 + -0.00x^3 + 0.00x^2 + -0.25x + 11.55
NIR_mean: Degree 5, R^2 = 0.761
y = 0.00x^5 + -0.00x^4 + 0.00x^3 + -0.00x^2 + 0.21x + -5.09
Original Red_mean
Fitted Red_mean (Degree 5, R^2 = 0.922)
Original Green_mean
Fitted Green_mean (Degree 5, R^2 = 0.803)
Original Blue_mean
Fitted Blue_mean (Degree 5, R^2 = 0.773)
Original NIR_mean
Fitted NIR_mean (Degree 5, R^2 = 0.761)

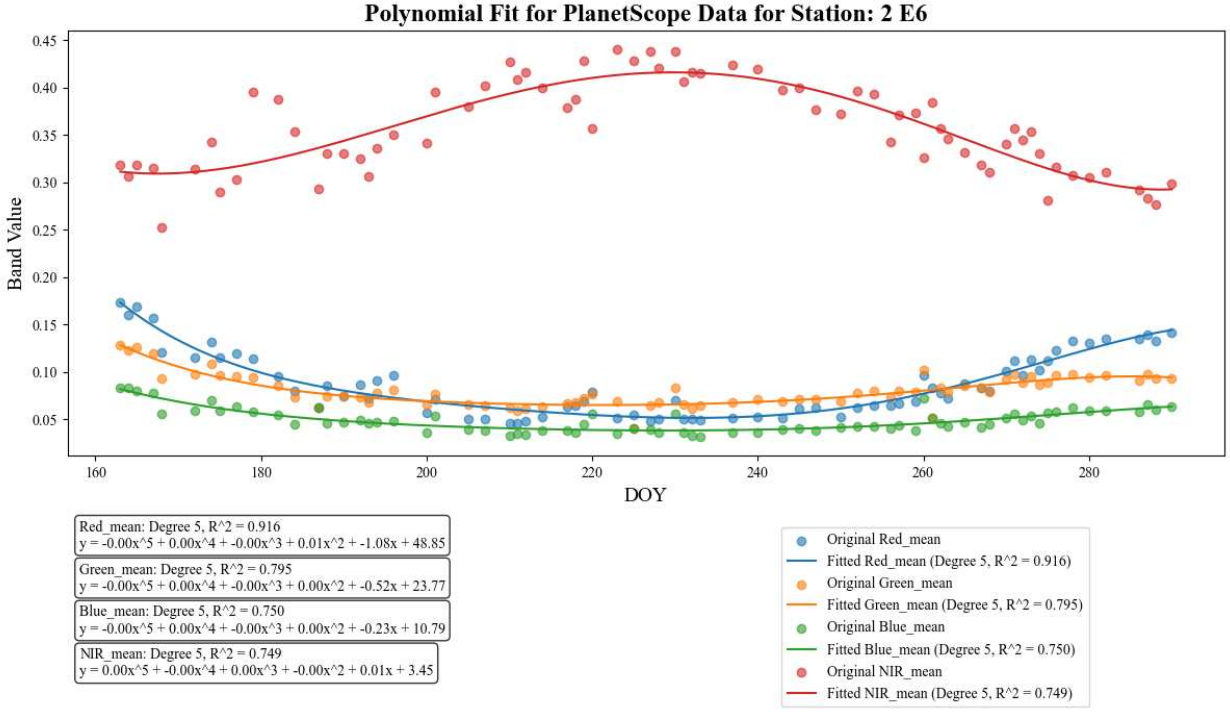
Polynomial Fit for PlanetScope Data for Station: 2 E6
Band Value
DOY
Red_mean: Degree 5, R^2 = 0.916
y = -0.00x^5 + 0.00x^4 + -0.00x^3 + 0.01x^2 + -1.08x + 48.85
Green_mean: Degree 5, R^2 = 0.795
y = -0.00x^5 + 0.00x^4 + -0.00x^3 + 0.00x^2 + -0.52x + 23.77
Blue_mean: Degree 5, R^2 = 0.750
y = -0.00x^5 + 0.00x^4 + -0.00x^3 + 0.00x^2 + -0.23x + 10.79
NIR_mean: Degree 5, R^2 = 0.749
y = 0.00x^5 + -0.00x^4 + 0.00x^3 + -0.00x^2 + 0.01x + 3.45
Original Red_mean
Fitted Red_mean (Degree 5, R^2 = 0.916)
Original Green_mean
Fitted Green_mean (Degree 5, R^2 = 0.795)
Original Blue_mean
Fitted Blue_mean (Degree 5, R^2 = 0.750)
Original NIR_mean
Fitted NIR_mean (Degree 5, R^2 = 0.749)

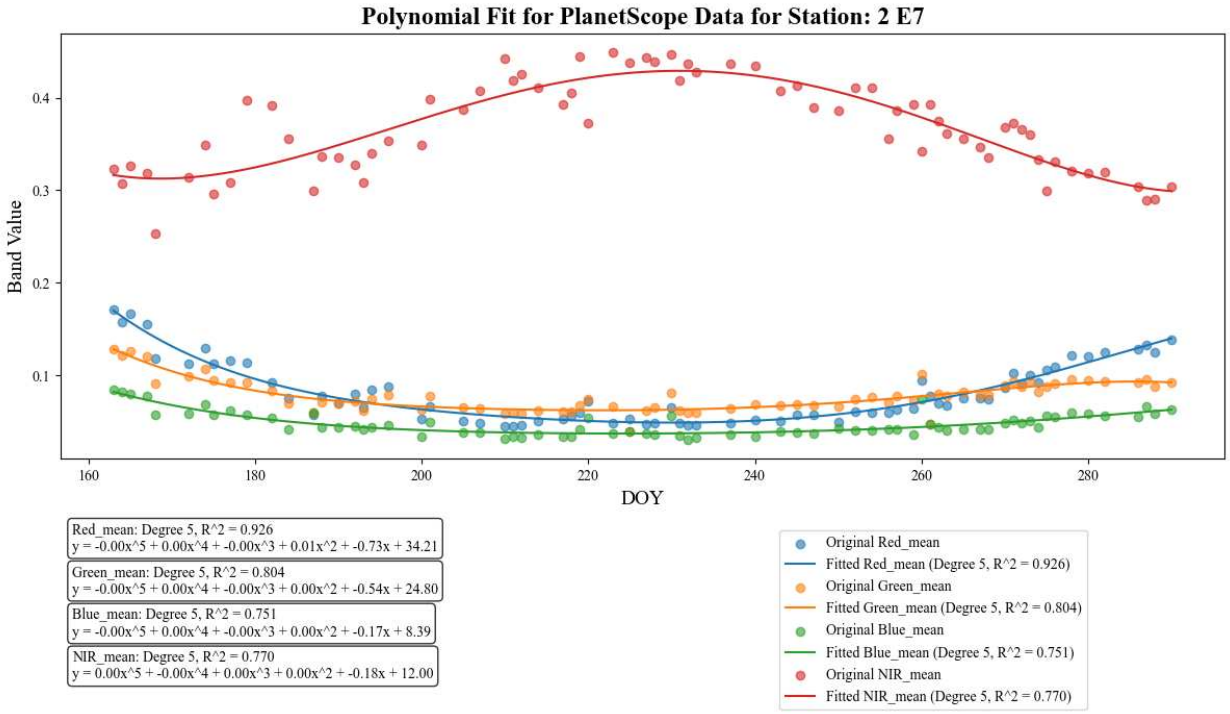
Polynomial Fit for PlanetScope Data for Station: 2 E7
Band Value
DOY
0.1
0.2
0.3
0.4
160
180
200
220
240
260
280
Red_mean: Degree 5, R^2 = 0.926
y = -0.00x^5 + 0.00x^4 + -0.00x^3 + 0.01x^2 + -0.73x + 34.21
Green_mean: Degree 5, R^2 = 0.804
y = -0.00x^5 + 0.00x^4 + -0.00x^3 + 0.00x^2 + -0.54x + 24.80
Blue_mean: Degree 5, R^2 = 0.751
y = -0.00x^5 + 0.00x^4 + -0.00x^3 + 0.00x^2 + -0.17x + 8.39
NIR_mean: Degree 5, R^2 = 0.770
y = 0.00x^5 + -0.00x^4 + 0.00x^3 + 0.00x^2 + -0.18x + 12.00
Original Red_mean
Fitted Red_mean (Degree 5, R^2 = 0.926)
Original Green_mean
Fitted Green_mean (Degree 5, R^2 = 0.804)
Original Blue_mean
Fitted Blue_mean (Degree 5, R^2 = 0.751)
Original NIR_mean
Fitted NIR_mean (Degree 5, R^2 = 0.770)

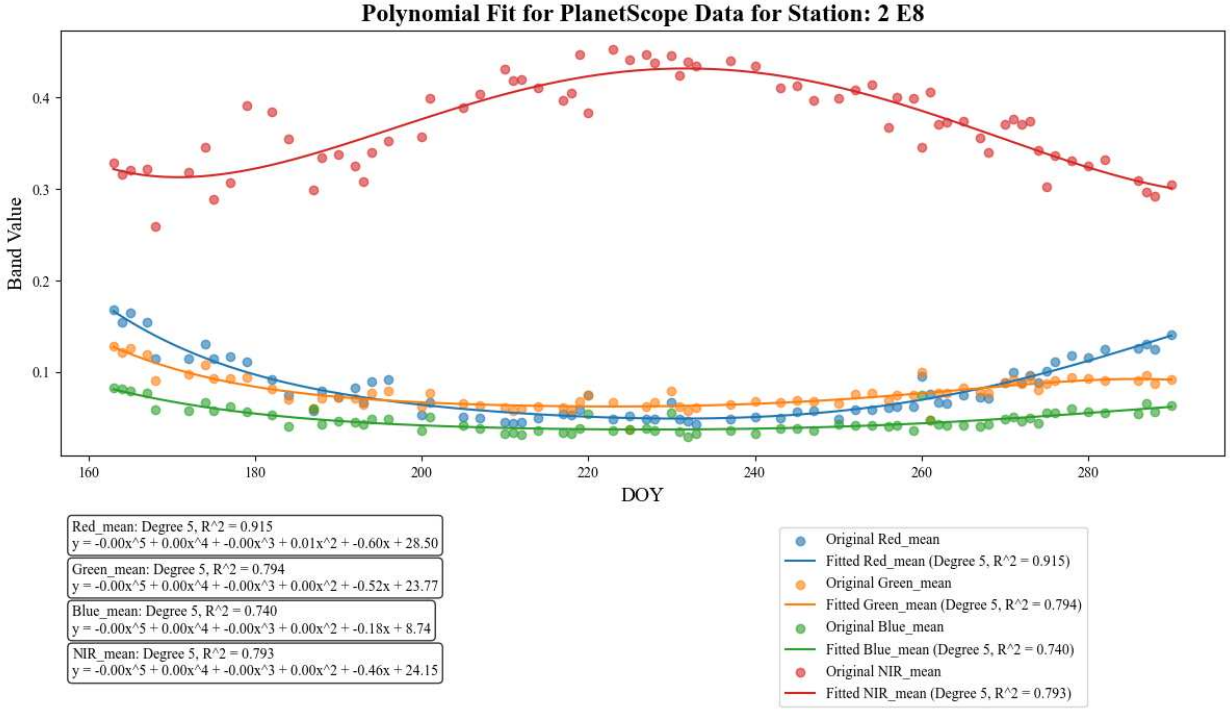
Polynomial Fit for PlanetScope Data for Station: 2 E8
Band Value
DOY
0.1
0.2
0.3
0.4
160
180
200
220
240
260
280
Red_mean: Degree 5, R^2 = 0.915
y = -0.00x^5 + 0.00x^4 + -0.00x^3 + 0.01x^2 + -0.60x + 28.50
Green_mean: Degree 5, R^2 = 0.794
y = -0.00x^5 + 0.00x^4 + -0.00x^3 + 0.00x^2 + -0.52x + 23.77
Blue_mean: Degree 5, R^2 = 0.740
y = -0.00x^5 + 0.00x^4 + -0.00x^3 + 0.00x^2 + -0.18x + 8.74
NIR_mean: Degree 5, R^2 = 0.793
y = -0.00x^5 + 0.00x^4 + -0.00x^3 + 0.00x^2 + -0.46x + 24.15
Original Red_mean
Fitted Red_mean (Degree 5, R^2 = 0.915)
Original Green_mean
Fitted Green_mean (Degree 5, R^2 = 0.794)
Original Blue_mean
Fitted Blue_mean (Degree 5, R^2 = 0.740)
Original NIR_mean
Fitted NIR_mean (Degree 5, R^2 = 0.793)

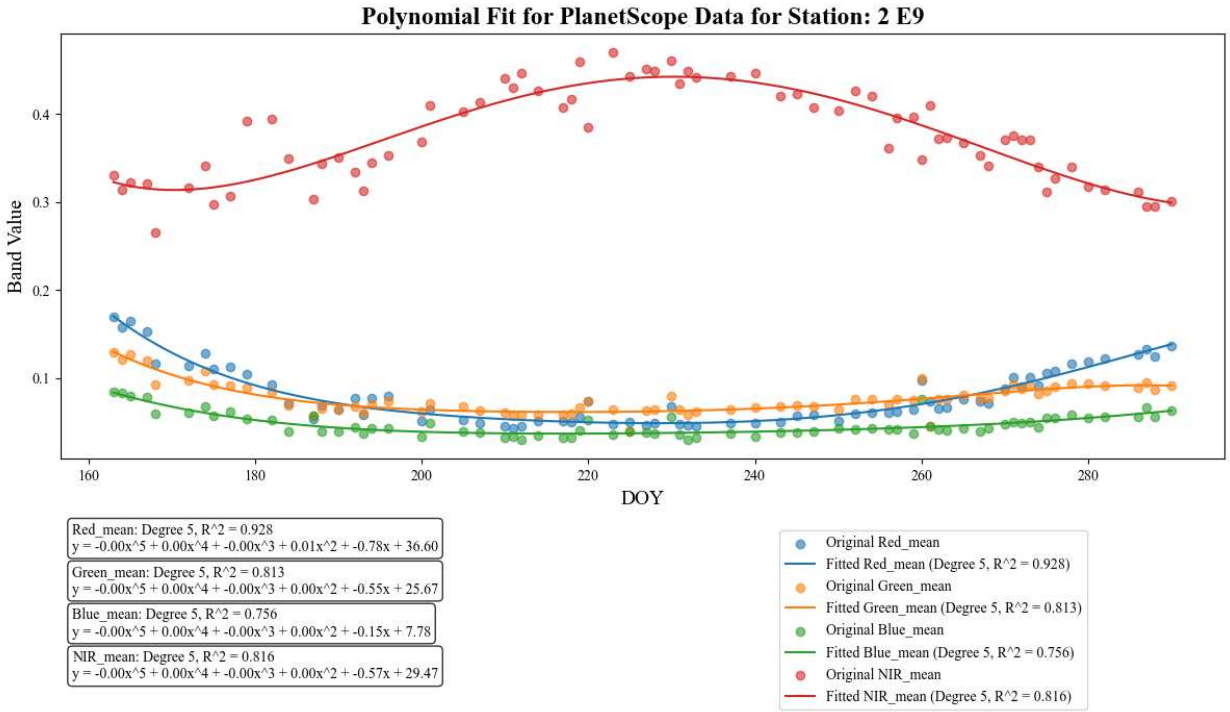
Polynomial Fit for PlanetScope Data for Station: 2 E9
Band Value
DOY
0.1
0.2
0.3
0.4
160
180
200
220
240
260
280
Red_mean: Degree 5, R^2 = 0.928
y = -0.00x^5 + 0.00x^4 + -0.00x^3 + 0.01x^2 + -0.78x + 36.60
Green_mean: Degree 5, R^2 = 0.813
y = -0.00x^5 + 0.00x^4 + -0.00x^3 + 0.00x^2 + -0.55x + 25.67
Blue_mean: Degree 5, R^2 = 0.756
y = -0.00x^5 + 0.00x^4 + -0.00x^3 + 0.00x^2 + -0.15x + 7.78
NIR_mean: Degree 5, R^2 = 0.816
y = -0.00x^5 + 0.00x^4 + -0.00x^3 + 0.00x^2 + -0.57x + 29.47
Original Red_mean
Fitted Red_mean (Degree 5, R^2 = 0.928)
Original Green_mean
Fitted Green_mean (Degree 5, R^2 = 0.813)
Original Blue_mean
Fitted Blue_mean (Degree 5, R^2 = 0.756)
Original NIR_mean
Fitted NIR_mean (Degree 5, R^2 = 0.816)

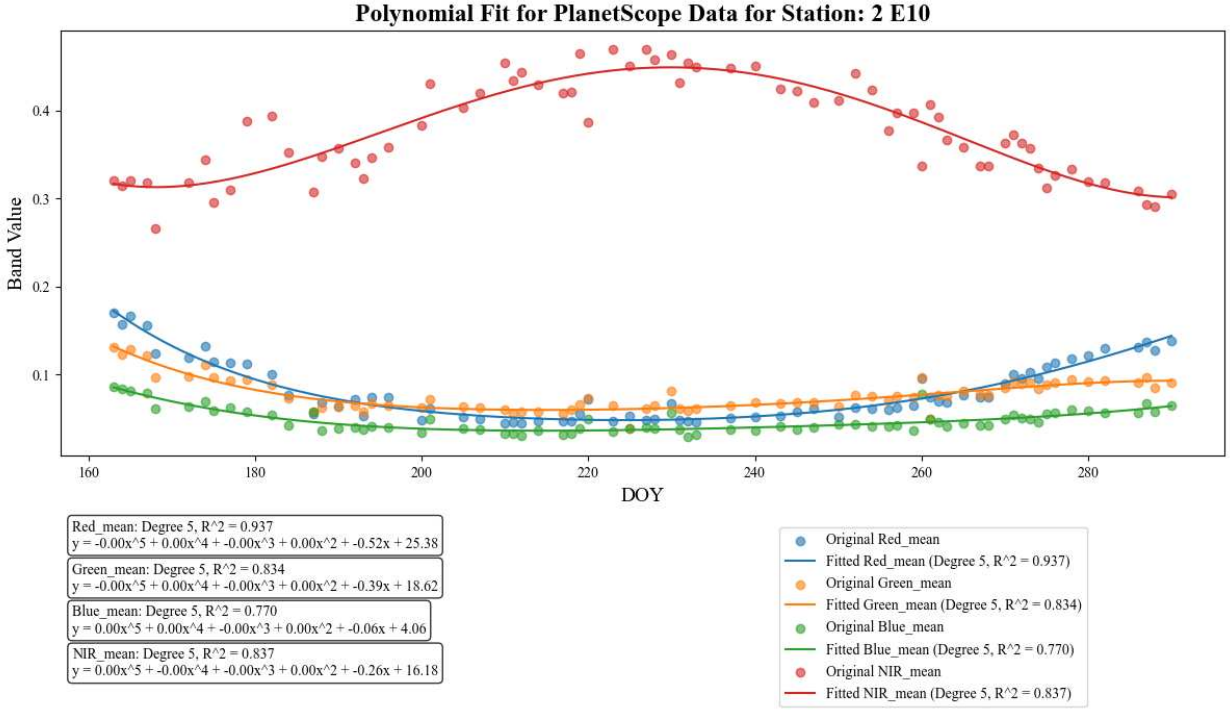
Polynomial Fit for PlanetScope Data for Station: 2 E10
Band Value
DOY
0.1
0.2
0.3
0.4
160
180
200
220
240
260
280
Red_mean: Degree 5, R^2 = 0.937
y = -0.00x^5 + 0.00x^4 + -0.00x^3 + 0.00x^2 + -0.52x + 25.38
Green_mean: Degree 5, R^2 = 0.834
y = -0.00x^5 + 0.00x^4 + -0.00x^3 + 0.00x^2 + -0.39x + 18.62
Blue_mean: Degree 5, R^2 = 0.770
y = 0.00x^5 + 0.00x^4 + -0.00x^3 + 0.00x^2 + -0.06x + 4.06
NIR_mean: Degree 5, R^2 = 0.837
y = 0.00x^5 + -0.00x^4 + -0.00x^3 + 0.00x^2 + -0.26x + 16.18
Original Red_mean
Fitted Red_mean (Degree 5, R^2 = 0.937)
Original Green_mean
Fitted Green_mean (Degree 5, R^2 = 0.834)
Original Blue_mean
Fitted Blue_mean (Degree 5, R^2 = 0.770)
Original NIR_mean
Fitted NIR_mean (Degree 5, R^2 = 0.837)

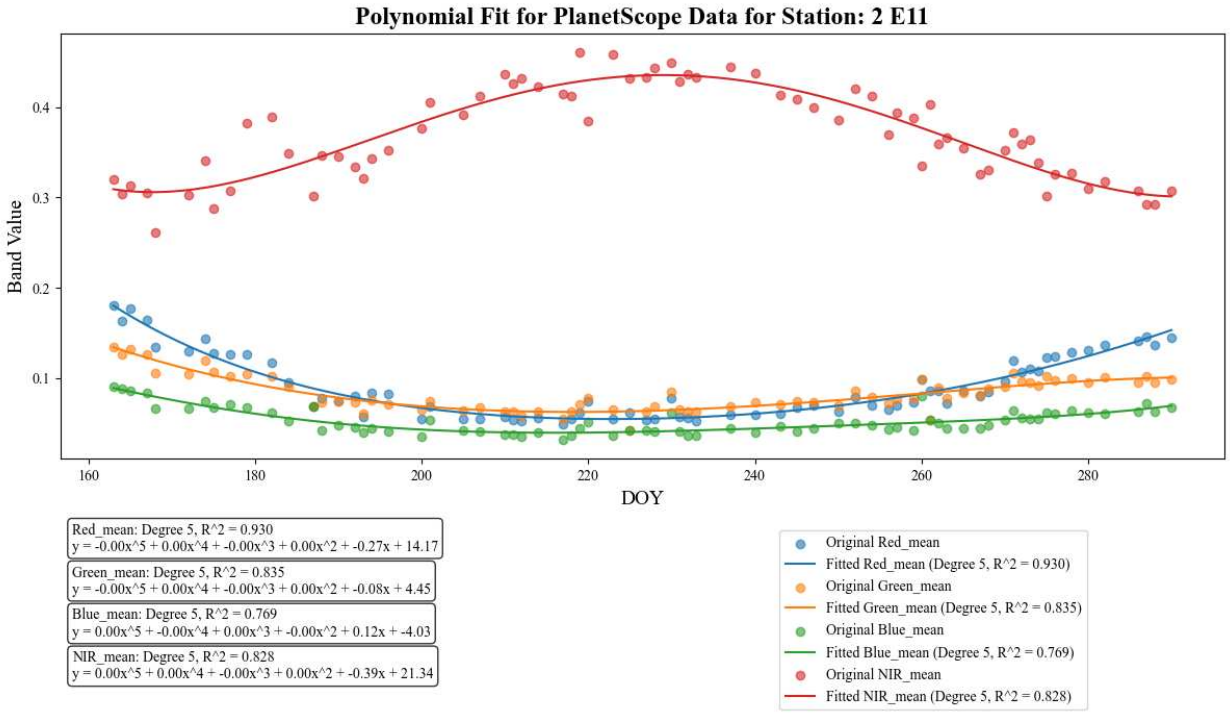

Red_mean: Degree 5, R^2 = 0.930
y = -0.00x^5 + 0.00x^4 + -0.00x^3 + 0.00x^2 + -0.27x + 14.17

Green_mean: Degree 5, R^2 = 0.835
y = -0.00x^5 + 0.00x^4 + -0.00x^3 + 0.00x^2 + -0.08x + 4.45

Blue_mean: Degree 5, R^2 = 0.769
y = 0.00x^5 + -0.00x^4 + 0.00x^3 + -0.00x^2 + 0.12x + -4.03

NIR_mean: Degree 5, R^2 = 0.828
y = 0.00x^5 + 0.00x^4 + -0.00x^3 + 0.00x^2 + -0.39x + 21.34

Original Red_mean
Fitted Red_mean (Degree 5, R^2 = 0.930)
Original Green_mean
Fitted Green_mean (Degree 5, R^2 = 0.835)
Original Blue_mean
Fitted Blue_mean (Degree 5, R^2 = 0.769)
Original NIR_mean
Fitted NIR_mean (Degree 5, R^2 = 0.828)